DSc dissertation

Non-equilibrium dynamics of low dimensional quantum systems

Balázs Dóra

Budapest University of Technology and Economics
Department of Physics

2014

Contents

Chapter 1

Introduction

1.1 Monolayer graphene

The first isolation of monolayer graphene (MLG), a single sheet of carbon atoms forming a honeycomb lattice, in 2004[1, 2] has attracted a huge interest, and practically revolutionized physics and has affected the research of many physicists. This is partly due to the fact that graphene is the first stable two dimensional crystal, awaiting our exploration, and partly because a general agreement has been reached in the closer condensed matter and broader physics community that the basic model describing its charge carriers is an effective, two dimensional, massless Dirac equation. Therefore, in contrast to e.g. high T_c superconductors, where one has to struggle to justify the actual model choice, not mentioning the various approximation schemes, graphene's low energy dynamics was soon demonstrated to be accountable for by the Dirac equation, as evidenced by numerous experimental, theoretical and ab initio studies.

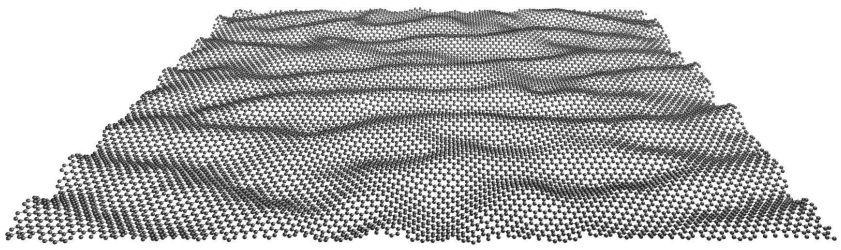

Figure 1.1: Ripples in graphene

Even its existence is surprising, since the Mermin-Wagner theorem does not allow for positional long-range order in two dimensions, thermal fluctuations are expected to destroy long range crystalline ordering. A possible way

out is provided by realizing that graphene is still of finite size, therefore as long as the coherence length of ordering is longer than the actual system size, it looks a stable two dimensional crystal. Moreover, improved experimental techniques have revealed that graphene is not strictly two-dimensional but hosts ripples i.e. surface waves, and stabilizes itself by fluctuations in the third spatial dimension, as shown in Fig. 1.1, which are typically 20-200 $\mathring{A}$ long and 10 $\mathring{A}$ high bumps

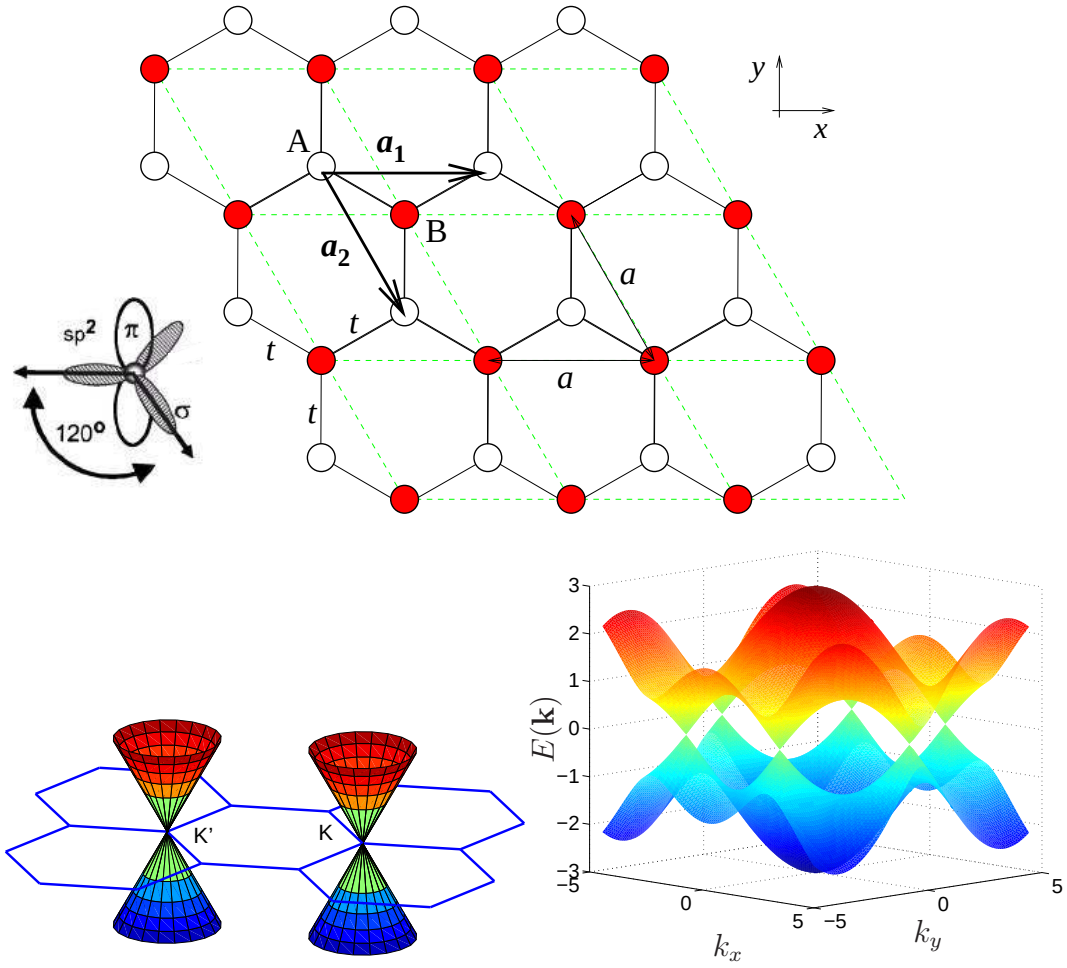

Figure 1.2: Top: a small segment of the honeycomb lattice in shown, made of two interpenetrating triangular lattices, with the two triangular sublattices denoted by filled and empty circles, together with the translational lattice vectors a_1 and a_2. The green lines separate the unit cells. Bottom left: the low energy part of the spectrum in momentum space with the two non-equivalent Dirac cones at the opposite corners of the Brillouin zone. Bottom right: The full energy spectrum in the Brillouin zone.

Soon after its discovery, a variety of interesting effect were predicted and subsequently observed experimentally, such as unconventional quantum Hall effect[2], a (possibly universal) minimal conductivity at vanishing carrier concentration[3], Klein tunneling in p-n junctions[4, 5] and Zitterbewegung[6, 7], frequency independent optical conductivity over a wide frequency range etc.

All these are natural consequences of the low energy physics of the half-filled honeycomb lattice, studied in the tight-binding approximation. The honeycomb lattice, depicted in Fig. 1.2 is regarded as two interpenetrating triangular lattices, whose lattice sites form the two sublattices. By considering only nearest neighbour, intersublattice hoppings, the resulting Hamiltonian is written in momentum space in second quantized form as

$$H_{graphene} = \sum_{\mathbf{k},\sigma} \; (a^+_{\mathbf{k},\sigma}, b^+_{\mathbf{k},\sigma}) \; \begin{pmatrix} 0 & tf(\mathbf{k}) \\ tf^*(\mathbf{k}) & 0 \end{pmatrix} \begin{pmatrix} a_{\mathbf{k},\sigma} \\ b_{\mathbf{k},\sigma} \end{pmatrix}, \tag{1.1}$$

where the $a_{\mathbf{k},\sigma}$ and $b_{\mathbf{k},\sigma}$ operators annihilate particles from sublattice A and B with momentum $\mathbf{k}$ and spin σ, $f(\mathbf{k}) = 1 + 2\exp(i3k_y/2)\cos(\sqrt{3}k_x/2)$, and we use the convention to take the nearest neighbour carbon atom distance to unity (which is 1.42 $\mathring{A}$), and $t \approx 2.7$ eV the hopping integral between neighbouring carbon atoms. Therefore, the spectrum consists of two bands as $E_\pm(\mathbf{k}) = \pm t|f(\mathbf{k})|$. The two bands touch each other at the corners of the hexagonal Brillouin zone, among which three-three are connected by reciprocal lattice vectors, ending up with two non-equivalent touching points at K and K'. By expanding the spectrum around these point, using e.g. $f(\mathbf{K}+\mathbf{p}) \approx (3/2)(p_x + ip_y)$, we arrive to a linearly dispersing band-touching as $E^K_\pm(\mathbf{p}) = \pm 3t|\mathbf{p}|/2$ at around point K, and similarly for point K'. The low energy physics is determined by excitations living close to these Dirac points, described by an effective Dirac equation, given by

$$H_{graphene} = \sum_{\mathbf{p},\sigma,\tau_z} \Psi^+_{\mathbf{p},\sigma,\tau_z} \begin{pmatrix} 0 & v_F(p_x - \tau_z i p_y) \\ v_F(p_x + \tau_z i p_y) & 0 \end{pmatrix} \Psi_{\mathbf{p},\sigma,\tau_\mathbf{z}}, \tag{1.2}$$

where $v_F = 3t/2 \sim 10^6$ m/s is the Fermi velocity, $\tau_z = 1$, -1 denotes the K and K' points and represents the valley degree of freedom and the spinor $\Psi_{\mathbf{p},\sigma,\tau_\mathbf{z}} = (a_{\mathbf{p},\sigma,\tau_\mathbf{z}}, b_{\mathbf{p},\sigma,\tau_\mathbf{z}})$ contains operators with momentum close to the Dirac point at K ($\tau_z = 1$) or K' ($\tau_z = -1$). By focusing on the e.g. $\tau_z = 1$ term, namely a single a single Dirac cone, which is written in first quantized form as

$$H_{Dirac} = v_F \begin{pmatrix} 0 & \hat{p}_x - i\hat{p}_y \\ \hat{p}_x + i\hat{p}_y & 0 \end{pmatrix} = v_F \boldsymbol{\sigma} \cdot \hat{\mathbf{p}}, \tag{1.3}$$

where $\boldsymbol{\sigma} = (\sigma_x, \sigma_y)$ are Pauli matrices, most of graphene's properties can be analyzed by borrowing from high energy physics or QED to some extent, where the appearance of the Dirac equation is part of the daily routine. However, there are several significant differences between graphene's Dirac equation and its relativistic version: *first*, graphene's charge carriers are massless in the relativistic sense, namely that $E(\mathbf{p}) \sim |\mathbf{p}|$ down to small momenta, whose fully relativistic realization among elementary particles is hotly debated. Note that in the condensed matter sense, these are infinitely heavy particles since the inverse of the effective mass tensor, calculated as

$$m^{-1} = \frac{v_F}{|\mathbf{p}|^3} \begin{pmatrix} p_y^2 & -p_x p_y \\ -p_x p_y & p_x^2 \end{pmatrix}, \tag{1.4}$$

has zero determinant and is therefore non-invertible. *Second*, the maximal velocity for graphene's particles is the Fermi velocity, being 1/300th the velocity of light, therefore bringing the typical energy scales, required to investigate graphene, down to the conventional energy scales of a condensed matter experiment, thus allowing for the observation of relativistic phenomena in low temperature labs. *Third*, the matrix structure in Eq. (1.2) stems from a peudospin variable, accounting for the two non-equivalent sublattices of the honeycomb lattice and not from the the physical spin of the particles. Due to this sublattice structure, these are called chiral Dirac electrons, since the helicity operator, $\boldsymbol{\sigma} \cdot \mathbf{p}/|\mathbf{p}|$ commutes with the Hamiltonian and is a good quantum number. For graphene, this implies $\boldsymbol{\sigma} \parallel \mathbf{p}$ for a given eigenstate. Note that by taking additional complications in the band structure into account (e.g. hoppings etc), the Dirac points are shifted in energy, but otherwise remain intact.

Due to the linear energy-momentum relationship and the two-dimensionality of graphene, its density of states (DOS) per unit volume vanishes linearly close to half filling as

$$\rho(\omega) = \frac{1}{2\pi} \frac{|\omega|}{v_F^2} \tag{1.5}$$

per spin and valley, similarly to d-wave superconductors or d-density waves[8]. In this respect, graphene is neither a metal with a sizeable DOS at the Fermi energy, nor an insulator with strongly suppressed DOS, but can be regarded as a semimetal.

The linear band crossing, provided by the Dirac equation in Eq. (1.3), possesses a half-integer quantized Berry flux[9]. The wavefunction is written in momentum space as

$$|\alpha, \mathbf{p}\rangle = \frac{1}{\sqrt{2}} \begin{pmatrix} \alpha \\ \exp(i\varphi_p) \end{pmatrix}, \tag{1.6}$$

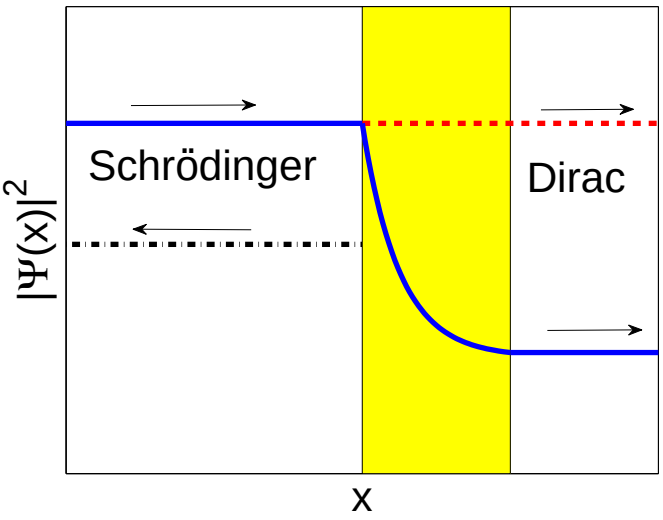

Figure 1.3: Schematics of Klein tunneling in graphene. At normal incidence, the transmission probability is always one for chiral particles, regardless to the width or height of the barrier.

where $\alpha = \pm$ corresponds to positive and negative energy states as $E_\alpha(\mathbf{p}) = \alpha v_F|\mathbf{p}|$ and $\varphi_p = \arctan(p_y/p_x)$. The Berry phase is calculated from

$$-i \oint_C d\mathbf{p} \cdot \langle \mathbf{p}, \alpha | \boldsymbol{\nabla}_\mathbf{p} | \alpha, \mathbf{p} \rangle = \pm\pi, \tag{1.7}$$

where C is a contour in momentum space enclosing the Dirac point and the $\pm$ sign depends on the orientation of the contour. The π Berry phase is regarded as a hallmark of two-dimensional massless Dirac fermions.

Another particularly interesting feature of Dirac fermions, stemming from their chiral nature, is their insensitivity to external electrostatic potentials due to the so-called Klein tunneling[5], meaning that Dirac fermions can be transmitted with probability 1 through a classically forbidden region, as illustrated schematically in Fig. 1.3. This happens because positive energy states can tunnel into negative energy states without changing their quantum numbers. In particular, for a potential barrier of width D and height V_0, the transmission probability of an incoming electron with energy $|E| << |V_0|$ is[3, 10]

$$\mathcal{T}(\phi) = \frac{\cos^2(\phi)}{1 - \cos^2(Dq_x)\sin^2(\phi)}, \tag{1.8}$$

where ϕ is the angle of incidence and $q_x \approx \sqrt{(V_0/v_F)^2 - k_y^2}$ is the longitudinal

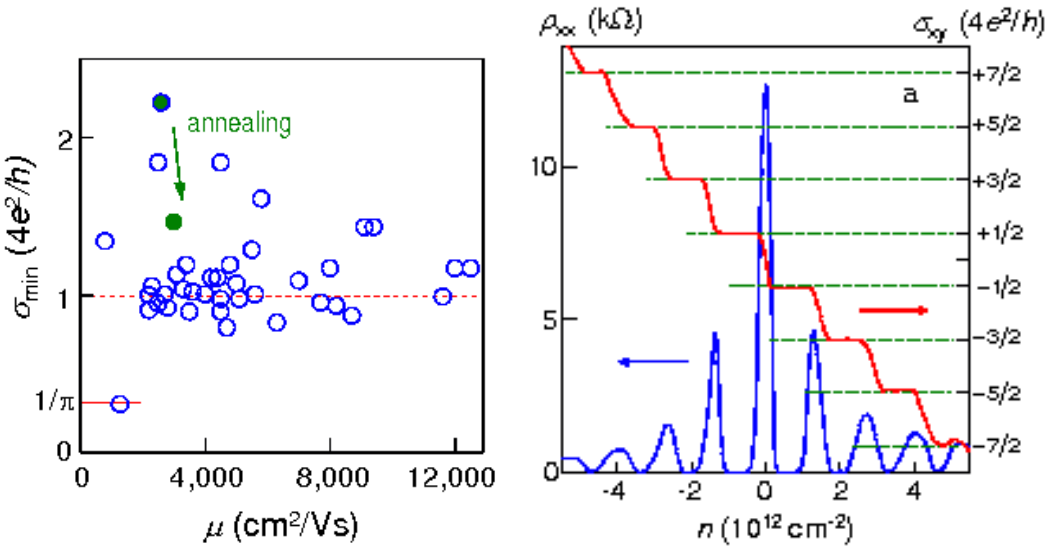

Figure 1.4: Left: the minimal conductivity of various quality graphene samples at the Dirac (charge neutrality) point. Right: the longitudinal resistivity and Hall conductivity of graphene in quantizing magnetic field as a function the carrier density.

component of the momentum within the barrier and k_y is the conserved component of the momentum, parallel to the barrier. Note that for $Dq_x = n\pi$ with n an integer, the barrier becomes completely transparent since $\mathcal{T}(\phi) = 1$, independent of the value of ϕ. In addition, for normal incidence with $\phi \to 0$ and for any value of Dq_x, barrier is again totally transparent. This result is a manifestation of the Klein tunneling[5], which does not occur for nonrelativistic electrons, where for normal incidence, the transmission is always smaller than 1. Due to Klein tunneling, Dirac electrons cannot be confined by conventional potential barriers[11], provided by gating the sample, as opposed to conventional semiconductor technology.

Since helicity is a good quantum number in the low energy Dirac equation description of graphene, backscattering is forbidden since it would require changing the sign of the helicity of a given momentum state, which cannot be provided by simple potential scatterers. Due to this, Dirac electron transport in graphene can be ballistic for typical sample sizes. Since disorder is unavoidably present in any material, there has been a great deal of interest in trying to understand how disorder affects the physics of Dirac electrons in graphene and its transport properties. Under certain conditions, Dirac fermions are immune to localization effects observed in ordinary electron

systems and it has been established experimentally that electrons can propagate without scattering over large spatial regions of the micron size. This originates from the intricate interplay of scattering and density of states: as the charge neutrality point is approached, a decreasing number of particles are available for charge transport due to the vanishing DOS, which, on the other hand acquire an increasingly long lifetime even in the presence of disorder. These two effects cancel each other perfectly, resulting in a finite, almost universal minimal conductivity at the Dirac point, largely independent from the microscopic details of the sample, as illustrated in Fig 1.4.

Since graphene is inherently two-dimensional, it represents an ideal platform to study quantum-Hall physics. A semiclassical Bohr-Sommerfeld quantization of the cyclotron orbits predicts that the Landau levels follow an unusual sequence as $E_n \sim \sqrt{n+\Gamma}$, where n is the Landau level index and Γ is related to the Berry phase and can only be determined from quantum mechanical considerations. These yield

$$E_n = \mathrm{sign}(n) v_F \sqrt{2|n|eB_\perp}, \tag{1.9}$$

where $B_\perp$ is the perpendicular component of the magnetic field to the graphene plane, and n is an integer. As opposed to a normal two-dimensional electron gas (2DEG), these levels are not equidistant, and depend on $\sqrt{B_\perp}$ in contrast to the linear dependence of the 2DEG and do not possess zero point energy, as follows from a Dirac oscillator vs. Schrödinger oscillator scenario. Each Landau level is fourfold degenerate, coming from the combined effect of the valley (2) and spin (2) degrees of freedom. The zero mode, provided by the $n = 0$ Landau level is special since it is half electron- and half hole-like, as it sits right at the intersection of the upper and lower Dirac cones, i.e. at the Dirac point (see Fig. 1.5) When calculating the Hall conductivity, each Landau levels contributes with a step of $4 \times e^2/2h$ to the Hall conductivity, where the factor of 4 comes from the valley and spin degeneracies, and the 2 in the denominator results from the π quantized Berry phase. The Hall conductivity is qualitatively well described by

$$\sigma_{xy} = \frac{2e^2}{h} \mathrm{sign}(B) \sum_{n=-N}^{N} \mathrm{sign}\left(E_n - \mu\right) \tag{1.10}$$

producing the unconventional Hall steps in graphene as a function of the chemical potential μ, as shown in Fig. 1.4, and N is a symmetric cutoff.

The first quantum Hall step, starting from the Dirac point with $\mu = 0$, is only $2e^2/h$ large as opposed to the subsequent steps in the series with $4e^2/h$ size. This roots back to the peculiar zeroth Landau level with $n = 0$, which

is only half particle like, therefore contributes only with a half step to the plateaux sequence. Note that if there was no spin and valley degeneracy, the contribution of this zeroth Landau level would be a half-integer quantized Hall conductivity as $e^2/2h$. Apparently, Dirac points always appear in pairs due to a no-go theorem[12], therefore the smallest step is expected to be e^2/h in general.

The lowest (small n) Landau levels in graphene are separated by an energy gap of order 300-400 K in a magnetic field of 1 T, in contrast to a two-dimensional electron gas, where the equidistant Landau levels are separated by a gap of the order of the magnetic field itself. Due to the peculiar quantization of Dirac fermions, the quantum-Hall effect remains observable even at room temperatures[13]. These are illustrated with the density of states of Landau quantized Dirac and normal two-dimensional electrons in Fig. 1.5.

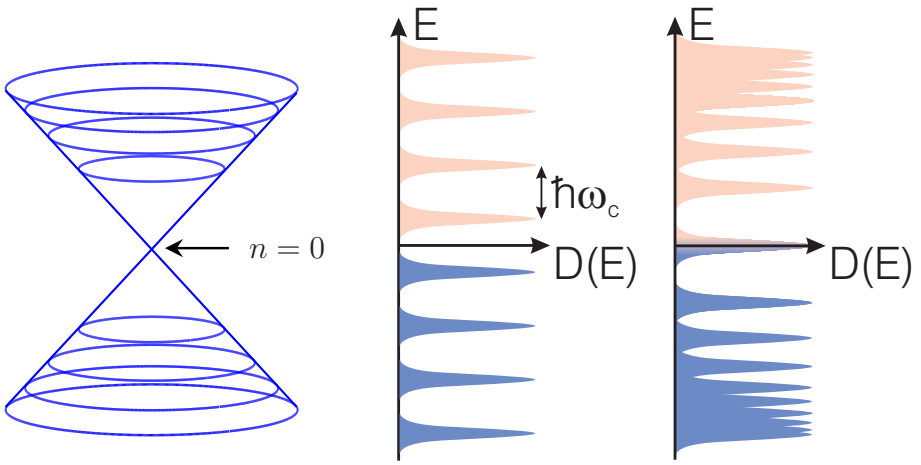

Figure 1.5: Left: the Landau level structure in the Dirac cone. Right: the DOS in a Landau quantized normal two-dimensional electron gas and graphene.

Graphene's two dimensionality notwithstanding, it was possible to measure its optical conductivity, which exhibits a frequency independent optical response over a wide frequency range. This can be understood from simple considerations: the electric current operator in the x direction for Dirac fermions is $j_x = ev_F\sigma_x$, independent from the momentum. Its matrix element, corresponding to interband transition is $|\langle \mathbf{p}, +|j_x|\mathbf{p}, -\rangle|^2 = \sin^2(\varphi_p)$. The total number of states, participating in this process is proportional to the size of the Fermi surface $\sim |\mathbf{p}|$. Putting this together and using the linear relationship between energy and momentum, the total number of states,

probed by an electromagnetic wave with frequency ω, scales with $|\omega|$. Dividing it by the frequency gives the optical conductivity, which indeed becomes frequency independent. By working out the prefactor, the optical conductivity is

$$\sigma_{xx}(\omega) = \frac{\pi e^2}{2h}. \tag{1.11}$$

Not surprisingly, since the Dirac equation does not contain any intrinsic energy scale which would influence the optical response, the optical conductivity is also universal. The optical transparency is calculated from this as $\mathcal{T}_{opt} = 1 - \pi\alpha$, where $\alpha = e^2/\hbar c \approx 1/137$ is the fine-structure constant. Despite being only one atom thick, graphene is found to absorb a significant 2.3% fraction of incident white light, By stacking graphene to obtain multilayer graphene, the optical transparency reduces linearly with the number of layers for up to 5 layers, as shown in Fig. 1.6.

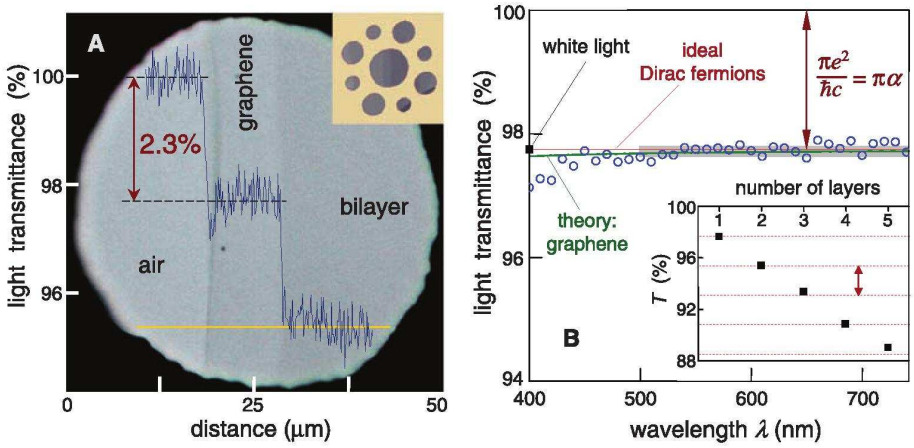

Figure 1.6: Left: Photograph of an aperture partially covered by mono and bilayer graphene. The line scan profile shows the intensity of transmitted white light. Right: Optical transmittance as a function of the number of graphene layers. From Ref. [14]

Most of graphene's electronic properties can be analyzed using a single particle picture based in the Dirac equation, and surprisingly good agreement is reached when comparing to experimental results. This is even more surprising in light of the fact that since its effective "light" velocity (i.e. the Fermi velocity) is 300 times smaller than the speed of light, its fine structure constant should be 300 times bigger than that in QED, of the order of 1-2, suggesting that interaction effects would play an important role and should

be non-perturbative. While in most condensed matter systems, interaction effect are omnipresent and obvious, one has to struggle with graphene to see any sign of interactions. From the point of view of basic research, the resent discovery of fractional quantum Hall physics in graphene sounds really promising[15, 16], allowing for studying strongly interacting Dirac fermions in quantizing magnetic field with no obvious analogue on high energy physics.

In addition to its unique electronic properties, which is the main concern of this dissertation, graphene also exhibits unique mechanical properties and is said to be the strongest material ever measured with a Young's modulus in the TPa regime. Its two-dimensionality makes it an ideal candidate to engineer planar electronic devices. Since its bulk is its surface, it was shown to be capable of detecting individual gas molecules, attached to its surface. Among many others, graphene could accelerate genomics by reading the whole human genome in two and a half hours. Whether graphene fulfills the promise it holds in applied sciences remains to be seen in the future, but it has certainly revolutionized condensed matter and related fields enormously over the past 7-8 years.

1.2 Bilayer graphene

Bilayer graphene (BLG) is composed of two monolayer graphenes (MLGs) in Bernal or AB stacking, meaning that the A sublattice of one layer is on top of the B sublattice of the other layer, as shown in Fig. 1.7. This is the typical stacking pattern of 3D graphite as well. Its charge carriers, as we show below, reveal non-relativistic, "Schrödinger" (quadratic dispersion) and relativistic "Dirac" (chiral symmetry, unusual Berry phase) features. Due to their peculiar nature, as discussed below, BLG holds the promise of revolutionizing electronics, since its band gap is directly controllable by a perpendicular electric field over a wide range of parameters [17, 18, 19, 20, 21] (up to 250 meV [22]), unlike existing semiconductor technology. Moreover, unlike monolayer graphene, whose effective model, namely the Dirac equation was thoroughly investigated in QED and relativistic quantum mechanics, understanding the low energy properties of BLG represents a new challenge.

The band structure of BLG also follows from tight-binding calculations. In addition to the intralayer hopping of the graphene layers, an interlayer hopping, $t_\perp \approx 0.3$-0.4 eV should be taken into account, since the typical distance between the layers is $d = 3.3$ $\mathring{A}$. Additional hopping processes are also present, but these are neglected for the sake of simplicity. A tight

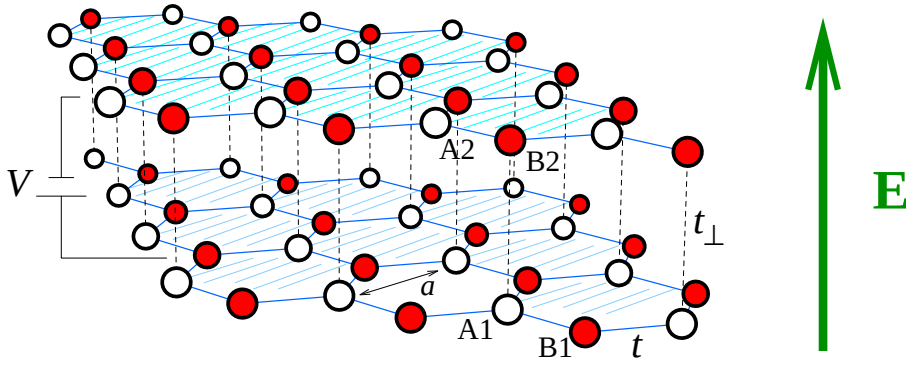

Figure 1.7: The lattice structure of BLG with the relevant hopping processes, the vertical green arrow denotes a perpendicular electric field.

binding calculation for the kinetic energy gives

$$H_{graphene} = \sum_{\mathbf{k},\sigma} \Psi^+(\mathbf{k},\sigma) \begin{pmatrix} \Delta & tf(\mathbf{k}) & 0 & 0 \\ tf^*(\mathbf{k}) & \Delta & t_\perp & 0 \\ 0 & t_\perp & -\Delta & tf(\mathbf{k}) \\ 0 & 0 & tf^*(\mathbf{k}) & -\Delta \end{pmatrix} \Psi(\mathbf{k},\sigma), \tag{1.12}$$

where the $\Psi^+(\mathbf{k},\sigma) = (a^+_{1,\mathbf{k},\sigma}, b^+_{1,\mathbf{k},\sigma}, a^+_{2,\mathbf{k},\sigma}, b^+_{2,\mathbf{k},\sigma})$, and the operators create particles on layer 1 or 2, sublattice A or B with momentum $\mathbf{k}$ and spin σ, as visualized in Fig. 1.7, and $f(\mathbf{k})$ has already been defined for MLG. Here, Δ represents a layer dependent chemical potential, which arises upon switching on a perpendicular electric field. Due to the 4 atoms in the unit cell, BLG possesses 4 band, two of them touching each other at zero energy for $\Delta = 0$, and two others separated by $\pm t_\perp$, as shown in Fig. 1.8

The low energy part of the spectrum in BLG is obtained by integrating out the high energy modes, leading to an effective 2×2 description as[18, 23]

$$H = \begin{pmatrix} \Delta & (p_x - ip_y)^2/2m \\ (p_x + ip_y)^2/2m & -\Delta \end{pmatrix}, \tag{1.13}$$

where $m = t_\perp/2v_F^2 \approx 0.03m_e$, and its spectrum is $\pm\sqrt{\Delta^2 + (|\mathbf{p}|^2/2m)^2}$. In the presence of a finite electric field, the band touching disappears and a finite bandgap appears, whose size is easily tunable by the electric field. However, screening due to electron interactions becomes relevant in this case, and the induced gap is related to the external potential, U_{ext}, created by the electric

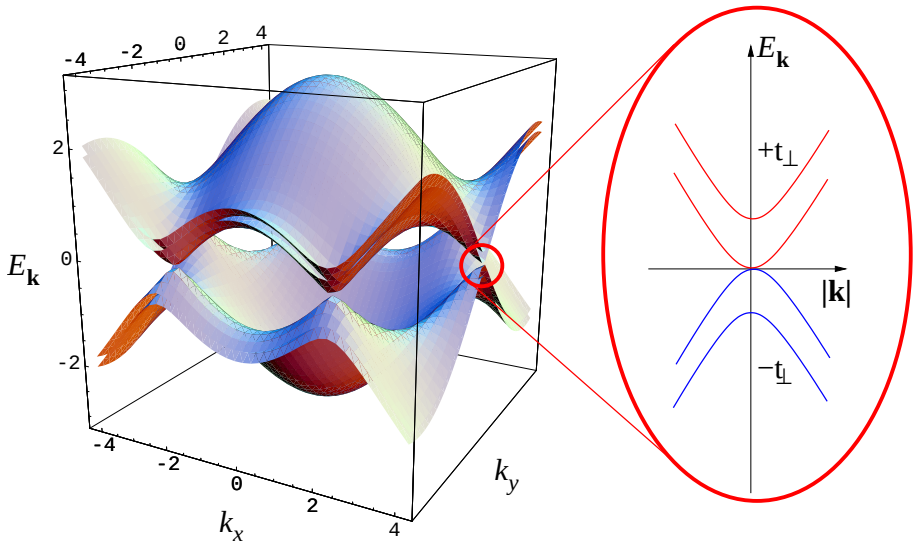

Figure 1.8: The energy spectrum of BLG in the Brillouin zone together with the low energy part of the spectrum around zero energy for $\Delta = 0$.

field as [18, 24]

$$2\Delta = U_{ext} + \frac{e^2 d\delta n}{2A_c\varepsilon_r\varepsilon_0}, \tag{1.14}$$

where $\delta n = \sum_p (n_{1p} - n_{2p})$ is the dimensionless density imbalance between the two layers with n_{ip} the particle density of state p on the ith layer. The induced gap to a good approximation is given by [18, 17]

$$\Delta = \left(1 + \lambda \ln\left(\frac{4t_\perp}{|U_{ext}|}\right)\right)^{-1} \frac{U_{ext}}{2}, \tag{1.15}$$

and the density imbalance reads

$$\delta n = 4\rho_0 \Delta \ln\left(|\Delta|/2t_\perp\right), \tag{1.16}$$

with $\lambda = e^2 d\rho_0/A_c\varepsilon_r\varepsilon_0 \sim 0.1 - 0.5$ the dimensionless screening strength, ε_0 the permittivity of free space and $\rho_0 = A_c m/2\pi\hbar^2$ the density of states per valley and spin in the limit $\Delta \to 0$. For SiO_2/air interface, $\varepsilon_r \approx 2.5$ ($\varepsilon_r = 25$ for NH_3, $\varepsilon_r = 80$ for H_2O), which reduces the effects of screening. This extra tunability of its bandgap makes bilayer graphene a promising candidate as well for future electronic devices. By applying a dual-gate structure [19, 22, 20, 25, 21] with top and back-gate, the size of the gap together with the total number of charge carriers can be tuned independently.

The physical properties of BLG with $\Delta = 0$ are as surprising as those of MLG, and vaguely speaking, in spite of the different topology of the low energy Hamiltonians in Eqs. (1.3) and (1.13), it is a "factor of 2 times monolayer graphene". It exhibits a universal minimal conductivity at the charge neutrality point, which is twice as large as that of MLG. Its wavefunction in momentum space is

$$|\alpha, \mathbf{p}\rangle = \frac{1}{\sqrt{2}} \begin{pmatrix} \alpha \\ \exp(i2\varphi_p) \end{pmatrix}, \tag{1.17}$$

where $\alpha = \pm$ corresponds to positive and negative energy states as $E_\alpha(\mathbf{p}) = \alpha|\mathbf{p}|^2/2m$ and $\varphi_p = \arctan(p_y/p_x)$. The Berry phase is calculated to be $\pm 2\pi$ [26] and in spite of its massive quasiparticles, it exhibits chiral symmetry unlike particles obeying the standard Schrödinger equation. The Klein tunneling is also peculiar in BLG: no perfect transmission occurs for perpendicular incidence, in contrast to MLG, but perfect reflection. This perfect reflection (instead of the perfect transmission) is viewed as another manifestation of Klein tunneling, because the effect is again due to the chirality of the quasiparticles (fermions in MLG and BLG exhibit chiralities that resemble those associated with spin 1/2 and 1, respectively, as follows from the π and 2π Berry phases). For MLG, an electron wavefunction at the barrier interface matches perfectly the corresponding wavefunction for a hole with the same direction of pseudospin due to chiral symmetry, yielding $\mathcal{T} = 1$. In contrast, for BLG, the chiral symmetry requires a propagating electron with wavevector $\mathbf{k}$ to transform into a hole with wavevector $i\mathbf{k}$ (rather than $-\mathbf{k}$), which is an evanescent wave inside a barrier.

Additionally, BLG is also characterized by a featureless optical conductivity which is twice that of MLG, as shown in Fig. 1.6. One essential difference, however, with respect to MLG is the finite density of states around half filling. Due to this, a short range electron-electron interaction is usually found to be marginally relevant, leading to all sorts of phase transition in BLG, at least on a theoretical level [27, 28, 29, 30]. The experimental verification of such phase transitions still remains to be seen.

The Landau level structure in a perpendicular magnetic field also shows Dirac like (chiral) and Schrödinger like features. In the absence of a gap, the Landau levels per spin and valley read as

$$E_{n\alpha} = \alpha\sqrt{n(n+1)}eB_\perp/m \tag{1.18}$$

with $\alpha = \pm$ and n non-negative integer and $B_\perp$ is the perpendicular component of the magnetic field to the BLG sheet. First of all, it contains two degenerate zero modes (in contrast to the single zero mode in graphene),

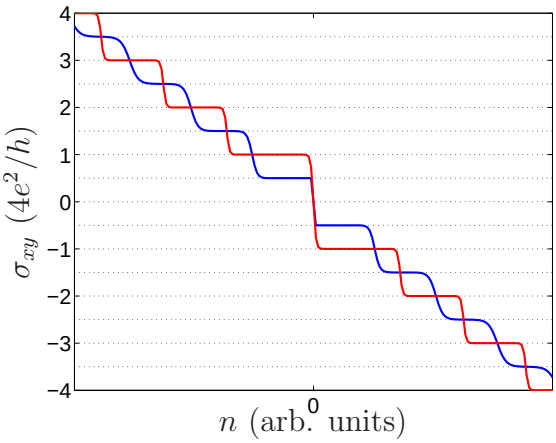

Figure 1.9: The Hall conductivity is shown schematically for MLG (blue) and BLG (red) as a function of the particle density, n, measured from half filling

while the low energy part of the spectrum increases is highly non-equidistant in the Landau level index. This, however, crosses over to a $\sim n$ increase with the Landau level index for large n, thus producing Schrödinger-like behaviour at high energies. The resulting quantum Hall effect is also different from that in graphene. Due to the doubled amount of zero modes, the first quantum Hall step is $4e^2/h$ large (twice as big as that in MLG) from the charge neutrality point, while all other steps have the same size as for graphene, since the degeneracies of the finite energy states are identical for MLG and BLG. The Hall conductivities are depicted in Fig. 1.9.

1.3 Topological insulators

Before the discovery of the integer quantum Hall effect, various phases of materials were classified according to their broken symmetries. For example, a crystal breaks the rotational and translational symmetry of free space, superconductors break the gauge invariance, a magnet breaks the spin rotational and sometimes the translational invariance etc. In 1980, the observation of the perfect quantization (up to 9 digits) of the integer quantum Hall effect[31] made us reconsider this issue, and the question "What causes quantization" called for an answer. Based on the seminal work in Ref. [32], it was realized that quantization results from topological order, and some response functions are determined by a topological invariant, explaining quantization. The response function is independent of the sample-dependent microscopic

parameters, such as scattering rate, interactions strength etc. due to topological protection. Such materials are termed topological insulators. Another, closely related definition states that a topological phase is an insulator in its bulk, which develops metallic surface or edge states when it gets in contact with a normal (i.e. topologically trivial) phase or vacuum. The connection between the two definitions is provided by the bulk-edge correspondence, which states that the integer value of the topological invariant is given by the number of surface or edge states. For example, a $2e^2/h$ Hall conductivity implies two conducting, ballistic, chiral channels around the edges of the sample, immune to backscattering.

The early members of the topological insulator (TI) family were the celebrated quantum Hall states, but due to recent experimental and theoretical progress [33, 34], numerous relatives have recently emerged. The topological protection of these materials mostly arises from their specific band structure, deriving from a strong spin-orbit interaction. Application-wise, TIs hold the promise to revolutionize spintronics, and contribute to conventional and quantum computing.

We start by introducing two-dimensional TIs with one-dimensional edge states. The first member of the TI insulator family is graphene. When supplemented with the intrinsic spin-orbit coupling (SOC), its Hamiltonian reads as[35]

$$H = v_F(\sigma_x p_x + \sigma_y \tau_z p_y) + \Delta \sigma_z \tau_z S_z, \tag{1.19}$$

where $\tau_z = \pm 1$ distinguishes between the K and K' valleys, S_z is the physical spin and Δ is the intrinsic SOC. This preserves parity and time reversal symmetry, and leads to a fully gapped spectrum in each valley as $\pm\sqrt{v_F^2|\mathbf{p}|^2 + \Delta^2}$, suggesting that it turns graphene into an insulator. However, when we leave the continuum limit and consider the original tight-binding problem on the hexagonal lattice, the above SOC can be originated by second nearest neighbour, intrasublattice hopping processes, which change sign according to whether the hopping occurs clockwise or anticlockwise on the hexagonal lattice. The SOC in Eq. (1.19) is related to a model introduced by Haldane [36] as a realization of the parity anomaly in (2+1) dimensional relativistic field theory. Since Eq. (1.19) conserves S_z, each spin species can be treated separately. The Hamiltonians for $S_z = \pm 1$ violate time reversal symmetry and are equivalent to Haldanes model for spinless electrons, which could be realized by introducing a periodic magnetic field with no net flux.

The energy spectrum of the lattice model, reducing to Eq. (1.19) in the continuum limit, is evaluated by considering a finite width graphene nanoribbon, revealing the presence of edge states. Fig. 1.10 shows the one dimensional energy bands for a strip where the edges are along the zig-zag direction

in the graphene plane. The bulk bandgaps at the one dimensional projections of the K and K' points are clearly seen. In addition to this, two bands traverse the gap, connecting the K and K' points. These bands are localized at the edges of the strip, and each band has degenerate copies for each edge. The edge states are not chiral since each edge has states which propagate in both directions. However, the edge states are "spin filtered" in the sense that electrons with opposite spin propagate in opposite directions.

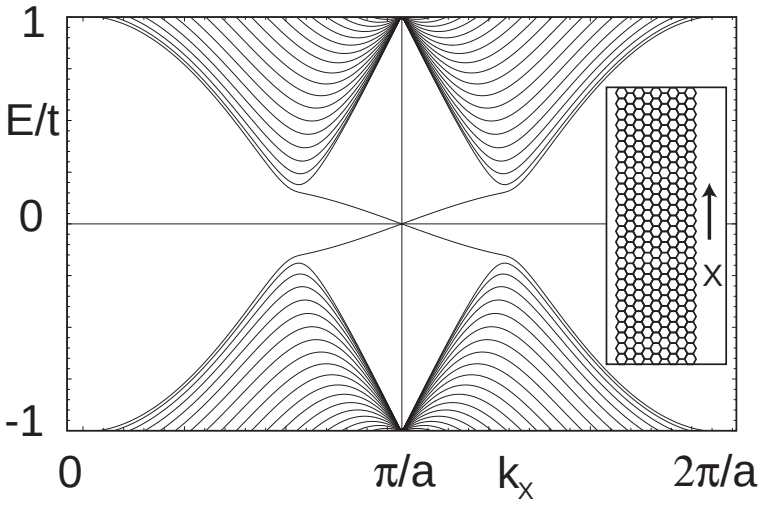

Figure 1.10: One dimensional energy bands for a strip of graphene (shown in inset). The bands crossing the gap are spin filtered edge states, from Ref. [35].

The effective model for the edge states is

$$H_{eff} = v_F S_z p_x, \tag{1.20}$$

protected by time reversal invariance, i.e. a right/left-going electron carries spin up/down, and backscattering can only occur if the spin is also flipped, therefore simple potential scattering cannot spoil the ballistic motion along the edges. The spin-Hall conductivity, calculated from either the bulk model[9] using Eq. (1.19) or using only the existence of ballistic edge states from Eq. (1.20), reads as

$$\sigma_{xy}^{spin} = \frac{e}{2\pi}, \tag{1.21}$$

being quantized. Note that this quantization is less robust than that of the quantum-Hall effect, since magnetic scatterers can provide us with efficient backscattering by flipping the electron spin, and degrade the quantized

spin-Hall response. So far, graphene as a spin-Hall insulator exists only in our dreams, since the size of the intrinsic SOC is estimated to be in the μeV range[37], being overwhelmed by additional processes such as impurity scattering etc. Nevertheless, cold atomic systems can be used to engineer graphene like system with intrinsic SOC [38].

Another member of the spin-Hall insulator family features a real material, where the existence of edge states was predicted theoretically[39] and subsequently demonstrated experimentally[40], namely HgTe/CdTe quantum wells. The $Hg_{1-x}Cd_xTe$ belongs to the family of semiconductors with strong spin-orbit interactions. Its band structure is rather common among semiconductors: the conduction/valence band states have an s/p-like symmetry. In HgTe, however, the p levels are above the s levels, resulting in an inverted band structure. Ref. [39] considered a quantum well structure where HgTe is sandwiched between layers of CdTe. When the thickness of the HgTe layer is $d < d_c = 6.3$ nm, the 2D electronic states bound to the quantum well have the normal band order. On the other hand, for $d > d_c$, the 2D bands invert. The inversion of the bands with increasing d signals a quantum phase transition between the trivial insulator and the quantum spin Hall insulator. This follows from the observation that the system has inversion symmetry: since the s and p states have opposite parity, the bands will cross each other at d_c without an avoided crossing, causing the energy gap to vanish at $d = d_c$.

The experimental results from Ref. [40] are depicted in Fig. 1.11, demonstrating convincingly the existence of the edge states of the quantum spin Hall insulator.

Three dimensional topological insulators posses two dimensional surface states, described by a two-dimensional Dirac equation as[33, 34]

$$H = v_F(S_x p_y - S_y p_x) + \Delta S_z, \tag{1.22}$$

where $\mathbf{S}$ stands for the physical spin, and Δ is a mass gap, originating from a thin ferromagnetic film covering the surface of TI, lifting the Kramer's degeneracy of the Dirac point. After a $\pi/2$ rotation of the spin around S_z, it reduces to the conventional form of the Dirac equation in Eq. (1.3). The spin dependence comes, similarly to the two-dimensional case, from strong spin-orbit coupling, therefore, materials with large atomic number are beneficial, such as Bi[33, 34].

Among their fascinating properties, such as the surface quantum Hall effect, coming from Eq. (1.22) in a perpendicular magnetic field, three-dimensional topological insulators feature the topological magnetoelectric effect. This means that the electron spin can be manipulated by an electric field and conversely, the electric current can be controlled by a magnetic

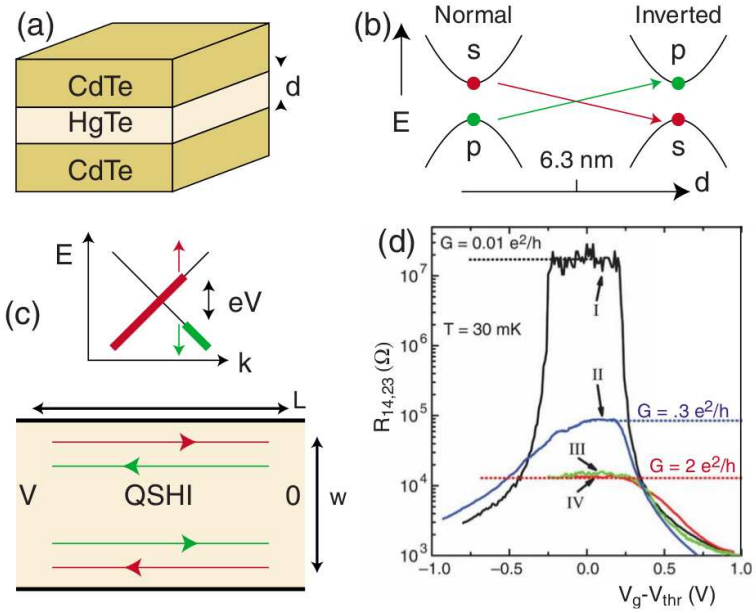

Figure 1.11: Experiments on HgTe/CdTe quantum wells. a) Quantum well structure. b) As a function of layer thickness d the 2D quantum well states cross at a band inversion transition. The inverted state is a quantum spin-Hall insulator with helical edge states, whose non-equilibrium population is determined by the leads (c). d) Experimental two terminal conductance as a function of a gate voltage that tunes the Fermi energy through the bulk gap. Sample III and IV show quantized transport associated with edge states. From Ref. [40].

field. This comes from the observation that the electric current operator for the surface states is $j_{x,y} \sim \partial H/\partial p_{x,y} \sim S_{y,x}$, therefore a vector potential, describing a time dependent electric field, which couples normally to the electric current, couples directly to the electron's spin. Conversely, the Zeeman coupling to a magnetic field, $\mathbf{B}$, involves $\mathbf{S} \cdot \mathbf{B}$ terms, affecting the charge dynamics.

1.4 Landau-Zener dynamics and Kibble-Zurek scaling

As we have seen previously, the basic equation governing the charge carriers in graphene and its variants as well as topological insulators is a 2×2

Dirac equation. Whenever some spatial or temporal dependent potentials are added to it, one needs to solve two coupled differential equations, as is the case for e.g. a time dependent vector potential, describing an electric field and spatially dependent scalar potential, accounting for a p-n junction in graphene[41]. The simplest and probably the most widely used time dependent 2×2 Hamiltonian is the Landau-Zener model[42, 43], which is to time-dependent quantum phenomena what the harmonic oscillator is to quantum mechanics. Note that the case of a scalar potential can also be mapped to this in the momentum representation[44]. It describes a two-level system, going through an avoided level crossing. Its Hamiltonian is

$$H_{LZ} = \begin{pmatrix} -vt & \Delta \\ \Delta & vt \end{pmatrix}, \tag{1.23}$$

and $v > 0$. Its instantaneous eigenenergies are given by $\epsilon_{\pm}(t) = \pm\sqrt{\Delta^2 + (vt)^2}$. Its eigenvectors are $|1\rangle = (1,0)^T$ with positive eigenenergy and $|0\rangle = (0,1)^T$ with negative eigenenergy, and the time evolution starts at $t \to -\infty$ with $|0\rangle$ being occupied. Was the time evolution completely adiabatic, i. e. $v \to 0$, then at time $t \to \infty$ the system would be in its ground state as $|1\rangle$ with probability one. In case of diabatic time evolution with $v \to \infty$, the final state at $t \to \infty$ would still coincide with the initial state as $|0\rangle$. For any finite rate passage, there will be a finite probability to stay in the initial state and to tunnel to the other state. The celebrated Landau-Zener formula describes the probability to tunnel into the excited state and is given by

$$P_{ad} = \exp\left(-\frac{\pi\Delta^2}{v}\right). \tag{1.24}$$

This can be obtained from the exact solution of the model, which is, however, not very illuminating since it involves the parabolic cylinder functions[45, 46]. By using some approximate, semiclassical methods such as the WKB[47] or its temporal version known as the Landau-Dykhne method[48, 49], the required probability is determined from

$$P_{ad} = \exp\left(-2\mathrm{Im}\int_{t_-}^{t_+} \epsilon_+(t)dt\right), \tag{1.25}$$

which describes the tunneling between the adiabatic energy levels, from $\epsilon_-(t)$ to $\epsilon_+(t)$, which is determined by the classically forbidden regions. The limits of integration is determined after continuing the adiabatic eigenenergies to complex time and look for a crossing point between the two bands as $\epsilon_+(t) =$

0. This occurs when $t_\pm = \pm i\Delta/v$. The above expression is correct within exponential accuracy in general since it neglects the interference between multiple quantum tunneling processes. Interestingly, this gives the exact result for the Landau-Zener model, e.g. for the present case. The above integral is evaluated easily since it only requires the knowledge of the area of a semi-circle, giving Eq. (1.24).

The Landau-Zener model is closely connected to the celebrated Kibble-Zurek scaling[50], and is often considered to be the microscopic basis to to derive it for specific models after mapping them to the Landau-Zener model[51], which is the case for a magnetic field quench in the transverse field Ising chain[52, 53] as an example. A quench here means a time-dependent change of some parameters in the Hamiltonian. If it is abrupt, we face a sudden quench. The Kibble-Zurek argument[54, 55] predicts a scaling form for the defect density following a slow quench through a quantum critical point. A finite rate passage through a quantum critical point (QCP) results in closing the gap, with an activated behaviour and a finite correlation length giving way to metallic response and power-law correlations exactly at the QCP. Due to the non-equilibrium nature of the process, defects (excited states, vortices) are produced. When the relaxation time of the system, which encodes how much time it needs to adjust to new thermodynamic conditions, becomes comparable to the remaining ramping time to the critical point, the system crosses over from the adiabatic to the diabatic (impulse) regime. In the latter regime, its state is effectively frozen, so that it cannot follow the time-dependence of the instantaneous ground states – as a result, excitations are produced[50]. Evolution restarts only after leaving the diabatic regime, with an initial state mimicking the frozen one. The theory, general as it is, finds application in very different contexts in physics, ranging from the early universe cosmological evolution[54] through liquid ^{3,4}He [56, 55, 57] and liquid crystals[58, 59] to ultracold gases[60], verified for both thermodynamic and quantum phase transitions[61].

Having argued that defects should be generated, we now sketch the derivation of the Kibble-Zurek scaling. Let Δ be the characteristic energy scale associated with the proximity to the critical point, which can be a gap or some other crossover scale. The evolution becomes non-adiabatic close to the critical point when the 'reaction time' of the quantum system given by the inverse of the energy gap is comparable with the timescale at which the Hamiltonian is changing: $1/\Delta \sim \Delta/(d\Delta/dt)$[62]. Assuming linear quenches of the form $\Delta \sim |t/\tau|^{z\nu}$, where τ measures the adiabaticity of the quench, the typical crossover time is $t_c \sim \tau^{z\nu/(z\nu+1)}$, where z and ν are the dynamical and correlation length exponents, respectively. The healing length, ξ typically denotes the length over which a single defect is present, which gives

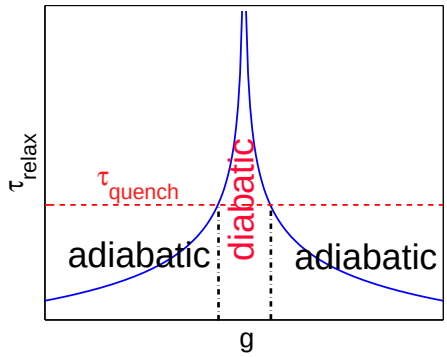

Figure 1.12: A cartoon for the Kibble-Zurek dynamics, g is a control parameter and the QCP is located at g_c, thus $\Delta \sim g - g_c$. When the relaxation time, $\tau_{relax} \sim 1/\Delta$ becomes comparable to the quench time, $\tau_{quench} \sim \Delta/(d\Delta/dt)$ (which is constant for a linear quench), the evolution becomes diabatic and defects are produced.

$\xi \sim \tau^{\nu/(z\nu+1)}$. The density of defects in a d-dimensional system scales as $1/\xi^d$ which leads to the Kibble-Zurek scaling form for the density of defects n given by

$$n \sim \xi^{-d} \sim \tau^{d\nu/(z\nu+1)}. \tag{1.26}$$

The process is shown schematically in Fig. 1.12.

1.5 Luttinger liquids: basic properties

Understanding non-equilibrium dynamics and quantum many body effects represent equally exciting problems of contemporary physics. When these two fields are combined, namely when strongly correlated systems are driven out-of-equilibrium, we face a real challenge. Experimental advances on ultracold atoms [63] have made the time dependent evolution and detection of quantum many-body systems possible, and in particular, quantum quenching the interactions by means of a Feshbach resonance or time dependent lattice parameters has triggered enormous theoretical [64, 65, 51, 66] and experimental [67, 68, 69, 70] activity.

Luttinger liquids (LLs) are ubiquitous as effective low-energy descriptions of gapless phases in various one-dimensional (1D) interacting systems [71, 72]. In 1D fermions, e.g., Landau's Fermi liquid (FL) description breaks down for any finite interaction, and the low-energy physics is described by bosonic collective modes with linear dispersion, and is characterized by anomalous

non-integer power-law dependences of correlation functions. This is to be contrasted to a Fermi liquid, where the quasi particle picture (electron) holds, implying critical exponents fixed to an integer. The LL similarly arises as the low-energy description of interacting 1D bosons or that of spin chains [71].

The breakdown of the FL description is best exemplified by the equal-time single particle correlation function, which, at $T = 0$, behaves in real space as

$$\langle \Psi(x,t)\Psi^{+}(0,t)\rangle_{FL} \sim \frac{Z}{x}, \tag{1.27}$$

for a FL, where $Z \leq 1$ is Landau's quasiparticle weight[73], and $\Psi(x,t)$ is the fermionic field operator, which annihilates a particles at x in real space and at t in real time. In a LL, it decays as

$$\langle \Psi(x,t)\Psi^{+}(0,t)\rangle_{LL} \sim \frac{1}{x^{1+\gamma^2}}, \tag{1.28}$$

where γ depends on the interaction strength. Its spatial Fourier transform corresponds to the momentum distribution function, which exhibits a finite jump at the Fermi wavevector k_F in a FL, signalling the existence of long-living fermionic excitations. In contrast, fermionic quasiparticles are not welcome in a LL, thus Z vanishes, as shown in Fig. 1.13.

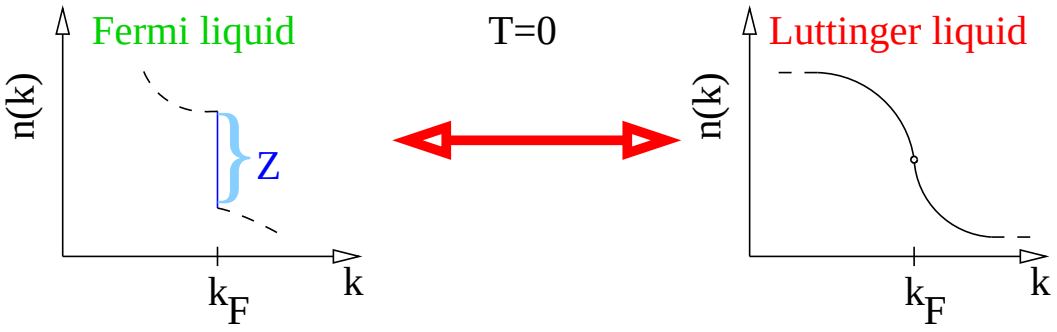

Figure 1.13: The momentum distribution function is depicted schematically for a FL (left) and LL (right). The finite jump at k_F, characteristic of the FL disappears in a LL, giving way to a smooth power law behavior.

A similar distinction can be made in the time or frequency domain as well. The decay of the real time correlator,

$$\langle \Psi(x,t)\Psi^{+}(x,0)\rangle_{FL} \sim t^{-1} \tag{1.29}$$

in a FL is to be contrasted to the LL behaviour as

$$\langle \Psi(x,t)\Psi^{+}(x,0)\rangle_{LL} \sim t^{-(1+\gamma^2)}, \tag{1.30}$$

changing the integer exponent to an arbitrary real number. Its temporal Fourier transform defines the density of states (DOS), whose behaviour is shown in Fig. 1.14. While the DOS is typically finite in a FL at the Fermi energy, it vanishes in a power law manner in a LL, developing pseudogap behaviour, because fermions are not good quasiparticles.

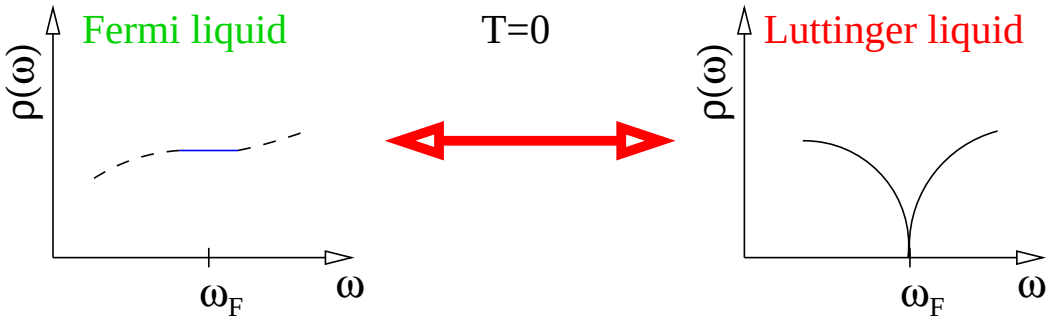

Figure 1.14: The quasiparticle density of states is shown schematically for a FL (left) and LL (right). The finite DOS at the Fermi energy, ω_F, characteristic to a FL, vanishes in a LL.

The reason why the Fermi liquid picture breaks down and gets replaced by collective bosonic excitations can be answered at several different levels of sophistication. Since a dissertation reflects the thinking of its author about these problems, we present here a simple, illuminating argument. Let's consider spinless, non-interacting fermions in d-dimensions with isotropic spectrum $\epsilon(\mathbf{k})$, whose Hamiltonian is

$$H_0 = \sum_{\mathbf{k}} \left[\epsilon(\mathbf{k}) - \mu\right] c^{+}_{\mathbf{k}} c_{\mathbf{k}}, \tag{1.31}$$

where μ is the chemical potential.The operator, describing density fluctuation in momentum space is

$$\rho(\mathbf{q}) = \sum_{\mathbf{k}} c^{+}_{\mathbf{k}} c_{\mathbf{k}+\mathbf{q}}, \tag{1.32}$$

which is bosonic in nature since it is a bilinear of fermionic operators. Its response function is given by the well-known Lindhard formula[73, 72] as

$$\chi(\omega,\mathbf{q}) = \int \frac{d^d k}{(2\pi)^d} \frac{n_{\mathbf{k}} - n_{\mathbf{k}+\mathbf{q}}}{\omega + i\delta + \epsilon(\mathbf{k}) - \epsilon(\mathbf{k}+\mathbf{q})}, \tag{1.33}$$

where $n_{\mathbf{k}}$ is the Fermi distribution function and $\delta \to 0^+$. At $|\mathbf{q}| \ll k_F$ and $|\omega| \ll \mu$, the integral is dominated by terms close to the Fermi surface. In one-dimension, the Fermi surface consists of two points as $\pm k_F$, and

$$\chi(\omega, \mathbf{q}) = \frac{q}{2\pi} \left(\frac{1}{\omega + i\delta - v_F q} - \frac{1}{\omega + i\delta + v_F q} \right), \tag{1.34}$$

where v_F is the Fermi velocity. Each term in Eq. (1.34) has a pole structure and represents the Green's function of a massless bosonic mode with linear spectrum $\omega = \pm v_F q$, propagating in the positive or negative direction in one dimension. The poles clearly indicate that these are long living, coherent bosonic modes in one dimension. In $d > 1$ space dimension, however, additional angular integrations remain, which smear out eventually the sharp Dirac-delta peaks in $\mathrm{Im}\chi(\omega, \mathbf{q})$ and yield brunch-cut singularities. Thus, already for non-interacting, higher dimensional fermions, the low energy spectrum of density excitations is exhausted by the incoherent background of electron-hole pairs.

The relevance of the one-dimensional case is further corroborated upon realizing that the fermionic field operator can be decomposed into right- and left-moving fermions as

$$\Psi(x) \approx \exp(ik_F x) R(x) + \exp(-ik_F x) L(x), \tag{1.35}$$

where

$$R(x) = \sum_{k \sim 0} \exp(ikx) c_{k_F + k}, \qquad L(x) = \sum_{k \sim 0} \exp(ikx) c_{-k_F + k}, \tag{1.36}$$

and the k summation is restricted for momenta close to each Fermi point as $|k\alpha| \ll 1$ with α an ultraviolet regulator. Then, to a good approximation, the Fourier transform of the long wavelength part of the above density fluctuation operator is decomposed as

$$\rho(x) \approx \sum_{r=\pm} \rho_r(x) \text{ with } \rho_+ = R^+(x) R(x) \text{ and } \rho_- = L^+(x) L(x). \tag{1.37}$$

The Fourier transform of $\rho_r(x)$ satisfies an almost bosonic commutator,

$$[\rho_r(p), \rho_{r'}(p')] = \delta_{r,r'} \delta_{p,p'} \frac{Lp}{2\pi}, \tag{1.38}$$

up to a normalization factor. This allows us to define proper bosonic creation

and annihilation operators as

$$b_p = \left(\frac{2\pi}{L|p|}\right)^{1/2} \sum_r \Theta(rp)\rho_r(-p), \tag{1.39}$$

$$b_p^+ = \left(\frac{2\pi}{L|p|}\right)^{1/2} \sum_r \Theta(rp)\rho_r(p) \tag{1.40}$$

and $\Theta(x)$ is the Heaviside function. With this, the kinetic energy is written as[72, 71]

$$H_0 \simeq \sum_{p\neq 0} v_F|p|b_p^+ b_p. \tag{1.41}$$

This equation is indeed remarkable since the kinetic energy, which was initially quadratic in terms of the fermionic operators, becomes quadratic in the language of the bosonic operators, which are, however, fermionic bilinears, therefore the resulting expression is also expressed as a quartic from of fermionic operators. It is not hard to see that a quartic fermionic interaction is expressed as a quadratic form of the bosonic operators. Therefore, the main trick of bosonization is not to simplify the interaction but rather to express the kinetic energy in a clever way by properly chosen bosonic operators.

In the presence of interactions, a general one-dimensional Hamiltonian with forward scattering interaction reduces in many cases to the so-called Luttinger model[71, 71, 74, 75], which describes the Luttinger liquid universality class as

$$H = \sum_{q\neq 0} (\omega(q) + g_4(q))b_q^\dagger b_q + \frac{g_2(q)}{2}[b_q b_{-q} + b_q^+ b_{-q}^+], \tag{1.42}$$

with $\omega(q) = v_F|q|$ (v_F being the bare "sound velocity" in the non-interacting case), $g_{2,4}(q) = g_{2,4}|q|$ and g_2 results from interaction between right- and left-moving fermionic densities as $\rho_+(x)\rho_-(x)$, while the g_4 process stems from interaction of rightmovers or leftmovers among themselves as e.g $\rho_+(x)\rho_+(x)$. The latter is mostly responsible for velocity renormalization as $v = v_F + g_4$. This setting is very general, and equally describes a variety of one-dimensional models such as interacting spinless fermion system, one dimensional Bose-gases, e.g. the Tonks-Girardeau limit of a 1D Bose gas [70] is also successfully described by such an effective Hamiltonian as interacting bosons can also bosonized[76], one dimensional spin chains such a the XXZ Heisenberg model, what we discuss further below. The Luttinger liquid description also applies to multicomponent models such as spinful fermions and

accounts for spin-charge separation (a detailed discussion is available in Refs. [72, 71]).

The basic identity of bosonization involves the relation between the fermionic field operators and the bosonic field. For example, the right-going field, $R(x)$, can be expressed in terms of the LL bosons as [71]

$$R(x) = \frac{\eta_+}{\sqrt{2\pi\alpha}} \exp\left(i\phi_+(x)\right) \ , \tag{1.43}$$

where η_+ denotes the Klein factor, which is a Majorana fermionic operator and it can be neglected in many calculations. Finally,

$$\phi_+(x) = \sum_{q>0} \sqrt{\frac{2\pi}{|q|L}} \exp(-\alpha|q|/2) \left(\exp(iqx)b_q + \exp(-iqx)b_q^+\right) , \tag{1.44}$$

and a similar expression exists for the left-movers, involving $q < 0$ momenta[71, 72, 74].

Finally, let us note that instead of the parametrizing a LL with the various g interaction parameters from g-ology[77], one can introduce two parameters, characterizing all correlation function in the long time-long distance asymptotic region, which are the renormalized velocity v and the LL parameter K as

$$v = \sqrt{(v_F + g_4)^2 - g_2^2}, \tag{1.45}$$

$$K = \sqrt{\frac{v_F + g_4 - g_2}{v_F + g_4 + g_2}}. \tag{1.46}$$

For example, the γ^2 exponent in Eqs. (1.28) and (1.30) reads as

$$\gamma^2 = \frac{K + K^{-1}}{2} - 1, \tag{1.47}$$

which gives $\gamma = 0$ for the non-interacting limit, $K = 1$, in accord with the Fermi liquid theory.

The best-known example of a lattice model, leading to LL physics is the XXZ Heisenberg model, which reads as

$$H = \sum_m J \left(S_m^x S_{m+1}^x + S_m^y S_{m+1}^y\right) + J_z S_m^z S_{m+1}^z \tag{1.48}$$

where m indexes the lattice sites with lattice constant set to unity, and $J > 0$ is the antiferromagnetic exchange interaction. This can be brought to

a simpler form after a Jordan-Wigner transformation, which reads as [71]

$$S_l^+ = \exp\left(i\pi \sum_{m<l} n_m\right) c_l^+, \quad S_l^- = \exp\left(i\pi \sum_{m<l} n_m\right) c_l, \tag{1.49}$$

$$S_l^z = n_l - \frac{1}{2}, \quad n_l = c_l^+ c_l \tag{1.50}$$

where the c's are fermionic operators, or alternatively, one can think of S^+ and S^- as hard-core boson creation and annihilation operators. The XXZ Heisenberg Hamiltonian maps onto spinless 1D fermions with nearest neighbour interaction [71]:

$$H = \sum_m \frac{J}{2}\left(c_{m+1}^+ c_m + \text{h.c.}\right) + J_z n_{m+1} n_m, \tag{1.51}$$

up to an irrelevant shift of the energy. Alternatively, S_l^+ acts as a hard core boson creation operator to site l, and the model maps to the hopping problem of hard core bosons, interacting with nearest-neighbour repulsion.

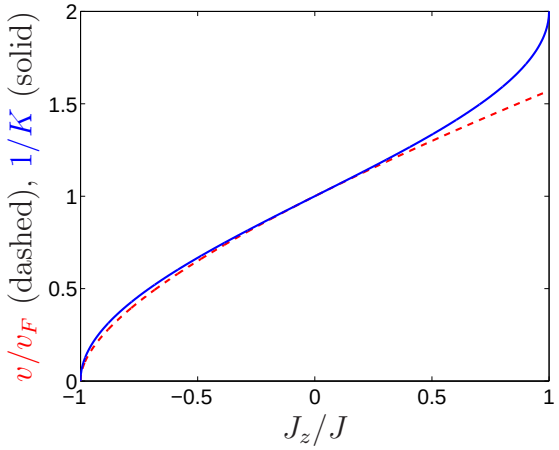

Figure 1.15: The LL parameters of the XXZ Heisenberg model are plotted as a function of the anisotropy parameter J_z.

This can conveniently be bosonized, using the steps sketched above, after going to the continuum limit [71, 72], yielding the Luttinger model in Eq. (1.42). The connection between the two models is established as $-1 \ll g_2/2v = J_z/\pi J \ll 1$ in the weak-coupling limit. The LL description remains valid for $|J_z| < J$, and the LL parameters are obtained exactly for this specific

model using the Bethe-Ansatz as

$$\frac{v}{v_F} = \frac{\pi}{2}\frac{\sqrt{1-(J_z/J)^2}}{\arccos(J_z/J)}, \tag{1.52}$$

$$K = \frac{\pi}{2[\pi - \arccos(J_z/J)]}, \tag{1.53}$$

where $v_F = J$, and these are depicted in Fig. 1.15.

At the isotropic XXX point with $J_z = J$, a Kosterlitz-Thouless quantum phase transition takes place to an antiferromagnetically ordered phase for $J_z > J$. This transition is, however, not described by the Luttinger model in Eq. (1.42), but is driven by additional terms in the Hamiltonian, outside of the realm of the Luttinger model. Their investigation is beyond the scope of the present dissertation. The $J_z = -J$ point represent a first order isotropic ferromagnetic quantum critical point, where the spectrum becomes quadratic, as is typical for a ferromagnet. In the close vicinity of this point within the gapless phase, the linear energy-momentum relationship remains valid only at very low energies, and is replaced by a quadratic relationship with increasing energy. There, bosonization only works at very low energies, when the linearized spectrum approximation works.

1.6 Experimental realization of one-dimensional systems

The LL paradigm applies to a variety of systems. Initially, quasi-one-dimensional condensed matter systems were suspected to belong to this category like the Bechgaard salts[78], and later carbon nanotubes, i.e. rolled up graphene sheets realized more faithfully LLs[79, 80, 81, 82, 83]. In particular, photoemission spectroscopy (PES) experiments[84, 85] probe directly the spectral functions in Eq. (1.28) and (1.30), yielding the non-integer power law exponents as shown in Fig. 1.16. Subsequent transport[86] as well as nuclear magnetic and conduction electron spin resonance studies[87, 88, 89] have confirmed the adequacy of the LL picture. The edge states in integer and fractional quantum-Hall states form also one-dimensional object, and are described by the LL theory[71].

Recent years have witnessed a tremendous amount of experimental advances in cold atomic systems[63]. Trapping one-dimensional bosons or fermions offers the possibility to realize LL physics with the extra tunability of system parameters such as the inter-particle interaction (tunable by a Feshbach resonance or by changing the parameters of the optical trap) or the

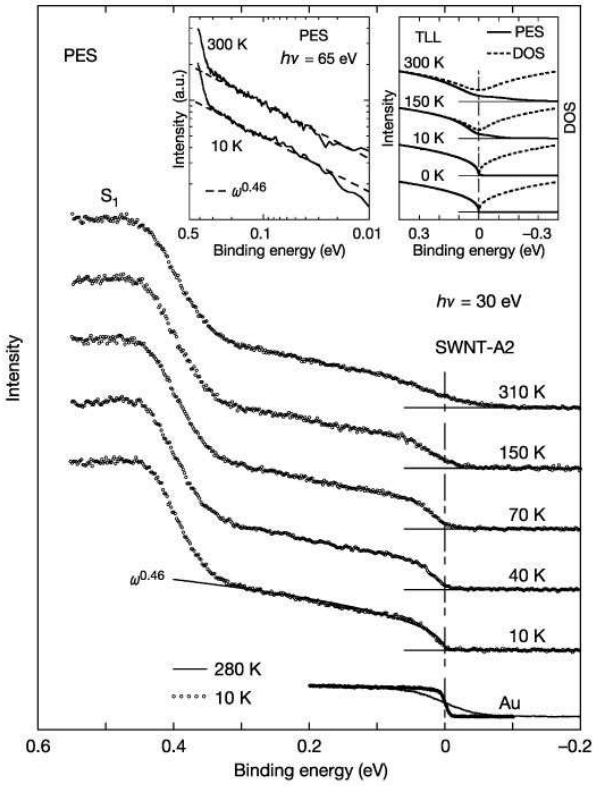

Figure 1.16: The PES spectra of single-wall carbon nanotubes. The spectral function, $|\omega|^\alpha$ ($\alpha = 0.46$), broadened by the energy resolution, is indicated by a thick solid line in the spectrum at 10 K. The spectra of Au (3D conventional metal) are also shown. The left inset shows the PES, which were measured with an energy resolution of 15 meV at $h\nu = 65$ eV, plotted on a loglog scale. The right inset shows the photoemission spectra and the densities of states (DOS) calculated for the LL state in the metallic nanotubes.

various relaxation channels (i.e. no phonons or impurities wich are ubiquitous in condensed matter systems). Ultracold fermionic gases have been realized using several atoms such as ^{40}K[90, 91, 92], ^{6}Li[93], ^{171}Yb-^{173}Yb[94], ^{163}Dy[95] and ^{87}Sr[96], and temperatures well in the quantum degeneracy regime were reached ($T < 0.1\ E_F$, with E_F the Fermi energy). All these atomic systems feature tunable interactions. Among these, 1D configurations have been realized using ^{40}K[90, 91], ^{6}Li[93], and the momentum distribution has been measured in time of flight (ToF) experiments in 2D[96] and 3D[92, 94] Fermi gases. Therefore, by applying ToF imaging or momentum resolved rf

spectroscopy[90], the observation of the momentum distribution of Eq. (7.13) is within reach for 1D fermions [90]. Furthermore, the specific momentum distribution of a LL has already been observed in the Tonks-Girardeau limit of 1D Bose systems[70], which exhibit fermionic properties in this strongly interacting regime.

The peculiarities of 1D systems were first demonstrated in the so-called quantum Newton's cradle experiment[69], sketched schematically in Fig. 1.17. Already the classical, idealized Newton's cradle when several balls are simultaneously in contact, can only approximately be explained by just the exchange of specific momentum values[97]. A 1D Bose gas made of ^{87}Rb atoms, initially prepared in a highly out of equilibrium momentum superposition state of right- and left-moving atoms, was evolved in time without any noticeably sign of equilibration even after thousands of collisions. In 1D, such system with point-like interparticle interactions realizes the Lieb-Liniger gas[98], which is Bethe-Ansatz integrable. This means in this case, that there are as many constants of motion as degrees of freedom (i.e. Bose particles), therefore the system's motion in phase space is restricted by the constants of motion. As a result, ergodicity breaks down and the gas does not thermalize, as was observed in the momentum distribution after several cycles, which retained a typical two-peak structure, characteristic to the initial state. When the same experiment was repeated using two- or three dimensional gases, which are not integrable, thermalization sets in immediately even within the first period.

Coupled condensates are also useful to mimic LL behaviour. Using atom chips, a 1D Bose gas with a few thousand atoms can be trapped in the 1D quasicondensate regime at very low temperature[67], and the 1D gas can be split into two 1D quasicondensates. Such a 1D quasi-condensate can be thought of as a LL, since the excitation spectrum grows linearly with the momentum. By the application of radio frequency (rf) induced adiabatic potential, the height of the barrier between the two condensates can be adjusted by controlling the amplitude of the applied rf field. This allows one to achieve both Josephson coupled and fully decoupled quasicondensates. The fluctuations of the relative phase of the two condensates are measured by the coherence factor

$$\Psi(t) = \frac{1}{L}\left|\int dx \exp\left[i(\theta_1(x,t) - \theta_2(x,t)\right]\right|, \tag{1.54}$$

where $\theta_{1,2}$ are the phases of the two condensates obtained after the splitting, respectively, and L is the length of the analyzed signal. This is predicted to behave, using a LL description, as $\Psi(t) \sim \exp(-(t/t_0)^{2/3})$ with t_0 a decay time constant.

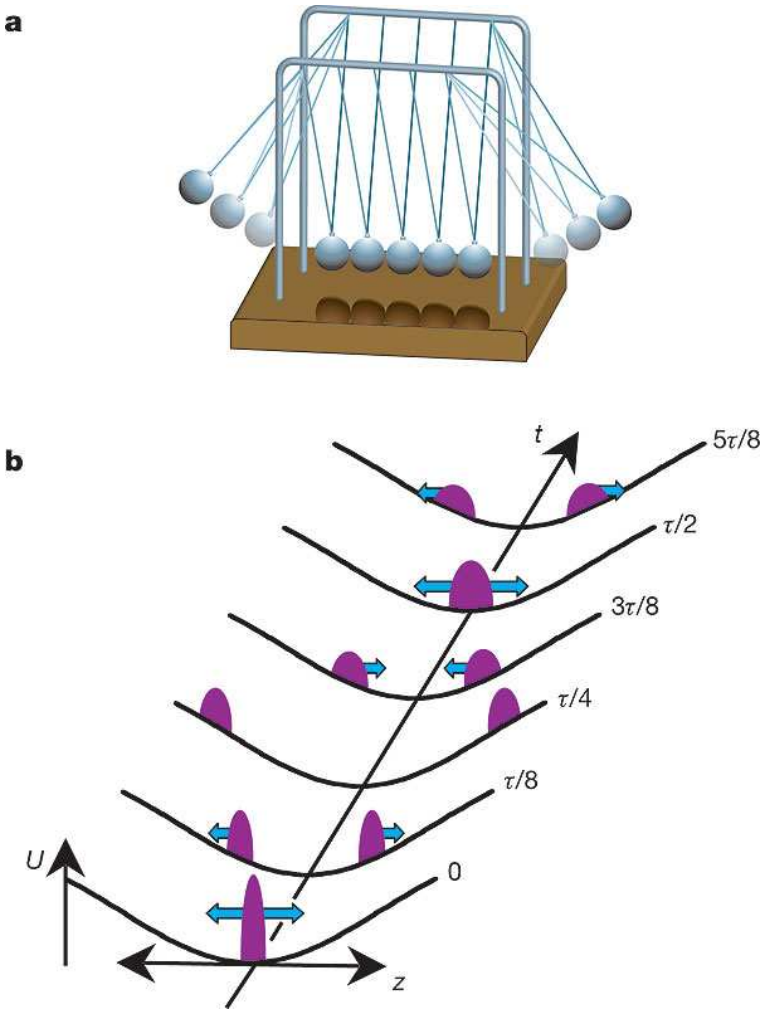

Figure 1.17: a. Visualization of a classical Newton's cradle[97]. b. Sketches at various times of two out of equilibrium clouds of atoms in a 1D anharmonic trap. Initially, the atoms are prepared in a momentum superposition state of right and left moving atoms. The two parts of the wavefunction oscillate out of phase with each other with a period τ. Each atom collides with the opposite momentum group twice every full cycle, for instance, at $t = \tau/2$. Anharmonicity causes each group to gradually expand, until ultimately the atoms have fully dephased. Even after dephasing, each atom still collides with half the other atoms twice each cycle.

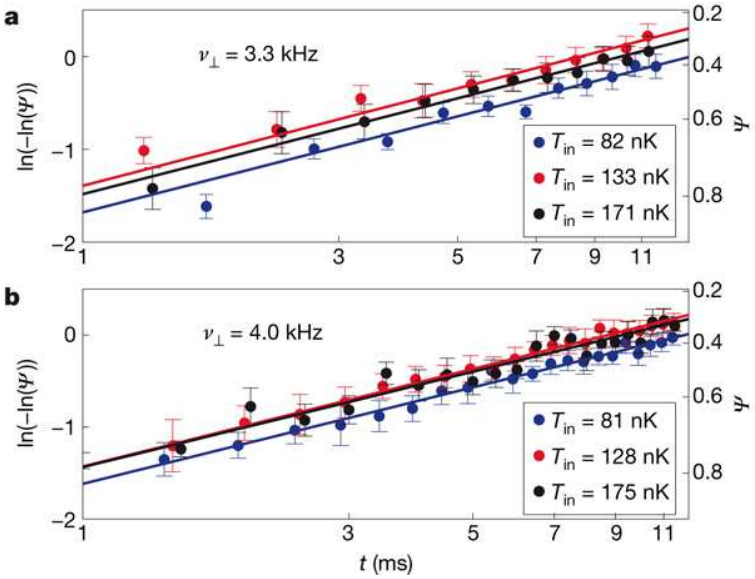

Figure 1.18: Double logarithmic plot of the coherence factor, Ψ as a function of time for decoupled 1D condensates. Each point is the average of 15 measurements, and error bars indicate the standard error. The slopes of the linear fits are in good agreement with a 2/3 exponent, coming from a LL description, from Ref. [67].

Chapter 2

Main objectives

Understanding the non-equilibrium dynamics and the electronic properties of novel exotic materials are in the focus of contemporary condensed matter physics. When these two are combined, fascination is guaranteed. We will investigate the non-equilibrium transport properties of Dirac electrons in two dimensions: for most nanoelectronic applications, the interest is in the high electric field regime since devices are usually operated at or near the current saturation limit. So far, little has been known about graphene and topological insulators under those conditions, while most of their equilibrium properties are understood at least on a qualitative level. Quantum transport and non-linear responses driven by finite external fields represent a genuine non-equilibrium phenomenon, giving rise to e.g. dielectric breakdown or Bloch oscillations. The quantum aspect of these effects is particularly pronounced in reduced dimensions. Therefore, two-dimensional massless Dirac electrons in finite electric fields, one of the subjects of this work, provide a fascinating setting for studying these issues. This will also provide us with the direct observation of several phenomena from high-energy physics, such as Schwinger's pair production. In addition, increasing amount of interest originates in this direction from the physics of ultracold atoms, where out-of-equilibrium preparation and investigation of model systems (including the honeycomb lattice) is possible.

Strong electric field can have a peculiar effect in bilayer graphene, consisting of two closely stacked graphene monolayers. When changed adiabatically, a perpendicular electric field leads to gap opening at the charge neutrality point. How non-adiabaticity affects the physical properties of bilayer graphene and whether temporal changes of the gap yield any peculiar phenomenon is a relevant question from both experimental and theoretical perspective. In addition to non-equilibrium time-evolution, the properties of the steady state reached after a time periodic perturbation are so far largely

unexplored.

The search for topologically non-trivial materials is becoming very active recently, and we will also characterize the topological benefits of driving quantum systems periodically. In particular, the fate of a quantum spin-Hall insulator, the first topological insulator realized experimentally, will be investigated in a strong electromagnetic field.

Switching on interactions in a non-equilibrium fashion is a different, though equally exciting way of reaching exotic states of matter. In particular, non-equilibrium dynamics and strong-correlation phenomena in quantum many body systems represent equally challenging fields of physics. The combination of these two fields, namely when strongly correlated systems are driven out-of-equilibrium, we face a real challenge. Experimental advances on ultracold atoms [63] have made the time dependent evolution and detection of quantum many-body systems possible, and in particular, quantum quenching the interactions by means of a Feshbach resonance or time dependent lattice parameters has triggered enormous theoretical [51, 66, 98] and experimental [67, 68, 69, 70] activity. Inspired by these, we'll study and characterize the non-equilibrium properties of Luttinger liquids after a temporal change of the interaction parameter.

Chapter 3

Non-linear electric transport in graphene

3.1 Longitudinal transport

A strong electric field produces peculiar phenomena in a variety of systems. First of all, it was predicted to create particle-antiparticle pairs, starting from the Dirac equation, which has a long history pioneered by the discovery of the Klein paradox[5]. In 1951, Schwinger derived a formula for the pair creation probability[99] and found that the Dirac vacuum in an electric field is unstable against creation of particle-antiparticle pairs.

This non-perturbative particle creation mechanism in strong external fields has a wide range of applications; not only the original QED problems but also pair creation in non-Abelian electromagnetic fields and gravitational backgrounds or close to a Mott transition[45]. For electron-positron pair creation, an electric field strength of the order 10^{16} V/cm is needed, which is beyond current technological capabilities, and it still calls for its first, unambiguous experimental observation, which can be obtained in graphene and related systems.

Additionally, in condensed matter quantum transport and non-linear responses driven by finite external fields represent a genuine non-equilibrium phenomenon, giving rise to e.g. dielectric breakdown or Bloch oscillations[100]. The quantum aspect of these effects is particularly pronounced in reduced dimensions. Therefore, two-dimensional Dirac electrons in finite electric fields, the subject of this chapter (based on our work in Refs. [101, 102]), provide a fascinating setting for studying these issues.

Electronic transport in a finite electric field is accounted for successfully by the Drude theory in normal metals. In graphene, however, special features

of Dirac electrons should be included: (i) their velocity is pinned to the "light cone" Fermi velocity, v_F, (ii) relativistic particles undergo pair production in strong electric fields, as predicted by Schwinger[99], and (iii) a uniform electric field modifies locally the geometry of the Fermi surface by moving the Dirac point around in momentum space (Eq. (3.4)). Since massless Dirac electrons can be thought of as being critical, this can lead to the production of excited states, and should leave its fingerprints on transport in finite electric fields.

Ohm's law predicts that in a metal, the current (j) grows linearly with the electric field (E) as

$$j = \sigma E, \tag{3.1}$$

for small fields, as was reformulated by G. Kirchhoff. For graphene, the linear relationship has been confirmed, though there is no agreement on the explicit value of the dc conductivity, σ from the theoretical side. In particular, it was shown[9] that the dc conductivity of 2D massless Dirac electrons at $T = 0$ per spin and valley is given by[103, 104]

$$\lim_{\Gamma\to 0}\lim_{\omega\to 0}\sigma(\omega,\Gamma) = \frac{e^2}{\pi h}, \qquad \lim_{\omega\to 0}\lim_{\Gamma\to 0}\sigma(\omega,\Gamma) = \frac{e^2\pi}{8h} \tag{3.2}$$

within linear response, where Γ is the scattering rate and ω is the external frequency. In general, electric transport depends on several parameters such as frequency, temperature, electric field and scattering rate (ω, T, E, Γ), and physical quantities depend strongly on how the $(\omega, T, E, \Gamma) \to 0$ limit is taken[105, 9].

In the followings, we will validate explicitly Eq. (3.1) for small fields and show, that for strong electric fields, graphene does not obey it any more, but follows a non-linear current-voltage characteristics. Our results are summarized in Table 3.1.

classical	Kubo	Schwinger/Kibble-Zurek
$t \ll h/W$	$h/W \ll t \ll 1/\sqrt{v_F e E}$	$1/\sqrt{v_F e E} \ll t \ll t_{Bloch}$
$j_x \sim Et$	$j_x \sim E$	$j_x \sim tE^{3/2}$

Table 3.1: Temporal evolution of the non-equilibrium current for clean graphene. Bloch oscillations show up for $t \gtrsim t_{Bloch} \sim 1/eaE$[100] with a the honeycomb lattice constant.

We focus on the 2+1 dimensional Dirac equation in a uniform, constant electric field in the x direction, switched on at $t = 0$, through a time dependent vector potential as $\mathbf{A}(t) = (A(t), 0, 0)$ with $A(t) = Et\Theta(t)$. The

resulting time dependent Dirac equation, describing low energy excitations around one of the Dirac points for clean graphene, is written as

$$H = v_F[\sigma_x(p_x - eA(t)) + \sigma_y p_y] + \Delta\sigma_z, \qquad i\partial_t \Psi_p(t) = H\Psi_p(t). \tag{3.3}$$

For the moment, we set $\Delta = 0$, but will return to the finite Δ case at the end of this chapter.

Due to the (pseudo)spin structure in Eq. (3.3), it represents a natural formulation for the study of Landau Zener dynamics, as emphasized in the Introduction. We first perform a time dependent unitary transformation [46], which rotates it into the instantaneous basis $U^+HU = \sigma_z\epsilon_p(t)$, where the resulting energy spectrum $\epsilon_p(t)$ is given by

$$\epsilon_p(t) = v_F\sqrt{(p_x - eA(t))^2 + p_y^2}. \tag{3.4}$$

The transformed time dependent Dirac equation reads

$$i\partial_t\Phi_p(t) = \left[\sigma_z\epsilon_p(t) - \sigma_x\frac{v_F^2 p_y eE}{2\epsilon_p^2(t)}\right]\Phi_p(t), \qquad \Psi_p(t) = U\Phi_p(t). \tag{3.5}$$

Note that the electric field appears in the energy spectrum and induces off-diagonal terms in the Hamiltonian, which is a consequence of the explicit time dependence of the unitary transformation ($-iU^+\partial_t U$). The spinor is given by

$$\Phi_p(t) = \begin{pmatrix} \alpha_p(t) \\ \beta_p(t) \end{pmatrix}, \tag{3.6}$$

with the initial condition $\alpha_p(0) = 0$ and $\beta_p(0) = 1$, implying half-filled graphene, (the lower/upper Dirac cone is occupied/empty).

After switching on the electric field, the current acquires a finite expectation value, which, however, requires the knowledge of the density of excited, positive energy states, $n_p(t) = |\alpha_p(t)|^2$ as

$$\langle j_x\rangle_p(t) = -ev_F\left[\frac{v_F(p_x - eEt)}{\epsilon_p(t)}(2n_p(t) - 1) - 2\frac{\epsilon_p(t)}{v_F eE}\partial_t n_p(t)\right]. \tag{3.7}$$

The first term is the current from particles residing on the upper or lower Dirac cone, while the second one describes interference between them, and is responsible for Zitterbewegung. Using QED terminology, the first and second term is referred to as conduction and polarization current, respectively[45]. In condensed matter, these are called intraband and interband contributions, respectively. The term independent of $n_p(t)$, namely $ev_F^2(p_x - eEt)/\epsilon_p(t)$

vanishes at half filling after momentum integration. In QED, this originates from charge conjugation symmetry[45], while in graphene, the same result is obtained by taking the full honeycomb lattice into account as in Ref. [106].

Before switching on the current, the upper/lower Dirac cone is empty/fully occupied. The quantity $n_p(t)$ measures the number of particles created by the electric field in the upper cone through Schwinger's pair production[99]. In graphene, instead of particle-antiparticle pairs, electron-hole pairs are created. Therefore, the basic quantity to determine transport through graphene is $n_p(t)$.

In the weak electric field case, only the polarization term contributes to the current, and one can solve Eq. (3.5) perturbatively in the electric field to obtain $n_p(t)$. After taking valley and spin degeneracies into account, the dc conductivity is obtained[101] as

$$\sigma = j/E = e^2\pi/2h, \tag{3.8}$$

in accordance with Ref. [106].

This is the value of the ac conductivity at finite frequencies obtained from the Kubo formula[103, 104, 3] and measured also[14], and since the model does not contain any additional energy scale, which would change the value of the ac response down to $\omega \to 0$, the same value for the dc conductivity sounds plausible. In this regime, all electrons propagate with the maximal velocity v_F, therefore the current is saturated, independent of time. Within our approach, the small field response is dominated by the Zitterbewegung, i.e. electric field induced interband transition. The ultrashort time transient response ($tW \ll h$ with W the bandwidth) is non-universal and follows from classical consideration[101] as well.

For the general time and electric field dependence, one can use the analogy between Eq. (3.3) and the Landau-Zener model in Eq. (1.23). Using Eq. (1.24) in the strong field, long time (specified in Eq. (3.12)) regime, we obtain[45, 107, 99] from Eq. (1.24)

$$n_p(t) = \Theta(p_x)\Theta(eEt - p_x) \exp\left(-\frac{\pi v_F p_y^2}{eE}\right), \tag{3.9}$$

which is the massless, two-dimensional pair production rate by Schwinger[99, 45]. It applies when $(p_x, eEt - p_x) \gg |p_y|$.

The physics behind Eq. (3.9) can be understood as follows: two levels at $\pm p_x$, weakly coupled by p_y level cross with time, ending up at $\pm(p_x - eEt)$. The transition is completed when both the initial and final levels are well separated, in which case the mixing between them is given by Eq. (3.9),

as plotted in Fig. 3.1. Eq. (3.9) describes the highly non-thermal, non-equilibrium momentum distribution in the upper Dirac cone, while $1 - n_p(t)$ is that in the lower cone.

In this regime, the current is dominated by the conduction (intraband) part as

$$\langle j_x \rangle(t) = \frac{2e^2 E}{\pi^2} \sqrt{v_F e E t^2}, \tag{3.10}$$

exhibiting a linear increase in time, which appears to be quite analogous to what is observed for electrons in a conventional parabolic band. However, the origin of the time dependence is completely different: it stems from the increasing number of pairs due to pair production à la Schwinger, each contributing with the same velocity v_F, as opposed to the continuously accelerated fixed number of normal electrons in strong fields. The $E^{3/2}$ dependence under distinct conditions has also shown up in Refs. [108, 109, 105].

The expectation value of the total number of particles-hole pairs created, $N(t)$ is obtained from $n_p(t)$:

$$N(t) = \frac{2}{\pi^2} \int \mathrm{d}\mathbf{p} n_p(t) = \frac{2eE}{\pi^2 v_F} \sqrt{v_F e E t^2}. \tag{3.11}$$

This reproduces Eq. (3.10) via $\langle j_x \rangle(t) = e v_F N(t)$. This equation is related to the quench dynamics through a quantum critical point (QCP)[52], and can be reobtained using the Kibble-Zurek mechanism[54, 55, 101]. This also predicts the $tE^{3/2}$ scaling of the total defect density for Eq. (3.3), similarly to Eq. (3.11), linking the non-linear transport in graphene to critical phenomena.

Putting the weak and strong field results together, the low field, perturbative response is dominated by interband contributions, and can be regarded as a manifestation of Zitterbewegung. With increasing field, a large number of electron-hole pairs are created, and intraband processes take over, producing non-linear transport.

This crossover is determined by the dimensionless time-scale, which can be obtained by comparing our system to the Landau Zener model as[110]

$$\tau_{cross} = \sqrt{v_F e E t^2}. \tag{3.12}$$

For $\tau_{cross} \ll 1$, no level crossing occurs, and we can use perturbation theory to estimate the current, therefore we are in the Kubo regime, while for $\tau_{cross} \gg 1$, the Schwinger mechanism is operative. In Landau Zener language, the level crossing is completed once $\tau_{cross} \gg 1$. The total number of pairs created is non-perturbative in the electric field.

So far we have discussed the real time evolution of the current after the switch-on of the electric field in the Dirac equation, summarized in Table 3.1.

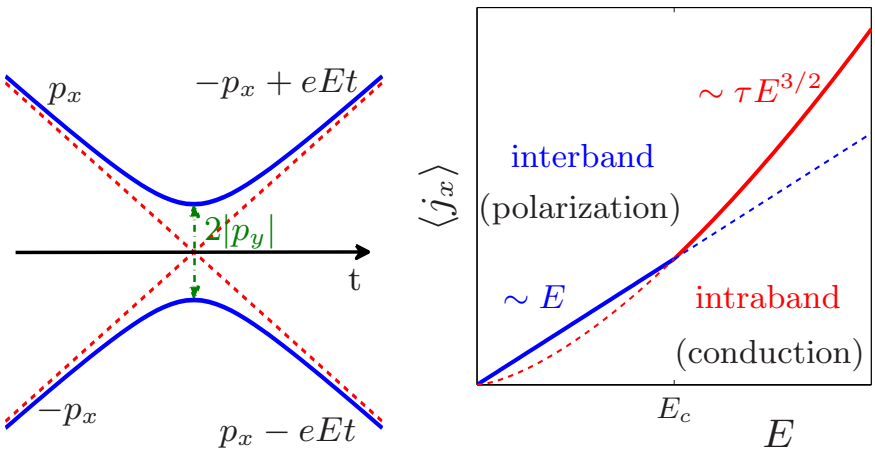

Figure 3.1: Left panel: visualization of the temporal evolution of the Landau Zener dynamics. Right panel: schematic picture of the current-electric field characteristics for graphene. Interband transitions are overwhelmed by intraband ones with increasing electric field, and the dominant contribution to the measured current changes in character from polarization to conduction.

In ideal clean graphene, for long enough times, Bloch oscillation would set in due to the underlying honeycomb lattice structure. We have thus simulated the switch-on of the electric field on the honeycomb lattice numerically by solving the resulting differential equation, following from performing the Peierls substitution in $f(\mathbf{k})$, defined in the Introduction. We have recovered all three regions[111] from Table 3.1 with the correct numerical coefficients, before Bloch oscillations set in. Therefore, this established the applicability of the Dirac description to study the non-equilibrium response of graphene.

The next question which naturally arises is that what happens away from this highly idealized limit without any sources of dissipation or scattering. In the simplest approach, the time t should replaced by an appropriate scattering time[106], τ_{sc} in the spirit of Drude theory, arising from scattering due to phonons or impurities. Alternatively, in ballistic samples, ballistic flight time from the finite flake size, $\tau_b = L_x/v_F$[108] would assume that role.

The observation of non-linear electric transport requires, from Eq. (3.12), an electric field as

$$E > E_c = 1/v_F e\tau^2, \tag{3.13}$$

where $\tau = \min(\tau_{sc}, \tau_b, \tau_\Delta)$ is the shortest of the additional restricting time scales (with τ_Δ defined below). Ballistic transport on the (sub)μm scale implies $\tau \sim 0.1 - 1$ ps, giving $E_c \sim 10^3 - 10^5$ V/m[112].

The exponents of the electric field of the linear (trivially 1) and non-linear (3/2) regime do not differ significantly, and the measured current is

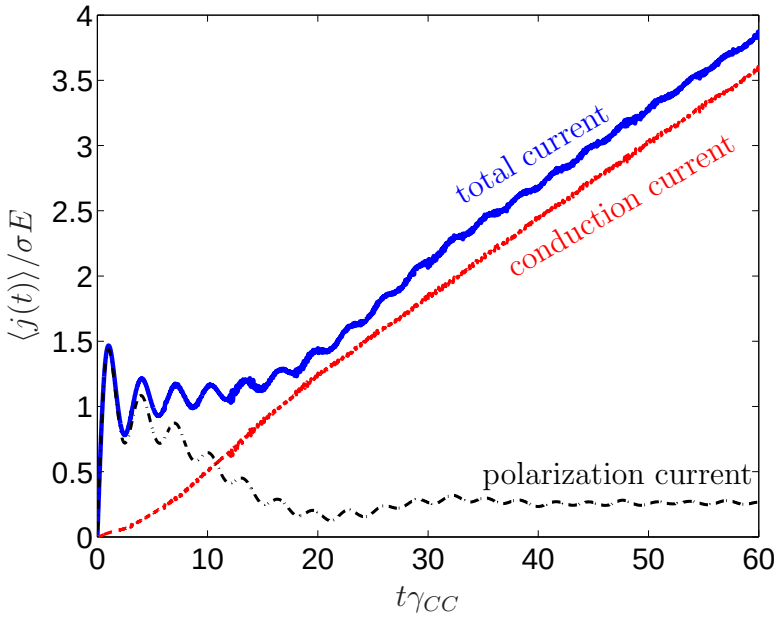

Figure 3.2: The electric current together with its components is shown as a function of time, after switching on the electric field, $eEv_F/\gamma_{cc} = 0.004$, from the numerical solution[111] of the time dependent Schrödinger equation on the honeycomb lattice, γ_{cc} is the nearest neighbour hopping and σ is defined in Eq. (3.8). All regions agree with the predictions of the Dirac equation, summarized on Table 3.1.

expected to show a change of slope as a function of the electric field in the crossover region, and an extended electric field window would be required to reveal the non-integer exponent, as shown in Fig. 3.1. The linear (small E) region is independent of time through Eq. (3.8), naturally accounting for the scattering independent minimal conductivity. We emphasize that in both regions, the current is related to $n_p(t)$. Thus, even the linear response regime witnesses pair production.

Recent transport measurements of undoped graphene devices have revealed superlinear current-voltage characteristics[113] for strong voltages, i.e. $I \sim V^{\alpha}$, with α close to the predicted one (1.5), depicted in Fig. 3.3, thus confirming our predictions and the realm of Schwinger's pair production for graphene. However, contrary to expectations, only low mobility samples, implying large scattering rate, provided an exponent close to 1.5, increasing mobility yielded an exponent closer to 1. The origin of this counterintuitive behaviour calls for further studies on non-equilibrium graphene in the presence of defects.

These results are also relevant for other systems with possible Dirac

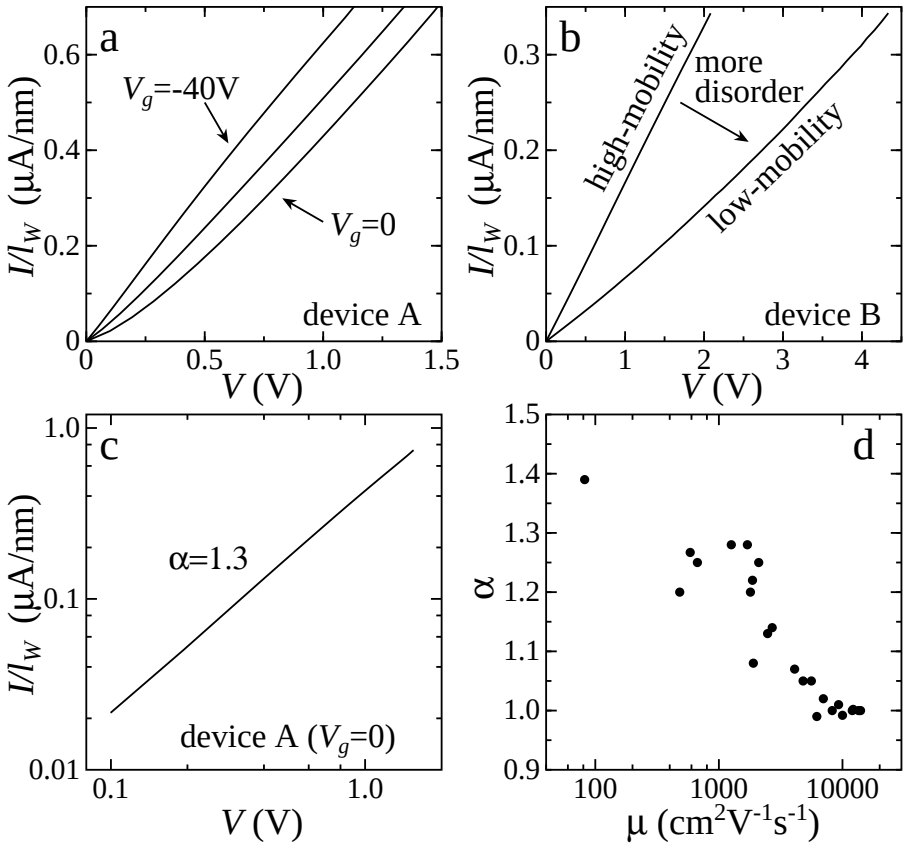

Figure 3.3: Electronic transport in graphene: a) Measured current I per unit of lateral length l_W vs source-drain voltage V in a low- mobility sample for different gate voltages: $V_g = 0, 20, 40$V, $V_g = 0$ corresponds to the Dirac point. The length between the voltage electrodes $l = 1.1$ μm and $l_W = 1.1$ μm. b) Measured I-V in a high-mobility sample, at the Dirac point, before and after the introduction of defects through electronic bombardment, $l = 2.2$ μm and $l_W = 550$ nm. c) Double-logarithmic scale plot of $I - V$. d) Exponent α as a function of mobility for different devices, l varies from 0.9 to 5.9μm and l_W from 70 to 1500 nm.

fermions such as the organic conductor[114] α-(BEDT-TTF)$_2$I$_3$ with a tilted Dirac cone, or for topological insulators. Dirac fermions can be realized in cold atoms in an appropriate optical lattice (half filled honeycomb, kagome and triangular lattices), without any source of dissipation or scattering, a regime not naturally accessible for materials-based condensed matter systems. The momentum distribution, Eq. (3.9), reveals the effect of the driving electric field before Bloch oscillations set in[100]. The pairs created in-

crease the energy of the system as $\sim t^2 E^{5/2}$, which, together with the highly non-thermal momentum distribution of Bloch states, can be measured after releasing the trap. This could be a first direct experimental observation of the Schwinger mechanism with microscopic resolution as well.

3.2 (Spin-) Hall effect

The hallmark of (pseudo-) relativistic massive Dirac electrons[115] is a single quantum Hall step around half-filling in the absence of magnetic field between $\sigma_{xy} = \pm e^2/2h$. By extending the technique developed in the first part of this chapter, we pose and answer the question: how this picture gets modified in the presence of strong electric fields. A strong electric field alters not only the longitudinal transport[101], but is expected to modify the transverse conductivity, involving the non-equilibrium quantum (spin-) Hall breakdown. Common wisdom has it that while there are no power law corrections to the integer Hall conductivity for weak electric fields, with its quantization 'topologically' protected, there can be exponentially small corrections. When these grow with field, quantization breaks down.

Motivated by the previous exact solution of the non-equilibrium, longitudinal current response of gapless graphene, we now focus on the time evolution of the Hall current for massive Dirac Fermions, after switching on a *longitudinal* electric field. We show that a *stationary transverse* current develops for long times, characterized by a quantized Hall conductivity for weak fields, crossing over to a power-law decaying Hall response with increasing field. This result is expected to apply to the quantum spin-Hall breakdown of graphene[116] as well as for the related[33] surface Hall and magnetoelectric effect in TI.

The adequate Hamiltonian around the Dirac point in graphene[3] or on the surface state of a 3D TI[117, 33], as in Eq. (1.22) in the presence of a uniform, constant electric field ($E > 0$) in the x direction is given by Eq.(3.3). Here, $\Delta > 0$ is the mass gap, originating from e.g. the intrinsic spin-orbit coupling (SOC) in graphene[35], or from a thin ferromagnetic film covering the surface of TI.

After a unitary transformation, bringing Eq. (3.3) to the instantaneous basis, similarly to the longitudinal case, we get

$$i\partial_t \Phi_p(t) = \left[\sigma_z \varepsilon_p(t) - \sigma_x \frac{v_F e E \sqrt{(v_F p_y)^2 + \Delta^2}}{2\varepsilon_p^2(t)} \right] \Phi_p(t), \tag{3.14}$$

with $\varepsilon_p(t) = \sqrt{\Delta^2 + v_F^2((p_x - eA(t))^2 + p_y^2)}$. The spinor structure and initial

condition are identical to those in Eq (3.6).

In contrast to the gapless Dirac equation, Eq. (3.14) contains intrinsic energy scales (due to the finite Δ), whose ratio determines the fate of the system. the diagonal energy (Δ) and off-diagonal coupling ($v_F eE/2\Delta$), which triggers transitions between the two gap edges or levels using Landau-Zener (LZ) terminology[110]. A crossover from weak to strong field is thus expected at $E \sim \Delta^2/v_F e$, irrespective of the explicit value of t, as we confirm below by a more detailed analysis.

The quantity we focus on is the time dependent transverse charge current, $j_y = -ev_F\sigma_y$, with spin current and conductivity differing only by a factor $1/ev_F$. For TI, j_y coincides with the topological magnetic field induced *parallel* to the applied electric field (after the $\pi/2$ rotation of the spin, leading to Eq. (3.3)) and monitors the magnetoelectric effect[118, 117]. The current reads as

$$\langle j_y\rangle_p(t) = -\frac{ev_F\Delta}{\varepsilon_p(t)}\left(\frac{\partial_t\left[\varepsilon_p^2(t)\partial_t n_p(t)\right]}{v_F eE((v_F p_y)^2+\Delta^2)} + \frac{v_F eE}{2\varepsilon_p^2(t)}\left(2n_p(t)-1\right)\right), \quad (3.15)$$

which depends only on $n_p(t) = |\alpha_p(t)|^2$ and its time derivatives, which parallels completely with the longitudinal case discussed previously. The short time limit of the Hall response exhibits peculiar behaviour, similarly to the longitudinal one, as discussed in Ref. [102], but we focus on the more relevant long time behaviour.

In the long time limit ($t \gg \min[1/\Delta, \sqrt{1/v_F eE}]$), we can use again the analogy of Eq. (3.14) to the Landau-Zener problem[110, 101] in Eq. (1.23) to determine $n_p(t)$ via Eq. (1.24):

$$n_p(t) = \Theta(p_x(eEt-p_x))\exp\left(-\frac{\pi[(v_F p_y)^2+\Delta^2]}{v_F eE}\right), \quad (3.16)$$

which is the extension of Eq. (3.9) to the case of a finite gap. In this limit, the second term in Eq. (3.15) dominates, and the transverse current reaches a time independent value, as opposed to the long time limit of the longitudinal current in Eq. (3.10), which increases linearly with time, as

$$j_y(t) = \sigma_{xy}E \quad (3.17)$$

with

$$\sigma_{xy} = \frac{(ev_F)^2\Delta}{4\pi h}\int d\mathbf{p}\frac{1-2n_p(t)}{\varepsilon_p^3(t)} \approx \frac{e^2}{2h}\mathrm{erf}\left(\sqrt{\frac{\pi\Delta^2}{v_F eE}}\right), \quad (3.18)$$

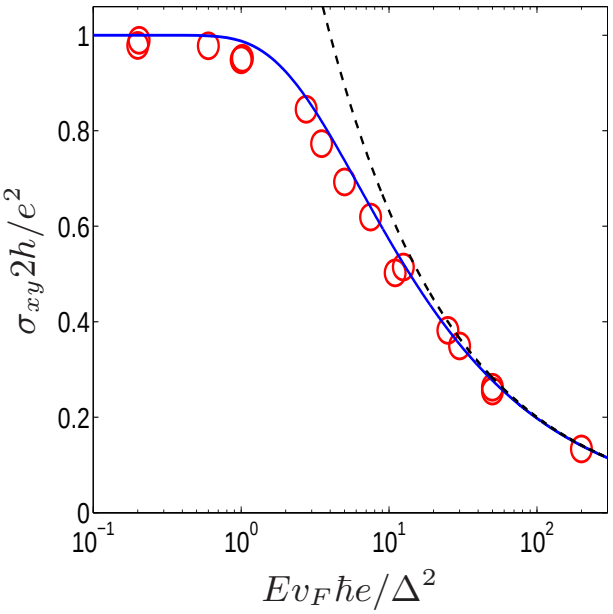

Figure 3.4: The long time limit of the Hall conductivity is plotted as a function of the applied longitudinal electric field. Quantization breaks down when $E \sim \Delta^2/\hbar v_F e$. The red circles denote the numerical data from the numerical solution of the Dirac equation, Eq. (3.14), the black dashed line is the approximate expression from Eq. (3.20) at large fields.

with erf(x) being the error function. The structure of the non-equilibrium Hall conductivity at long times (Eq. (3.18)) parallels closely with the conventional equilibrium Kubo expression[119, 120] after shifting the momentum with the vector potential and replacing the equilibrium Fermi functions with the non-equilibrium momentum distributions, Eq. (3.16). Alternatively, Eq. (3.18) reflects the competition between Berry's curvature ($\Omega_p = v_F^2\Delta/2\varepsilon_p^3(t)$), protecting quantization[32] and the difference of momentum distributions in the upper ($n_p(t)$) and lower ($1 - n_p(t)$) Dirac cones in the numerator, spoiling it. When the two distributions are comparable due to tunneling from the lower to the upper Dirac cone, the gap becomes irrelevant, and the conductivity decays.

In the limit of small fields ($E \ll \pi\Delta^2/v_F e$), we recover its quantized value as

$$\sigma_{xy} = \frac{e^2}{h}\int d\mathbf{p}\frac{\Omega_p}{2\pi} = \frac{e^2}{2h}, \tag{3.19}$$

in agreement with Eq. (1.21), without higher order perturbative or power law (in E) corrections. The additional terms contain the non-perturbative, exponential factor $\exp(-\pi\Delta^2/v_F eE)$, signaling the robustness of Hall quantiza-

tion [121] and the half-integer quantized magnetoelectric polarizability[118]. In the strong field limit ($E \gg \pi\Delta^2/v_F e$), it decays as

$$\sigma_{xy} = \frac{e^2}{2h}\frac{2\Delta}{\sqrt{v_F e E}}. \tag{3.20}$$

For TI with a mass gap ($\Delta \neq 0$), the magnetization produced by surface currents probes the Hall conductivity through the topological magnetoelectric effect, and the magnetization *parallel* to the electric field follows Eq. (3.18): its quantization breaks down with increasing field similarly to the Hall response.

Assuming a small gap of the order of 0.01-1 K (typical for the intrinsic SOC of graphene[35, 122] or TI) the crossover field is 0.001-10 V/m for $v_F \sim 10^6$ m/s, easily accessible experimentally. The Hall conductivity together with numerical results on the Dirac equation is shown in Fig. 3.4. The agreement between the analytically and numerically obtained conductivities is excellent.

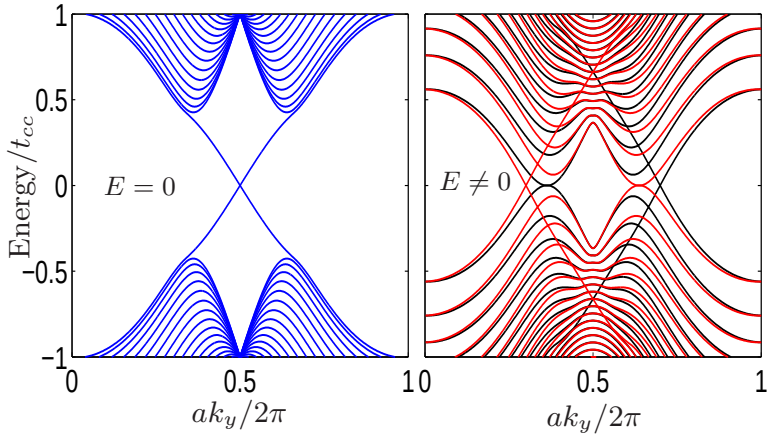

Figure 3.5: The energy spectrum of a spin-Hall insulator[35] in graphene, t_{cc} is the hopping. Left panel: without electric field, showing two gapless, spin degenerate edge states. Right panel: with finite critical electric field (red/black denoting up/down spin states), distorting the spectrum, and bringing additional levels into play around zero energy. Consequently, the spin-Hall conductivity is not quantized any more. Similar effects are generated by a strain induced pseudo-electric field having opposite sign in the two valleys, resulting in a valley-Hall effect. For stronger E, band crossing is more significant.

A static, uniform electric field can also be represented by a scalar potential as $V(\mathbf{r}) = eEx$. Therefore, we have decided to take a complementary look

at the stationary version of the same problem by analyzing Eq. (3.3) in a static, uniform electric field from a scalar potential and without the vector potential. Due to the time-independence of this setup, the eigenenergies can be determined from the stationary Schrödinger equation, and the evolution of the spectrum and edge states as a function of the electric field can be followed. We thus consider the tight-binding spectrum of a zigzag graphene ribbon[35] with intrinsic SOC, causing a gap with opposite sign between the two valleys, sublattices and spin directions in the continuum limit, similarly to Fig. 1.10. Without an electric field, only the edge states, connecting the two Dirac cones, carry the transverse current, in accord with Fig. 1.10, while in a strong electric field perpendicular to the edges, the effect of edge states is supplemented by the appearance of additional low energy modes living in two dimensions, due to the bands approaching and eventually touching each other, as seen in Fig. 3.5. As long as the electric field is smaller than a critical value, causing the band touching, the band structure remains qualitatively similar to that in Figs. 1.10 and 3.5 left panel: edge states are protected by a finite gap, above which a continuum of excitations exist. The spin-Hall response remains protected in this range. When the electric field exceeds its critical value, E_c, the gap closes (right panel in Fig. 3.5), and the edge states merge with the continuum, and are not protected any more: the spin-Hall breakdown occurs,

These results also allow to conjecture the nature of the quantum-Hall breakdown which occurs for graphene and related systems: 2D Dirac electrons in crossed stationary in plane electric (E) and perpendicular magnetic (B) field exhibit Landau quantization and subsequently quantized Hall conductivity. The value ($e^2/2h$ per spin and valley) and the origin of the lowest quantum Hall plateau agrees with that of Eq. (3.19), therefore its breakdown can also share common origin. Indeed, at $E = v_F B$, all Landau levels collapse[123, 124, 125] as visualized in Fig. 3.6 and a different Hall response should arise. Defining the energy gap as the distance between the Landau levels closest to the Dirac point, we have $\Delta_{Landau} = v_F\sqrt{2eB}$, yielding $E = \Delta^2_{Landau}/2ev_F$ for the field causing the collapse of Landau levels, which agrees well with the crossover field where the spin-Hall response changes dramatically. We expect that some of our results can be transcribed to the quantum Hall breakdown in graphene[116], testified by a Hall conductivity decreasing with the electric field, similarly to Eq. (3.20).

Finally, we return to the behaviour of the longitudinal response in the presence of a mass gap. The perturbative regime is characterized by exponentially activated behaviour due to the gap, and the current is exponentially

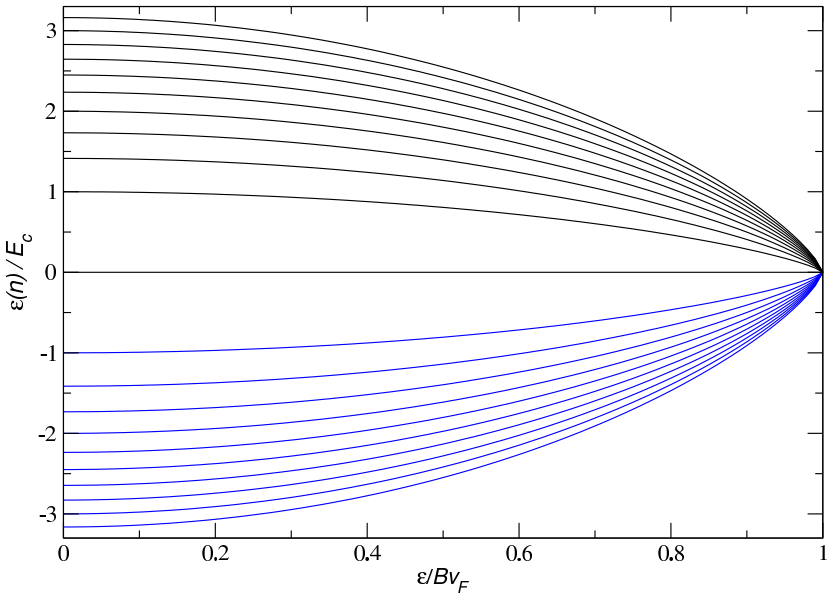

Figure 3.6: First ten Landau levels as function of $|\mathcal{E}|/v_F|B|$ from Ref [124]. The quantity E_c is the cyclotron energy $\tilde{\omega}_c$. The one dimensional momentum k, which is a good quantum number in the Landau gauge, was chosen to be zero.

suppressed at low temperatures ($T \ll \Delta$) as

$$j \sim E \exp(-2\Delta/k_B T),$$

just as in normal semiconductors. On the other hand, for strong electric field, we can still use the analogy to Landau Zener tunneling as

$$\langle j_x \rangle(t) = \frac{2e^2 E}{\pi^2} \sqrt{v_F e E t^2} \exp\left(-\frac{\pi \Delta^2}{v_F e E}\right). \tag{3.21}$$

Non-linear transport sets in for $E > \pi\Delta^2/v_F e$, which defines a new timescale for E_c as $\tau_\Delta = 1/\Delta\sqrt{\pi}$.

In general, the non-linear current for $d+1$ dimensional ($d = 1, 2, 3$) Dirac electrons[107] is

$$\langle j_x \rangle(t) \sim t E^{(d+1)/2} \exp\left(-\frac{\pi \Delta^2}{v_F e E}\right). \tag{3.22}$$

For $d = 1$, a good realization would be carbon nanotubes (rolled up graphene sheet), whose "non-linear" response is still linear ($j \sim E$), only the non-trivial exponential factor with a possible gap reports about non-perturbative effects[126]. The $d = 3$ case might be realized among the bulk electrons of Bi, possessing a band-gap ~ 0.015 eV.

In summary, we have studied the effect of longitudinal electric field on the non-linear longitudinal and Hall response of graphene and topological insulators[101, 102]. The current parallel to the electric field grows non-linearly with the field as $j \sim E^{3/2}$, which represents a clear deviation from Ohm's law and what was also found in subsequent experiments on graphene. The Hall current of a single, massive Dirac cone grows as $j_{Hall} \sim E^{1/2}$. Both responses witness electron-hole pair production and can be analyzed in terms of Schwinger's pair production.

Chapter 4

Quantum quench dynamics in bilayer graphene

The idea of using graphene as a possible source of coherent radiation has appeared in the literature short after its first isolation[127]. In this chapter, we show that BLG looks also very promising as the basic building block of a solid-state laser[128]. BLG features the unique property of altering its bandgap close to half filling by gate voltages, as discussed in the Introduction. Tuning the gap through zero in BLG in a time dependent perpendicular electric field parallels closely to a finite rate passage through a quantum critical point (QCP), and the resulting physics parallel to the Kibble-Zurek scaling[54, 55]. By manipulating the gap – in particular in real time – via a spatially uniform external electric field, which can therefore play the role of a (time dependent) control parameter, establishes BLG as an ideal setting for the study of quantum quenches[129, 130, 62]. The non-equilibrium state after the time-dependent process often possess an inverted population with high energy states occupied with a larger probability than their low energy partners. This could in principle provide a coherent source of infra-red radiation with tunable spectral properties (frequency and broadening). As there are only few materials that generate light in the infrared with tunable frequency, BLG with its unique properties might represent the first step towards new lasers for this regime.

4.1 Defect production in BLG

We start by analyzing a more general class of low energy Hamiltonians, comprising MLG from Eq. (1.3) and BLG from Eq. (1.13), exhibiting quantum

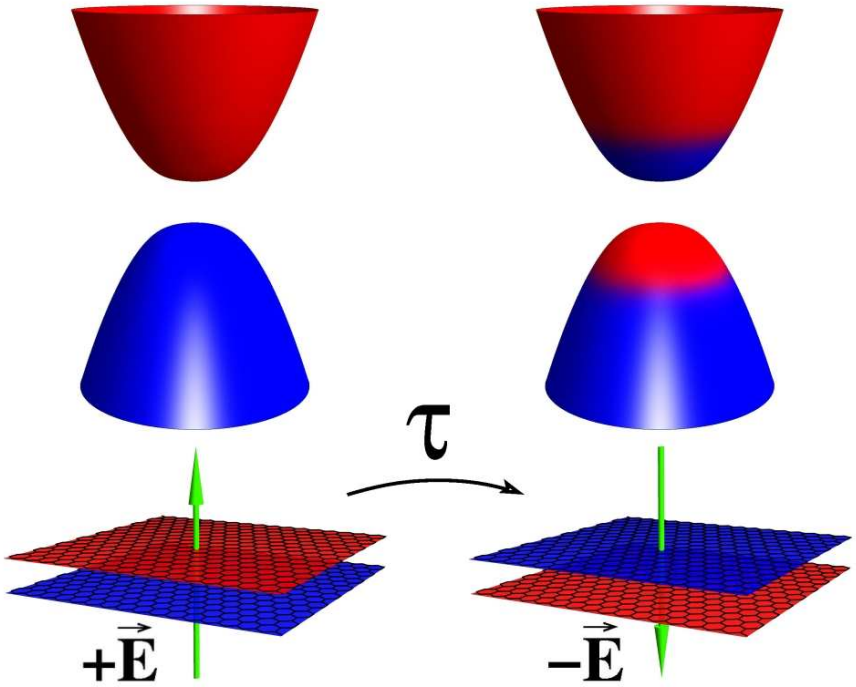

Figure 4.1: Reversing the applied perpendicular electric field $+\vec{E}$ in half-filled BLG (left) at a finite rate $1/\tau$ leads to excited states in the upper branch in accordance with the Kibble-Zurek theory of non-equilibrium phase transitions (right). The momentum distribution increases from red (0) to blue (1) in the spectra. Realistic quenching times provide an effective population inversion with little effect on the layer charge asymmetry.

critical behaviour, as

$$H = \begin{pmatrix} \Delta & c_J(p_x - ip_y)^J \\ c_J(p_x + ip_y)^J & -\Delta \end{pmatrix}, \tag{4.1}$$

where J is a positive integer. The energy spectrum is determined as $E_\pm(p) = \pm\sqrt{\Delta^2 + \varepsilon^2(p)}$, where $\varepsilon(p) = c_J|p|^J$ is the gapless spectrum, $|p| = \sqrt{p_x^2 + p_y^2}$ with spatial dimension $d = 2$.

The correlation length follows from dimensional analysis: $\xi \sim (c_J/|\Delta|)^{1/J}$, defining $\nu = 1/J$ as the correlation length exponent[131]. The Hamiltonian contains the Jth spatial derivative (Jth power of p), which leads to the dynamical critical exponent $z = J$. The resulting scaling relation $z\nu = 1$ is in agreement with a linearly vanishing gap Δ.

We will study the quantum quench dynamics when the gap varies as $\Delta(t) = \Delta_0 t/\tau$ (up to logarithmic corrections, as analyzed below) and $t \in$

$[-\tau, \tau]$. According to Kibble-Zurek scaling [54, 55] in Eq. (1.26), the resulting defect (extra electron/hole on the hole/electron rich layer, respectively, equivalent to excited states in the upper branch in this case[132], as shown in Fig. 4.1) density is

$$\rho \sim (\Delta_0/\tau)^{1/J} . \tag{4.2}$$

The matrix structure of Eq. (4.1) allows us again to connect our problem to the Landau-Zener (LZ) dynamics [110, 42, 43] in Eq. (1.23) by analyzing the solution of

$$i\partial_t \Psi(t) = H\Psi(t), \quad \Psi(-\tau) = \Psi_-, \tag{4.3}$$

where $H\Psi_\pm = E_\pm \Psi_\pm$, and the quantity of interest is $\Psi(\tau)$ and we focus on a zero temperature initial state. The diabatic transition probability between final ground and excited states at momentum p for $\varepsilon(p) \ll \Delta_0$ gives the momentum distribution of excited states in the upper branch (Fig. 4.1) and the resulting total defect density, which, using the Landau-Zener result from Eq. (1.24), yields

$$P_p = \exp\left(-\pi\varepsilon^2(p)\tau/\Delta_0\right), \tag{4.4}$$

$$\rho = \frac{A_c}{(2\pi)^2}\int \mathrm{d}^2 p P_p = \frac{A_c \Gamma(1/J)}{4J\pi}\left(\frac{\Delta_0}{\pi c_J^2 \tau}\right)^{1/J} \tag{4.5}$$

per valley, spin and unit cell, with A_c the unit cell area. The exponents agree with Kibble-Zurek scaling in Eq. (4.2). However, the present approach also provides the explicit numerical prefactor for arbitrary J, similarly to the quantum Ising model [52], when mapping to the Landau-Zener model is possible. While realizing the $J = 1$ quench seems unlikely in MLG, the $J = 2$ case with $c_2 = 1/2m$ is indeed realized by BLG. By using a dual-gate structure [19, 22, 20, 25, 21], a continuous change of the gate voltage results in closing and reopening the gap, as the density imbalance between the layers is inverted in BLG.

Upon changing the external potential as a function of time, we should in principle monitor the real time evolution and buildup of the screening on the layers. This would represent a significant challenge, which can be circumvented upon realizing that when the external potential changes adiabatically, the resulting gap and density imbalance are given by Eqs. (1.15) and (1.16), respectively. For slow, nearly adiabatic temporal changes of the potential, only a small fraction of terms in the δn sum is expected to behave truly diabatically (contribution from states nearest to the gap edges), while the rest follows an adiabatic time evolution. Therefore, for near-adiabatic quenches, when only the lowest energy states are affected, we can still use the adiabatic

expression for the induced gap to a good approximation. We have checked this numerically and verified, that the total number of excited states can be obtained using Eq. (1.15) at least semi-quantitatively [128].

The number of defects (excited states in the upper branch) created in an external potential, follows Eq. (4.5) even in the presence of screening as

$$\frac{\rho}{\rho_0 \Delta_0} = \frac{1}{2}\sqrt{\frac{\Delta_\lambda}{\Delta_0}}\sqrt{\frac{1}{\tau\Delta_0}}, \tag{4.6}$$

where $\Delta_0 = |U_0/2|$, $\Delta_\lambda \equiv \Delta|_{U_{ext}=U_0}$ from Eq. (1.15). In terms of numbers, since $\Delta_0\rho_0 \sim 10^{-3}$ for $\Delta_0 \sim t_\perp/10$, the resulting density of defects per unit area (including spin and valley) falls into the order of $\sqrt{1/\tau\Delta_0} \times 10^{12}$ cm^{-2}, and typically takes the value 3×10^9 cm^{-2} for quenching time $\tau \sim 1$ ns, corresponding to a ramping rate $\Delta_0/\tau \sim 10^7$ eV/s. Note that this density corresponds to the electrons/holes in the otherwise empty/occupied upper/lower branch, and does not by itself imply any particular real space density modulation, since these states contribute negligibly to the layer charge imbalance. A moderately slow quench implies $\tau\Delta_0/1 \sim 10 - 100$ with $\Delta_0 \sim t_\perp/10$, translating to $\tau \sim 0.1 - 1$ ps.

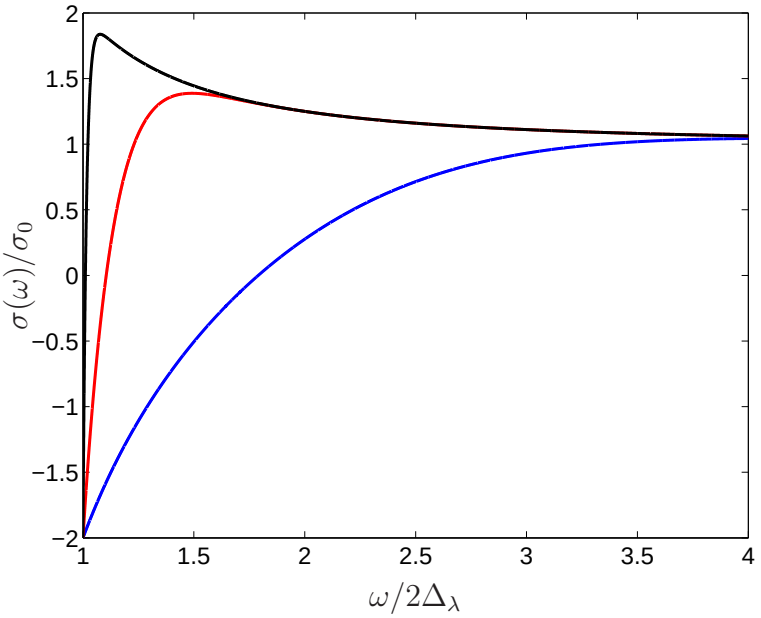

Figure 4.2: The dynamic conductivity of BLG is shown for $\tau\Delta_\lambda = 0.1$ (blue), 1 (red) and 10 (black) as a function of frequency.

4.2 Non-equilibrium optical response

Having evaluated of the defect density in BLG, created during the quench, we now focus on the optical response of the resulting non-equilibrium state, which is strongly affected by the momentum distribution given by Eq. (4.4), which differs significantly from a thermal distribution. Eq. (4.4) is population inverted, i. e. for any finite quench time, the occupation number of state at the upper gap edge is always larger than that below the lower gap edge. The optical response is evaluated by considering a small ac electric field within linear response, e.g. using Fermi's golden rule, and the dynamic conductivity after the quench is related to the rate of optical transitions between the two states with the same momentum, weighted by the probabilities of occupied initial and empty final states, yielding the dynamical conductivity

$$\frac{\sigma(\omega)}{\sigma_0} = \left[1 - 2\exp\left(\pi\tau\left(\Delta_\lambda - \frac{\omega^2}{4\Delta_\lambda}\right)\right)\right]\left[1 + \frac{4\Delta_\lambda^2}{\omega^2}\right]\Theta\left(|\omega| - 2\Delta_\lambda\right), \quad (4.7)$$

with $\sigma_0 = \pi e^2/h$ the ac conductivity of BLG [133, 134], twice that of MLG from Eq. (1.11) and is plotted in Fig 4.2. At high energies, the population inversion is lost and it approaches its universal, frequency independent value as seen in Fig. 1.6. However, close to the gap edge, the dynamic conductivity is negative due to the population inversion [127] (i.e. the energy injected into the system during the quench is released) as

$$\sigma(\omega \to 2\Delta_\lambda) \approx -2\sigma_0. \quad (4.8)$$

This indicates the dominance of stimulated emission and a phase coherent response, which is of course essential for a laser. In addition, stimulated emission can also win against spontaneous emission by increasing the intensity of the incoming radiation field. If spontaneous emission dominates (luminescence), the resulting radiation will still be spectrally limited but without phase coherence.

The typical lasing frequency is estimated to be in the close vicinity of Δ_λ (including the THz regime, wavelength of the order of 10 μm), conveniently tunable by perpendicular electric fields [22]. The relaxation times for intra- and interband processes in MLG are estimated as 1 ps and 1-100 ns[127], respectively, which might be further enhanced in BLG around half-filling[135]. Thus, the lasing is expected to survive for quenching times in the ps-ns range even in the presence of the above processes.

Our results apply to other systems with a quadratic band crossing, e.g. for certain nodal superconductors or cold atoms on Kagome or checkerboard optical lattices [136] at appropriate fillings, described by Eq. (4.1) with $J = 2$

at low energies. The momentum distribution, Eq. (4.4) and the concomitant scaling of the defect density after closing and reopening the gap would be direct evidence of the quench dynamics. Particularly intriguingly, graphene multilayers with appropriate stackings realize higher order ($J > 2$) band crossings [137, 138].

To conclude, by exploiting the tunability of the band gap in BLG by a perpendicular electric field, a finite rate temporal electric field quench leads to excited state production, whose distribution is analyzed in terms of Kibble-Zurek scaling and LZ dynamics for non-linear quenches[128]. The effect of the quench is manifested in population inversion, and BLG could be used as a coherent source of infra-red radiation, and possibly as a laser.

Chapter 5

Rabi oscillations in graphene

A graphene sheet in a perpendicular magnetic field hosts Landau levels as in Eq. (1.9), with an unusual dependence on the Landau level index n as $\sqrt{n}$, in accord with experimental observations[139, 140]. This is to be contrasted with the linear in n dependence of a two dimensional electron gas, obeying the Schrödinger equation. Not only the spectrum is different, but the wavefunction and consequently the overlaps and selection rules in a magnetic field differ considerably in graphene from that in a normal electron gas. By analyzing the non-equilibrium current dynamics of high-mobility graphene, we demonstrate that the current dynamics is controlled by oscillations between Landau levels[141], resembling closely to that in the Jaynes-Cummings or Rabi models[142].

5.1 The Jaynes-Cummings model

The presence of magnetic field can be taken into account by introducing a vector potential via the Peierls substitution as $\pi = \mathbf{p} + e\mathbf{A}$, where $\mathbf{p} = -i\nabla$, e is the electric charge and $\mathbf{A} = (0, Bx, 0)$ is the vector potential in Landau gauge, describing a perpendicular magnetic field to the graphene layer. The corresponding Hamiltonian of a graphene monolayer around the K point is given by[3]

$$H_g = \begin{pmatrix} \Delta & v_F\pi^- \\ v_F\pi^+ & -\Delta \end{pmatrix}, \tag{5.1}$$

where $v_F = 10^6$ m/s is the Fermi velocity in graphene, $\pi^\pm = \pi_x \pm i\pi_y$, Δ represents a sublattice imbalance, a possible excitonic gap[143] or substrate induced bandgap[144] in epitaxial graphene. Since $[\pi^-, \pi^+] = 2eB$ satisfies

bosonic commutation relations, we can introduce the creation and annihilation operators of a harmonic oscillator as $\pi^+ = \sqrt{2eB}a^+$ and $\pi^- = \sqrt{2eB}a$, leading to

$$H_g = v_F \begin{pmatrix} \Delta & v_F\sqrt{2eB}a \\ v_F\sqrt{2eB}a^+ & -\Delta \end{pmatrix}. \tag{5.2}$$

This model is connected to the basic model in quantum optics, describing the interaction of a two level atom or spin 1/2 in a cavity with a single mode electromagnetic field, known as the Jaynes-Cummings Hamiltonian[142]. Consider a two-state atom or spin 1/2 interacting with monochromatic quantized electromagnetic field, whose electric part is $E \sim a+a^+$, while the dipole transition between the two atomic states are described by $d \sim \sigma_x \sim \sigma^+ + \sigma^-$, leading to the interaction $H_{int} = -VdE$ with coupling constant V, sketched in Fig. 5.1. Then, the full Hamiltonian in the rotating wave approximation, neglecting $a^+\sigma^+$ and $a\sigma^-$ terms, is

$$H_{JC} = V(a^+\sigma^- + \sigma^+a) + \Delta\sigma_z + \omega a^+a = \begin{pmatrix} \Delta + \omega a^+a & Va \\ Va^+ & -\Delta + \omega a^+a \end{pmatrix}, \tag{5.3}$$

where Δ is the energy imbalance between the atomic states. The Jaynes-Cummings model features, among many others, Rabi oscillations, which are periodic exchange of energy between the electromagnetic field and the two-level system. It possesses $a^+a + \sigma_z/2$ as a conserved quantity, thus it is integrable. Note that the original version of the model without the rotating wave approximation was long thought to be non-integrable, and its exact solution has only been found recently[145].

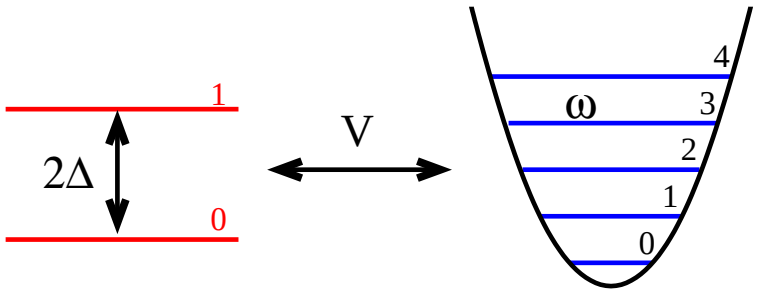

Figure 5.1: Cartoon about the basic ingredients of the Jaynes-Cummings model. The two level atom (red, left) is coupled via dipole transitions to the quantized electromagnetic field, denoted by the blue parabola.

With the $V = v_F\sqrt{2eB}$ (vacuum Rabi frequency) and $\omega = 0$ identification, the Jaynes-Cummings model coincides with the Dirac Hamiltonian

in a quantizing magnetic field. The electromagnetic field in the former case plays the role of the raising and lowering operators on the Landau basis, and the two-state atom or the spin 1/2 in the former is represented by the pseudospin index in the latter. Albeit the frequency of the electromagnetic field is zero, the excitation energies of the coupled system depend on the boson number. The fact that these two Hamiltonian are equivalent to each other is also related to Zitterbewegung[7, 146, 147], which is caused by the coupling between states with positive and negative energies (represented by the Pauli matrices). In the present case, the transition between these states is provided by the bosonic field a.

The eigenvalues of the Hamiltonian are

$$E_{n\alpha} = \alpha\sqrt{\Delta^2 + V^2(n+1)}, \tag{5.4}$$

where $n = 0, 1, 2\ldots$ non-negative integer, $\alpha = \pm$. In the non-relativistic limit ($\Delta \gg V$), the usual Landau level spectrum is obtained as $\alpha(\Delta + \omega_c(n+1))$ with cyclotron frequency $\omega_c = v_F^2 eB/\Delta$. In addition, there is a special eigenstate, stemming from the Landau level at the Dirac point with

$$E^* = -\Delta \tag{5.5}$$

which formally corresponds to $n = -1$ and $\alpha = -1$.

5.2 Real-time current-current correlations

We now turn to the investigation of the σ_x correlation function, $C_{xx}(t) = \langle\sigma_x(t)\sigma_x(0)\rangle$. In the case of the Jaynes-Cummings model, it describes the transitions between the two atomic states, and tells us about the spectrum of Rabi oscillations[148]. In the case of graphene, σ_x coincides with the current operator. This can easily be checked by evaluating the current as the time derivative of the polarization operator in the Heisenberg picture as $j_x = i[H, x] = v_F\sigma_x$, and similarly $j_y = v_F\sigma_y$, which holds in the presence of the magnetic field as well. Therefore, $C_{xx}(t)$ plays the role of the current-current correlation function in the Dirac case, and leads eventually to the optical conductivity[14, 149]. Therefore, we expect the well-known Rabi oscillations of quantum optics characterizing the excitations of the atom to be observable in the various response functions of Landau quantized Dirac fermions. The

correlation function is evaluated, following standard manipulation, as

$$C_{xx}(t) = g_c f(E^*) \sum_{\gamma=\pm} \exp(i(E_{0\gamma} + E^*)t) P_{*\to 0\gamma} + \\ + \sum_{\substack{n\geqslant 0,\\ \alpha\gamma s=\pm}} g_c f(E_{n\alpha}) \exp(i(E_{n\alpha} + E_{n-s\gamma})t) P_{n\alpha\to n-s\gamma}, \tag{5.6}$$

where $f(E) = 1/(\exp((E-\mu)/T)+1)$ is the Fermi function, $g_c = N_f A_c eB/2\pi$ is the degeneracy of the Landau levels and spins, A_c is the area of the unit cell, to be taken as unity in the Dirac approach, $N_f = 2$ stands for the spin degeneracy. The structure of the optical transitions can be readily identified from this: a $E_{n\alpha}$ Landau level with $n > 0$ and given α possesses 4 possible optical transitions to the adjacent levels as $E_{n\pm 1\pm\alpha}$ (on the same side and on the other side of the Dirac cone), the $n = 0$ level 3 transitions to $E_{1\pm\alpha}$ and E^* and the E^* level two transitions to $E_{0\pm}$. The non-zero transition matrix elements are given by

$$P_{n\alpha\to n-s\gamma} = \frac{1}{4}\left(1 + \frac{s\Delta}{E_{n\alpha}}\right)\left(1 + \frac{s\Delta}{E_{n-s\gamma}}\right) \text{ for } n \geqslant 0, \\ P_{*\to 0\gamma} = \frac{1}{2}\left(1 - \frac{\Delta}{E_{0\gamma}}\right), \tag{5.7}$$

which satisfy $\sum_{m\gamma} P_{n\alpha\to m\gamma} = 1$, and agree with the transition probabilities for Rabi oscillations of atoms induced by external electromagnetic field. These approach 1/4 in the classical limit (of bosons) $n \to \infty$, in which case the field contains many bosons, whose quantum character can then be neglected[150]. Interestingly, the $\Delta = 0$ limit yields the classical matrix elements for any $n \geqslant 0$. However, the E^* level never reaches the classical limit, and is responsible for the anomalous optical properties of graphene in magnetic field[151], see e.g. the discussion below Eq. (1.9). Therefore, all selection rules and transition probabilities are identical in the two models.

Rabi oscillations occur when the atom repeatedly emits and reabsorbs radiation. These are also possible in the vacuum of the radiation field, when the atom is prepared in its excited state, referred to as vacuum-field Rabi oscillations, which are not captured by the classical treatment of the field. Therefore, the transition probabilities involving the E^* level differ from the other matrix elements due to their quantum mechanical origin.

From the current-current correlation function, the optical conductivity follows, which agrees with those obtained for graphene with distinct methods[152, 153, 103, 154]. The allowed optical transitions are thus controlled by Eq. (5.7),

which, together with the relation to the Jaynes-Cummings Hamiltonian provides us with a particularly simple picture about the optical selection rules and transitions by relating them to the Rabi oscillations. Therefore, the optical conductivity by varying the frequency sweeps through all possible transitions, and measures the frequency of the Rabi oscillations, with quantum or classical character. This provides a unique opportunity to investigate a basic phenomenon of quantum electrodynamics in a condensed matter experiment. By changing the external magnetic field applied to graphene, the coupling between the atom and electromagnetic field in the Jaynes-Cummings model can be tuned continuously, facilitating the exploration of various regimes, the quantum to classical crossover.

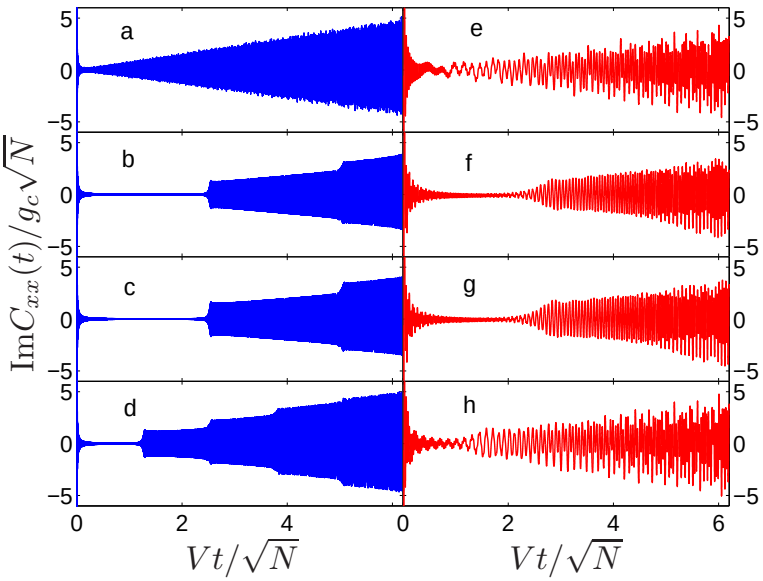

Figure 5.2: The real time evolution of $C_{xx}(t)$ is shown at $T = 0$, taking both valley and spin degeneracies into account. We introduced a cutoff D, and the number of levels is measured as $D = V\sqrt{N}$, corresponding to different magnetic field strengths. The left/right panels show $N = 10000$ (blue)/$N = 100$ (red) with $D = V\sqrt{N}$ for $(\mu, \Delta)/V\sqrt{N} = (0, 0)$ [a/e], (0.4,0) [b/f], (0.4,0.2) [c/g], and (0,0.2) [d/h]. These structures correspond to thermal field induced random oscillation in quantum optics[155].

In quantum optics, one can prepare the initial state of both the atom and the electromagnetic field freely. The atom is usually in its excited state, and the field is prepared in a number state or in a coherent state. Then, through the Jaynes-Cummings Hamiltonian, the time evolution of the atomic population can be studied, which exhibits Rabi oscillations, when jumping between

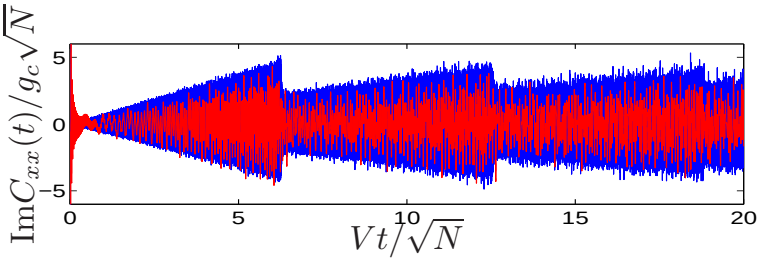

Figure 5.3: The real time evolution of $C_{xx}(t)$ is shown for long times for $T = 0$, $(\mu, \Delta) = (0, 0)$. We introduced a cutoff D, and the number of levels is measured as $D = V\sqrt{N}$, corresponding to different magnetic field strengths with $N = 10000$ (blue) and $N = 100$ (red). Collapse and revival shows up with time similarly to the thermal field Jaynes-Cummings model. The revivals gradually get wider and overlap. The presence of thermal revivals are related to the finite average boson number in the Jaynes-Cummings model, which translate to a finite cutoff in the Dirac case. As opposed to Fig. 5.2, these revivals at long times are caused by the finite cutoff.

the ground and excited state, causing collapse and revival phenomenon. However, qualitatively different behaviour describes chaotic or thermal fields[155], which are characterized by an average boson number. Quiescent periods and interfering revivals are also present, but the resulting pattern of oscillations follow an apparently random evolution, as shown in Fig. 5.4.

On the other hand, graphene, as a condensed matter system, does not allow for an arbitrary preparation of the initial states, but requires thermal, ensemble averaging. In this respect, it is closer to the second type of thermal initial condition for the Jaynes-Cummings model. The average boson number, characterizing the latter corresponds to the total number of fermions in the latter, determined by the chemical potential and the cutoff. This can be introduced by the energy scale $D = V\sqrt{N+1}$, above which we neglect all states (with $n > N$). We mention, that the inclusion of a cutoff is required to obtain correctly the f-sum rule for graphene[156].

The real time evolution of the longitudinal current-current correlation function based on Eq. (5.6) is shown in Fig. 5.2. Similarly to the Jaynes-Cummings model[155, 142], the initial collapse is followed by a revival of oscillation, which are also sensitive to the presence of finite μ and Δ. They both enlarge the quiescent period after the short time collapse, and cause additional step-like structures in the envelope of oscillations. For longer times, collapse and revival is observable in Fig. 5.3, which gradually become wider and overlap. This revival time depends on the value of the cutoff like $2\pi\sqrt{N+1}/V = \pi D/v_F^2 eB$, as is apparent from the figure, and is controllable

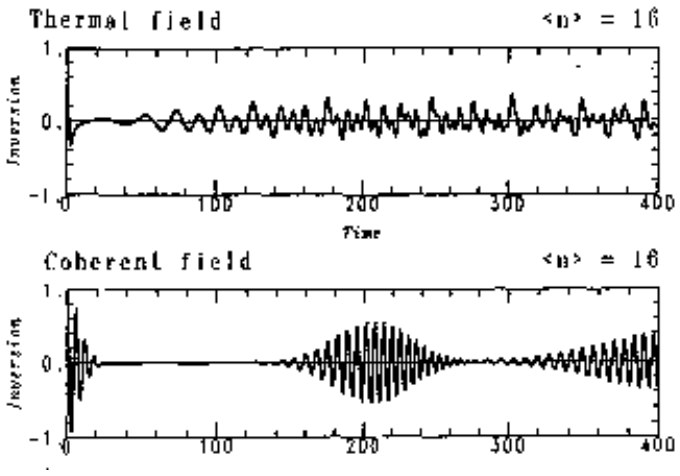

Figure 5.4: Population inversion of the Jaynes Cummings model, i.e. the difference between the expectation values of finding the atom in the excited and ground state from Ref. [142]. The initial mean photon number is 16. Top frame shows thermal field, lower frames show a coherent field. Times are in units of the inverse of the mean Rabi frequency.

by the magnetic field.

The evaluation of the microwave Hall conductivity proceeds through similar steps[141] from $C_{xy} = \langle \sigma_x(t)\sigma_y(0)\rangle$. The transverse current correlator is evaluated as

$$C_{xy}(t) = -ig_c f(E^*) \sum_{\gamma=\pm} \exp(i(E_{0\gamma} + E^*)t) P_{*\to 0\gamma} + \\ + \sum_{\substack{n\geqslant 0,\\ \alpha\gamma s=\pm}} ig_c f(E_{n\alpha}) \exp(i(E_{n\alpha} + E_{n-s\gamma})t) s P_{n\alpha\to n-s\gamma}, \tag{5.8}$$

producing the unconventional Hall steps in graphene as a function of μ or particle density. After Fourier transformation, it gives Eq. (1.10) at zero temperature.

The time evolution of the Hall correlator is shown in Fig. 5.5, and turns out to be independent of the applied cutoff scheme, hence universal. It exhibits Rabi oscillations in the original meaning of the word, which vanish at the Dirac point (this equivalent to the statement, that the Hall conductivity is zero exactly at the Dirac point). Upon increasing μ, oscillations appear, showing beating property, observed in the Jaynes-Cummings model as well[142]. The period of the envelope functions widens with μ, bringing

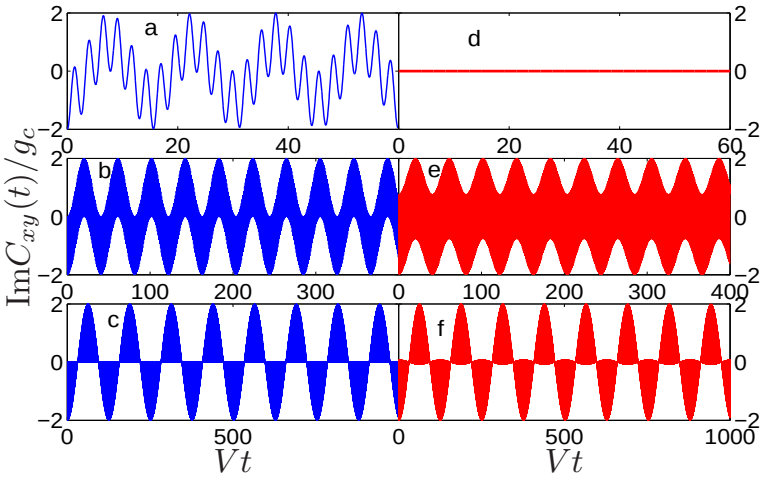

Figure 5.5: The real time evolution of $C_{xy}(t)$ is shown for $T = 0$. The explicit value of the number of levels (N) does not influence the resulting pattern. The chemical potential varied as $\mu/V = 1.2$ [a/d], 3.2 [b/e] and 10 [c/f] with $\Delta = 0$ (left panel, blue) and $\Delta = 2V$ (right panel, red), and the frequency of the envelope function is $v_F^2 eB/\mu$, the cyclotron frequency of massless Dirac fermions. For $T = 0$ and $\Delta > \mu$, $\mathrm{Im}C_{xy}(t) = 0$. Note the different horizontal scales!

the relevant timescale to the experimentally measurable domain. The typical timescale for the evolution of the correlation functions is set by $T_B = \hbar/V$ upon reinserting original units, which translates into $T_B = \sqrt{\hbar/2eB}/v_F$, of the order of 10 femtosecond for a field of 1 T. This is usually enlarged by the presence of the cutoff for $C_{xx}(T)$ and by the chemical potential for $C_{xy}(t)$. A possible time limit is provided by impurities, which broaden the Landau levels, whose effect is taken into account by an additional $\exp(-\Gamma t)$ factor. Therefore, the available time window is restricted to times$< 1/\Gamma$.

A possible way to measure these correlation functions is provided through optical conductivity or current fluctuation measurement. Via the fluctuation dissipation theorem, they contain the same information, and upon Fourier transforming from frequency space to get the real time dependence, one is expected to be able to observe the presence of thermal Rabi oscillations. Similar measurements have already been carried out without magnetic field[14, 149], by exploiting the tunability of the carrier concentration with gate voltage.

In conclusion, we have shown that the equivalence of the Hamiltonians of graphene in magnetic field and of the JC model influences their correlation functions as well, causing both thermal and coherent Rabi oscillation in the electric response of graphene[141]. Finally we speculate that Rabi oscillations

and Zitterbewegung are two closely related phenomena named differently in different fields of physics, both arising from the coupling of positive and negative energy states.

Chapter 6

Floquet topological insulators

Topological insulators are interesting not only for basic research but also due to their possible application in spintronics and quantum computation. However, topologically non-trivial materials are rather scarce, therefore various methods to turn a topologically trivial material to a TI should be warmly welcome. It is interesting to contemplate different physical mechanisms that could lead to non-trivial topological properties. Several strategies other than band structure engineering from the material science do exist. Applying strain to alter the band structure seems feasible for a variety of materials[157]. Electron-electron interactions can sometimes also produce the desired effect. Simple mean-field decoupling of the interaction can mimic an effective spin-orbit coupling, for example, thus inducing a transition from a topologically trivial to a non-trivial phase [158, 159, 160, 161].

6.1 Time-periodic perturbation

Bloch states and energy bands arise from spatially periodic Hamiltonians in condensed matter systems. Extending the periodicity in the time domain through a time-periodic perturbation increases tunability of the Hamiltonian: the temporal analogue of Bloch states (the Floquet states) can be manipulated via the periodicity and amplitude of the external perturbation[162, 163]. Bloch's theorem states that the electron wavefunction in a spatially periodic potential with $V(\mathbf{r}) = V(\mathbf{r} + \mathbf{R})$ is written as

$$\Psi_{\mathbf{k}}(\mathbf{r}) = \exp(i\mathbf{kr})u_{\mathbf{k}}(\mathbf{r}), \tag{6.1}$$

where $u_{\mathbf{k}}(\mathbf{r}) = u_{\mathbf{k}}(\mathbf{r} + \mathbf{R}) =$ is lattice periodic. Similarly, in the presence of a time periodic perturbation with $H(t) = H(t + T)$, Floquet's theorem

dictates[164, 165] the wavefunction to take the form

$$\Psi_\varepsilon(t) = \exp(-i\varepsilon t)\Phi_\varepsilon(t), \tag{6.2}$$

where $\Phi_\varepsilon(t) = \Phi_\varepsilon(t+T)$ is time periodic and ε is called the Floquet quasienergy. This is only well defined modulo $\omega = 2\pi/T$ in the Floquet Brillouin zone, since using the substitutions $\varepsilon_n = \varepsilon + n\omega$, $\Phi_{\varepsilon_n}(t) = \Phi_\varepsilon(t)\exp(in\omega)$ give identical wavefunctions, which is Bloch's theorem in the time domain.

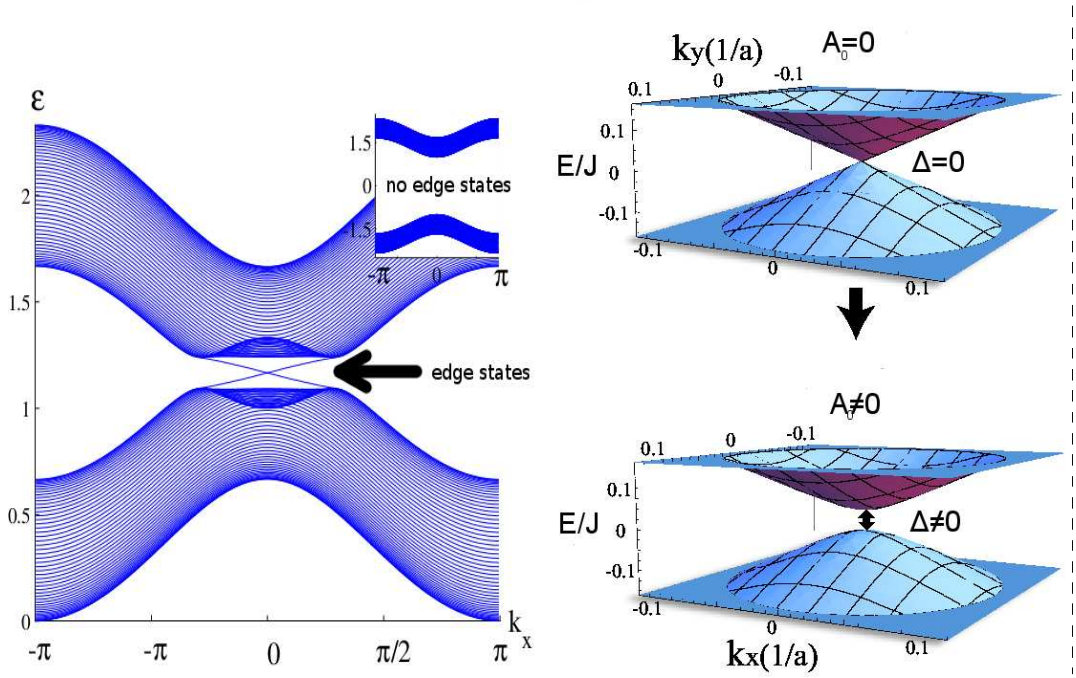

Figure 6.1: Left: The energy spectrum of a non-inverted HgTe/CdTe quantum well (inset) and the Floquet quasienergies in the presence of a linearly polarized perturbation (main panel) with 2 chiral edge modes, traversing the gap. Pictures taken from Ref. [166]. Right: The energy spectrum of Dirac electrons near one of the Dirac points is shown for without light ($A_0 = 0$, upper figure) and the Floquet quasienergies under the application of light with $A_0 \neq 0$ (lower figure), opening a finite gap at the Dirac point. J_0 is the hopping amplitude and a the lattice constant of the graphene honeycomb lattice. Picture taken from Ref. [167].

Recently, it has been shown that novel topological edge states can be induced by shining electromagnetic radiation on a topologically trivial insulator, e.g. a non inverted HgTe/CdTe quantum well with no edge state in the static limit [166]. A linearly polarized light was capable of inverting

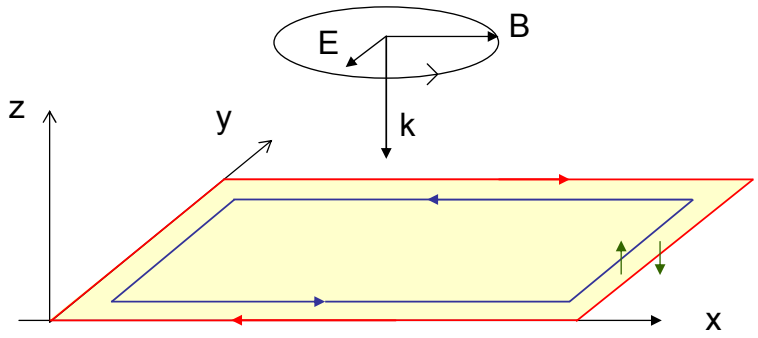

Figure 6.2: The quantum spin-Hall insulator (light yellow rectangle) with its helical edge state (counterpropagating red/blue arrows) in a circularly polarized electromagnetic field with frequency ω and wave vector k. In the plane $z = 0$ the rotating vector potential $\mathbf{A}(t) = A_0(-\sin\omega t, \cos\omega t)$ is perpendicular to the S^z direction (vertical green arrows). Picture taken from Ref. [162].

the band-structure, yielding topologically protected edge states, as shown in Fig. 6.1. It has been predicted that circularly polarized light can open a gap at the Dirac points[168]. Moreover, it was argued[167] that for small laser power, the effective Hamiltonian contains an effective spin-orbit coupling term, being identical to the intrinsic spin-orbit coupling in graphene (Eq. (1.19)). As a result, a topologically protected, light induced gapless edge mode appears, similarly to that in a quantum spin-Hall insulator[35]. The gap at the Dirac point can be estimated as

$$\Delta = 16\pi\alpha\frac{v_F^2 I}{\omega^3}\sin\phi, \tag{6.3}$$

where I is the laser intensity (W/m^2), $\alpha \simeq 1/137$ is the fine structure constant and ϕ tunes the polarization, i.e. circular or linear polarization implies $\phi = \pm\pi/2$ or $0, \pi$, respectively.

We have decided to investigate the fate of a quantum spin-Hall edge state in the presence of circularly polarized electromagnetic field[162, 163]. A quantum spin-Hall insulator, located in the xy plane, is irradiated by a circularly polarized electromagnetic field with frequency ω (Fig. 6.2). The general Hamiltonian of the QSH edge from Eq. (1.20) reads in this setting:

$$H(t) = v_F\sigma^z(p - eA_x(t)) + g\left[\sigma^+\exp(-i\omega t) + h.c.\right], \tag{6.4}$$

where the Pauli matrix σ_z represents the physical spin of the electron, p the momentum along the one-dimensional channel and v_F the Fermi velocity. It is

assumed that the quantization axis of the QSH edge state is perpendicular to the plane xy. The circularly polarized radiation now acts on both the orbital motion through the vector potential $A_x(t) = -A_0 \sin \omega t$ and on the electron spin through the Zeeman coupling $g = g_{\text{eff}} \mu_B B_0$, g_{eff} being the effective g-factor and μ_B the Bohr magneton. The orbital effect can be safely neglected according to a simple semi-classical argument: an electron travelling at speed v_F in an electric field $E_0 = A_0 \omega = cB_0$ during a time $1/\omega$ picks up an energy $v_F e E_0/\omega$ from the vector potential which has to be compared to the smallest energy quantum it can absorb, $\hbar\omega$. Hence in the regime $v_F e E_0/\omega \ll \hbar\omega$, only the time-dependent Zeeman effect is effective and not the orbital effect. In contrast to this, in other 2D systems the orbital effect is the dominant one [168, 169, 170, 171, 172].

Eq. (6.4) without the vector potential is exactly solvable[162], since for a given p, it maps onto the Hamiltonian of a two level system in circularly polarized electromagnetic field[164, 165], which is the classical version of the Jaynes-Cummings Hamiltonian[142] in Eq. (5.2) using the correspondence $a \longleftrightarrow \exp(-i\omega t)$. It is to time periodic problems what the Landau-Zener model is to (avoided) level crossings.

6.2 Topological properties and photocurrent

We now analyse the topological invariant describing the steady state of the QSH edge state in terms of the mapping, $(p,t) \to \hat{\mathbf{d}}_{\alpha,p}(t) = \Phi^+_\alpha(p,t)\mathbf{S}\Phi_\alpha(p,t) = \alpha(g\cos(\omega t), g\sin(\omega t), v_F p - \omega/2)/\lambda$, between the 1+1 dimensional (p,t) space and the unit sphere. Here, $\alpha = \pm 1$ distinguishes between the Floquet bands, which are descendant of the Dirac bands without the field, $\lambda = \sqrt{g^2 + (v_F p - \omega/2)^2}$ and $\Phi_\alpha(p,t)$ is the Floquet wavefunction[162]. The sub-band Chern number,

$$\mathcal{C}_\alpha = \int_{-\infty}^{\infty} \frac{dp}{4\pi} \int_0^T dt \hat{\mathbf{d}}_{\alpha,p}(t) \cdot \left(\frac{\partial \hat{\mathbf{d}}_{\alpha,p}(t)}{\partial p} \times \frac{\partial \hat{\mathbf{d}}_{\alpha,p}(t)}{\partial t} \right), \tag{6.5}$$

counts the number of times the unit vector $\hat{\mathbf{d}}_{\alpha,p}(t)$ wraps around the unit sphere [33, 166, 34], the summation being taken over occupied bands. In principle the integral goes over a compact manifold like the Brillouin zone. However, it is enough to calculate the integral of the Berry curvature for an individual Dirac cone, living on the infinite plane of momenta to get the topological invariant, since high energy states usually do not contribute much to topological invariants, see e.g. Ref. [35]. Due the the circularly polarized

field, a finite photocurrent is generated along the edge by the Zeeman term as

$$\langle j \rangle = \frac{e}{2\pi} |\omega| \mathcal{C}_-, \tag{6.6}$$

which is the incarnation of the magnetoelectric effect, namely that an electric current is generated by coupling to magnetic fields.

The behavior of this topological invariant (and photocurrent) can be investigated as a function of the frequency of the driving field. At low frequency, $|\omega| < 4g$, and half filling, the $\alpha = -1$ band is occupied. Indeed we have checked numerically that such an initial state below the Fermi level (before irradiation) will evolve to one of the negative energy Floquet states upon smoothly branching the time-dependent driving field. Then accordingly the Chern number

$$\mathcal{C}_\alpha = -\int_{-\infty}^{\infty} dp \frac{\alpha \mathrm{sign}(\omega) v_F g^2}{2\lambda^3} = -\alpha \mathrm{sign}(\omega) \tag{6.7}$$

is quantized, shown in Fig. 6.3. By contrast, when $|\omega| > 4g$, the two bands cross, and $\mathcal{C}_-$ is no longer quantized, in analogy to the transfer of Chern numbers between equilibrium bands which touch:

$$\mathcal{C}_\alpha = -\alpha \mathrm{sign}(\omega) \left(1 - \sum_{s=\pm 1} s \frac{\sqrt{2\omega_s \omega}}{\omega} \right) \tag{6.8}$$

where $4\omega_\pm = \omega \pm \sqrt{\omega^2 - 16g^2}$. The Chern number $\mathcal{C}_\alpha$ vanishes as $\mathcal{C}_\alpha = -\alpha 2g/\omega$ for $g \ll |\omega|$. The quantized photocurrent is lost due to the crossing of Floquet subbands carrying opposite Chern number. It is remarkable that the Chern number and the photocurrent are quantized over a broad range of frequencies, $|\omega| < 4g$, that exceeds the strict adiabatic limit. In this limit, it can be deduced [173] from the Goldstone-Wilczek formula [174]. The robustness of the quantization for $|\omega| < 4g$ is a feature specific to our model. It is related to the fact that the gap of the instantaneous Hamiltonian $H(t)$ never closes for Zeeman coupling and circular polarization. In particular this quantization still survives for elliptic polarization, upon addition of an inversion symmetry breaking term and/or in presence of orbital effects[162].

The typical induced photocurrent is estimated by recalling that the $g \ll |\omega|$ regime is realized usually (and note that larger values of ω are beneficial for neglecting the vector potential), and for a radiation field with magnetic field strength of the order of $10^{-4} - 10^{-5}$ T, this generates a photocurrent of the order of $0.1 - 10$ pA, depending also on the effective g-factor values.

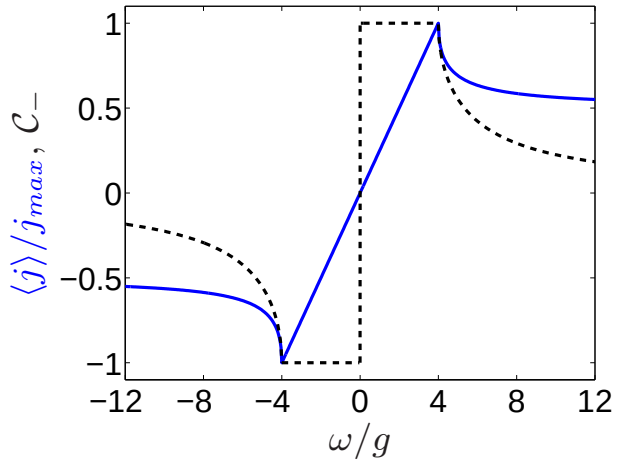

Figure 6.3: The induced photocurrent (blue solid line) and the $\mathcal{C}_-$ Chern number (black dashed line) are shown as a function of ω/g. The latter becomes non-quantized when band touching occurs at $4g = |\omega|$.

These can be significantly enhanced ($g_{\text{eff}} \approx 20 - 50$) for certain materials such as HgTe/CdTe, HgSe or Bi_2Se_3.

The induced current can be detected in a contactless measurement. The photoinduced "rectified current" being of the order $\langle j\rangle = 1$ pA, the corresponding magnetic field $B_{ind} = 1$ pT (for a 1 micron perimeter) is within the detectability limit of an ac SQUID [162].

The topological properties of the edge state are reflected in the induced magnetization and photocurrent, shown in Fig. 6.3. In the $|\omega| < 4g$ regime, the current is obtained (upon restoring original units) as $\langle j\rangle = \text{sign}(\omega)e/T$, which tells us that the charge pumped within one cycle (T) is exactly the unit charge. The integer charge pumped across a 1D insulator in one period of an (adiabatic) cycle is a topological invariant that characterizes the cycle. This specific quantization of charge stems directly from the quantized $\mathcal{C}_- = \text{sign}(\omega)$ in this regime, as was identified by Thouless [175]. The current is dissipationless, protected by a photoinduced gap. Though the current still satisfies $\langle j\rangle = e\mathcal{C}_-/T$ for $|\omega| > 4g$, it is dissipative and no longer quantized due to the band touching, in analogy with the photovoltaic Hall effect [168] in graphene.

We have demonstrated that the topological properties of a spin-Hall edge state can be altered by irradiating it with a circularly polarized light[162, 163]. Upon increasing its frequency, a topological transition takes place from dissipationless charge pumping to a dissipative transport regime. Our predictions could be tested by experiments similar to those in graphene [176]

and HgTe/CdTe quantum wells [177], they rely on a different coupling mechanism, that is Zeeman coupling rather than orbital coupling.

Chapter 7

Interaction quench in a Luttinger liquid

As we have seen in the Introduction, the LL physics is rather peculiar as signalled by the non-integer power law-exponents. Such low dimensional systems can be driven out of equilibrium through e.g. transport [178, 179], but here we focus on time dependent changes of the interaction parameter, which is of particular relevance for cold atomic systems. Sudden quenches (SQ) of the interaction in LLs have been considered recently by several authors [180, 181, 182], and the properties of the other extreme limit of adiabatic parameter ramps has long been investigated. However, experimental ramps cannot take infinite time, and are not instantaneous, either. Here we study, how a nonzero quench time, $\tau \neq 0$, influences the final state of the system after a quantum quench. As we present here, based on Refs. [183, 184, 185, 186], a finite τ leads to 'heating' effects, and generates excitations in the final state. Moreover, it leads to in the appearance of additional energy ($\sim 1/\tau$) and corresponding length scales: while in certain space-time regions the system reveals universal near-equilibrium (adiabatic) correlations [66], in other regimes renormalized Fermi liquid (FL) or sudden quench (SQ) behavior is found.

Thus motivated, we study the time dependent version of Eq. (1.42) as

$$H = \sum_{q\neq 0} \omega(q) b_q^\dagger b_q + \frac{g(q,t)}{2}[b_q b_{-q} + b_q^+ b_{-q}^+], \tag{7.1}$$

with $\omega(q) = v|q|$ (v being the bare "sound velocity"). The interaction g is changed from zero to a nonzero value within a quench time τ, $g(q,t) = g_2(q)|q|Q(t)$, with $Q(t)$ encoding the explicit quench protocol, and satisfying $Q(t > \tau) = 1$ and $Q(t < 0) = 0$. In particular, for a linear quench, $Q(t) = t\Theta(t(\tau - t))/\tau + \Theta(t - \tau)$ with $\Theta(t)$ the Heaviside functions.

To understand the applicability of the low energy LL description for quenches, one needs to go beyond the LL paradigm by either considering additional terms in the Hamiltonian (termed irrelevant in equilibrium) or by comparing the results of the LL theory to numerical simulations on lattice models. We have decided to follow the second option, and investigated arbitrary rate quenches numerically on the J_z component of the XXZ Heisenberg model, i.e. by allowing for a $J_z Q(t)$ function in Eq. (1.48). Then, these are compared to bosonization results. Similar approach was undertaken in Ref. [187] for the case of a sudden interaction quench.

All the numerical simulations, presented in this chapter, were performed by Frank Pollmann using a combination of a matrix-product state (MPS) [188] based infinite density matrix renormalization (iDMRG) [189, 190, 191] and the infinite time evolving block decimation (iTEBD) [192] algorithms [193, 184]. In the implementation of the two algorithms, infinite, translationally invariant systems are used. Working in the limit of infinite systems has the advantage that no finite size effects show up and the only approximation is the finite bond dimension (χ) of the MPS. In critical systems (as the one we are studying), the finiteness of χ induces a finite correlation length $\xi \propto \chi^{\kappa}$ with κ being a model specific parameter [194, 195]. For our simulations, we check and ensure that the induced correlation length does not affect our results. First the iDMRG method is used to find the ground state by optimizing variationally a wavefunction in the MPS representation. Then the actual quench is simulated using the iTEBD technique. This technique is based on a Suzuki-Trotter decomposition of the time-evolution operator and provides an efficient algorithm to perform the real-time evolution of the MPS during the quench. A time-step of $\delta t = 0.01 J^{-1}$ together with a second-order Trotter decomposition are used.

The time evolution in Eq. (7.1) is attacked by the Heisenberg equation of motion, leading to

$$i\partial_t b_q = [b_q, H] = \omega(q)\; b_q + g(q,t)\; b^+_{-q}, \tag{7.2}$$

and similarly to $\partial_t b^+_{-q}$. These are solved by a time-dependent Bogoliubov coefficients as

$$b_q(t) = u(q,t)\; b_q(0) + v^*(q,t)\; b^+_{-q}(0)\;, \tag{7.3}$$

where all the time dependence is carried by the prefactors, $u(q,t)$ and $v(q,t)$, and the operators on the r.h.s. refer to non-interacting bosons before the quench. All expectation values are taken in terms of the initial density matrix of the latter. The bosonic nature of the quasiparticles requires $|u(q,t)|^2 -$

$|v(q,t)|^2 = 1$. From Eqs. (7.2)-(7.3), we obtain

$$i\partial_t \begin{bmatrix} u(q,t) \\ v(q,t) \end{bmatrix} = \begin{bmatrix} \omega(q) & g(q,t) \\ -g(q,t) & -\omega(q) \end{bmatrix} \begin{bmatrix} u(q,t) \\ v(q,t) \end{bmatrix}, \tag{7.4}$$

with the initial condition $u(q,0) = 1$, $v(q,0) = 0$. By Eq. (7.4), all time dependence has been transferred to the Bogoliubov coefficients, and therefore expectation values of the time dependent bosonic modes and non-equilibrium dynamics are calculable using standard techniques developed for equilibrium [71], once the solutions of Eq. (7.4) are known.

From Eq. (7.4), the adiabatic limit follows from replacing $g(q,t)$ with its time independent final value, and looking for the stationary solutions of Eq. (7.4) at a given energy while ignoring the initial conditions. The SQ limit requires only the replacement of $g(q,t)$ by its final, time independent value, and solving the resulting linear differential equation with the initial conditions satisfied.

For a linear quench, Eq. (7.4) realizes the non-hermitian Landau-Zener model [196], which can be solved exactly in terms of the parabolic cylinder function. However, the exact solution does not yield an immediate and transparent physical picture, similarly to the hermitian Landau-Zener model in Eq. (1.23). To obtain more insight, we assume that $g(q,t) \ll \omega(q)$ (i.e., $g_2(q) \ll v$) for all t and q, and solve Eq. (7.4) perturbatively in the interaction. To lowest order in $g_2(q)$, we obtain $u(q,t) \approx \exp(-i\omega(q)t)$ and

$$v(q, t > 0) \approx i \int_0^t dt' g(q,t') \exp(i\omega(q)(t - 2t')) \, . \tag{7.5}$$

We have also checked numerically that Eq. (7.5) is indeed applicable for any t and τ, as long as $g_2(q) \ll v$, and the the solution can easily be extended to include higher powers of $g_2(q)$ for a linear quench. In the SQ ($\tau \to 0$) and adiabatic ($\tau \to \infty$) limits we obtain

$$v(q, t > \tau) \approx \frac{g_2(q)}{2v} \times \begin{cases} 2i \sin(\omega(q)t) & \text{for } \tau \to 0, \\ -\exp(-i\omega(q)t) & \text{for } \tau \to \infty, \end{cases} \tag{7.6}$$

reproducing to lowest order in $g_2(q)$ the SQ results [180, 182] and the equilibrium Bogoliubov transformation [77, 71], respectively.

After the quench ($t > 0$), the expectation value of the total energy, for $\langle H(t) \rangle$ is obtained as[183]

$$\langle H \rangle = \sum_{q \neq 0} \mathrm{Im}[v^*(q,t) \partial_t v(q,t)] \, ,$$

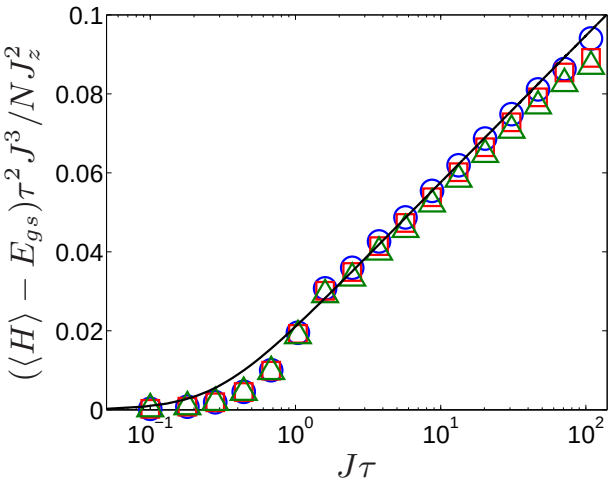

Figure 7.1: The heating is plotted from iTEBD for $J_z/J = 0.1$ (blue circles), 0.2 (red squares) and 0.4 (green triangles) together with the prediction of Eq. (7.7) (black solid line), using $R_0 = 2v\tau_0 = 0.5622$ (from Fig. 7.4). The agreement remains excellent for small variations of R_0 as well.

at $T = 0$. This expression is time independent for $t > \tau$, as expected. For $t > \tau$, and an interaction of finite range, $g_2(q) = g_2 \exp(-R_0|q|/2)$, we obtain for a linear quench

$$\langle H\rangle = E_{gs}\left[1 - \left(\frac{\tau_0}{\tau}\right)^2 \ln\left(1 + \left(\frac{\tau}{\tau_0}\right)^2\right)\right] \tag{7.7}$$

for a linear quench, $\tau_0 \equiv R_0/2v$, and $E_{gs} = -Lg_2^2/4\pi v R_0^2$ is the adiabatic ground state energy shift to lowest order in g_2, with L the system size. The second term corresponds to quasiparticle excitations resulting from the finite quench speed. In the SQ limit, $\tau \ll \tau_0$, the energy of the system is only slightly shifted[197], $\langle H\rangle = E_{gs}(\tau/\tau_0)^2/2$. This holds true for a general quench, i.e. $\langle H\rangle \sim (\tau/\tau_0)^2$ when $\tau \to 0$ with a quench dependent coefficient. In the adiabatic limit, $\tau \gg \tau_0$, on the other hand, the excess energy (or "heating") vanishes as $-2E_{gs}\ln(\tau/\tau_0)\ \tau_0^2/\tau^2$ in accord with the so-called analytic response of Ref. [198]. The crossover between the SQ and adiabatic limits occurs when $\tau \sim \tau_0$, which typically translates to $\tau \sim 1/J$ in an optical lattice, with J the hopping integral in the underlying microscopic lattice Hamiltonian, see e.g. Eq. (1.48).

The heating in the near-adiabatic limit in 1D gapless systems has been addressed in Refs. [199, 197], and non-universal behaviors were found. The universal $\ln(\tau)/\tau^2$ heating seen in Eq. (7.7) was mentioned previously in Ref. [198]. In Fig. 7.1, we compare Eq. (7.7) to the numerical result on XXZ

Heisenberg model in Eq. (1.48), after linearly switching on the interaction, using $R_0 = 0.5622$ as the only free parameter, what we obtain from the bosonic density matrix, and obtain excellent agreement, especially for near-adiabatic quenches.

7.1 Fermionic density matrix

The expectation value of the heating does not depend on the statistics of the original interacting model, i.e. whether we had interacting fermions or bosons, but correlation functions do. Let us start with the discussion of the fermionic correlators. In this context, the structure of the non-equilibrium dynamics can be well demonstrated by means of the fermionic one-particle density matrix. Since the fermion field decomposes to right-going and a left-going parts (see. Eq. (1.35)), it is enough to concentrate on the right-going part of the density matrix,

$$G_r(x,t) \equiv \langle R^+(x,t)R(0,t)\rangle \,, \tag{7.8}$$

describing excitations around the right Fermi momentum, $k \approx k_F$. The right-going field, $R(x)$, can be expressed in terms of the LL bosons as in Eq. (1.36). The expectation value of the above correlator is evaluated following standard steps [71, 72]. In essence, these rely on the observation[74], that for a random variable, ξ with Gaussian probability distribution with zero mean,

$$\langle \exp(i\xi)\rangle = \exp\left(-\frac{\langle \xi^2\rangle}{2}\right). \tag{7.9}$$

We then obtain at $T = 0$

$$G_r(x,t) = G_r^0(x)\exp\left(-\sum_{q>0}\left(\frac{8\pi}{qL}\right)\sin^2\left(\frac{qx}{2}\right)|v(q,t)^2|\right), \tag{7.10}$$

where $G_r^0(x) = i/(2\pi(x+i\alpha))$ denotes the free fermion propagator, with α an ultraviolet regulator. It depends only on $v(q,t)$, i.e. the mixing between b_q and b_{-q}^+ determines the dynamics.

Although the above summation can be transformed to an integral in the thermodynamic limit ($L \to \infty$), which can be performed analytically at $T = 0$, it contains many terms and does not provide us with an intuitive picture about the underlying non-equilibrium dynamics. Therefore, we have expanded these results in various regimes to pinpoint the involved processes.

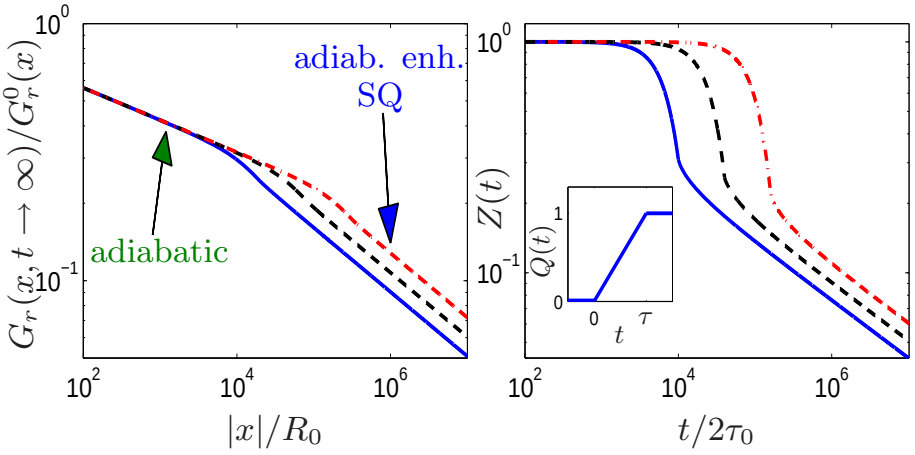

Figure 7.2: Left: the long time ($\tau \ll t \to \infty$), steady state limit of the one-particle density matrix is plotted on loglog scale for a linear quench and $2g_2 = v$ as a function of $|x|$, exhibiting the crossover from adiabatic behavior (lower line in Eq. (7.11)) at small $|x|$ to SQ behavior with adiabatic enhancement (upper line in Eq. (7.11)) at large $|x|$. The curves are plotted for $\tau/2\tau_0 = 10^4$, 4×10^4 and 16×10^4 from bottom to top in both panels. Right: Landau's quasiparticle weight, $Z(t)$ is plotted on a loglog scale as a function of t, bridging between the weakly interacting Fermi liquid to strongly suppressed $Z \ll 1$ with adiabatic enhancement (Eq. (7.12)). Inset: the linear quench protocol is shown.

Let us first discuss the properties of $G_r(x,t)$ long after the quench, $t \gg \tau$. In this limit, independently of the quench protocol, $Q(t)$, the one-particle density matrix exhibits universal properties,

$$\frac{G_r(x,t)}{G_r^0(x)} \sim \begin{cases} A\left(\tau/\tau_0\right)\left(\dfrac{R_0}{\min\{|x|,2vt\}}\right)^{\gamma_{\rm SQ}} & \text{for } |x| \gg 2v\tau, \\ \left(\dfrac{R_0}{|x|}\right)^{\gamma_{\rm ad}} & \text{for } |x| \ll 2v\tau, \end{cases} \tag{7.11}$$

where $\gamma_{\rm SQ} = g_2^2/v^2 + \ldots$ and $\gamma_{\rm ad} = g_2^2/2v^2 + \ldots$ denote the perturbative sudden quench and adiabatic exponents, respectively. The prefactor $A\left(\tau/\tau_0\right)$ depends on the speed of the quench: For a sudden quench it is $A(\tau \ll \tau_0) \sim 1$, while for slower quenches $A(\tau > \tau_0) \sim (\tau/\tau_0)^{\gamma_{ad}}$.

Thus even for $t \to \infty$, instead of one single power-law, G_r interpolates between the SQ and adiabatic limits. This is shown in Fig. 7.2 for a linear quench[183]. Physically, the crossover behavior of G_r is understood as follows: a finite-time quench is experienced by low energy excitations, $\omega(q) < 1/\tau$ as a sudden change, while high energy excitations with $\omega(q) > 1/\tau$ can adjust

to the change in the interaction strength adiabatically. Since high (small) energy excitations determine the short (long) distance correlations, the tail of G_r is governed by the SQ exponent [180], while the short distance behavior is described by the adiabatic exponent. For slow quenches, $\tau \gg \tau_0$, the quench time manifests itself explicitly through an adiabatically *enhanced* prefactor $A \sim (\tau/\tau_0)^{\gamma_{\rm ad}}$ of the asymptotic tail as also shown in Fig. 7.2. Thus while the spatial decay of Eq. (7.11) contains the SQ exponent, its τ dependence reveals the adiabatic LL exponent. For a finite $t \gg \tau$ but $2vt \ll |x|$, $G_r(x,t)$ decays asymptotically as $iZ(t)/2\pi x$, with a finite quasi-particle weight,

$$Z(t \gg \tau, \tau_0) \sim A(\tau/\tau_0) \left(\frac{\tau_0}{t}\right)^{\gamma_{\rm SQ}}. \tag{7.12}$$

Thus the exponent observed in $Z(t)$ is identically $\gamma_{\rm SQ}$ for $t \gg \tau$, but the finite quench time amounts in a quasiparticle weight increased by a factor, $A \sim (\tau/\tau_0)^{\gamma_{\rm ad}}$ for $\tau \gg \tau_0$. Although these results were obtained perturbatively, we expect them to carry over in the non-perturbative limit, except that the exponents $\gamma_{\rm SQ}$ and $\gamma_{\rm ad}$ must be replaced by their exact value.

All these spatial features appear also in the time-dependent momentum distribution of the fermions, $n(k,t)$, directly measurable through time of flight experiments. In particular, at $T = 0$ and finite $t \gg \tau$, $n(k,t)$ exhibits a jump of size $\sim Z(t)$ at $k = k_F$, while it approximately scales for $|\tilde{k}| \gg 1/2vt$ as

$$n(k) - \frac{1}{2} \sim -\mathrm{sign}(\tilde{k}) \times \begin{cases} A(\tau/\tau_0)\, |\tilde{k}R_0|^{\gamma_{\rm SQ}}, & |\tilde{k}| \ll \frac{1}{2v\tau}\,, \\ |\tilde{k}R_0|^{\gamma_{\rm ad}}, & |\tilde{k}| \gg \frac{1}{2v\tau}, \end{cases} \tag{7.13}$$

for $\tilde{k} \equiv k - k_F$, $|\tilde{k}| \ll k_F$, and $t \gg \tau$. Thus the time scale of the quench is also imprinted in the momentum distribution, which also shows a crossover behavior between the SQ and the adiabatic limits. For adiabatic quenches, $\tau \to \infty$, we recover the equilibrium LL exponent, while close to k_F, the momentum distribution is enhanced by a factor $A(\tau/\tau_0)$ compared to the SQ behavior[180, 182].

The above analysis can be extended to the short time region, $t \ll \tau$, where the behavior found depends explicitly on the quench protocol[183] as

$$G_r(x,t) \sim G_r^0(x) \left(\frac{R_0}{\min\{|x|, 2vt\}}\right)^{\gamma(t)}, \tag{7.14}$$

where $\gamma(t) = g_2^2 Q^2(t)/2v^2 + \ldots$. In short distance region, $|x| \ll 2vt$, the spatial correlations are characterized by a weakly interacting LL with time-dependent exponents (t-LL). For $|x| \gg 2vt$, on the other hand, similar to $t \gg \tau$, correlations remain almost unaffected by interaction, and a Fermi

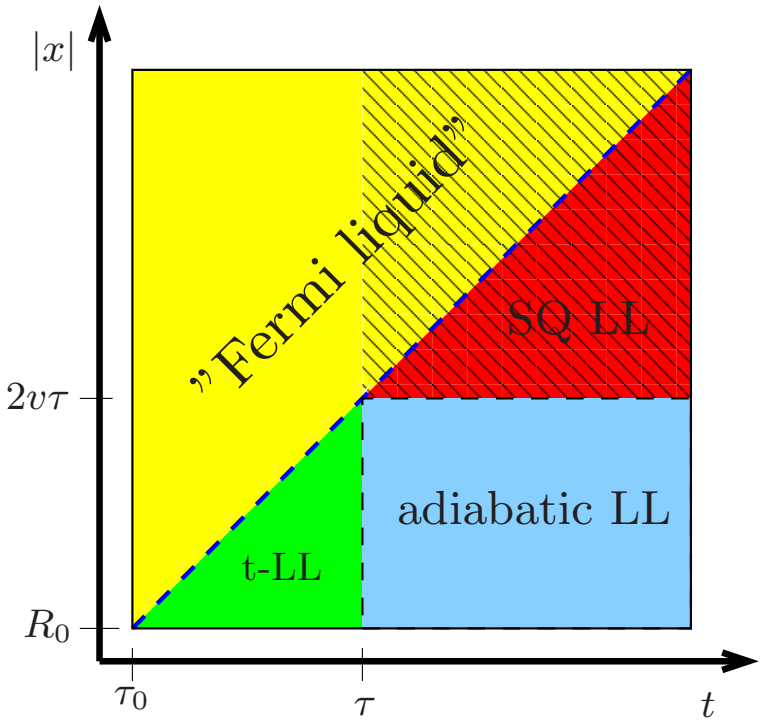

Figure 7.3: The schematic universal spatial-temporal characteristics of a quenched LL, with the boundaries denoting *crossovers*. In the adiabatic LL regime, the LL exponent of the final state, $\gamma_{\rm ad}$ governs spatial correlations, while in the SQ LL region, correlations decay with the SQ exponent, $\gamma_{\rm SQ} > \gamma_{\rm ad}$. Correlations are adiabatically increased by an amplitude, $A \sim (\tau/\tau_0)^{\gamma_{\rm ad}}$ in the shaded region. In the Fermi liquid region a time dependent quasiparticle residue is found (see Eq. (7.15)), while in the time-dependent LL (t-LL) region a quench protocol-dependent weakly interacting LL is found with a time dependent exponent, Eq. (7.14). The dashed line denotes $|x| = 2vt$, i.e. the light-cone[64]. For $\tau \ll \tau_0$, the SQ physics of Ref. [180, 182] dominates everywhere.

liquid regime is found. For $t \ll \tau_0$, $Z(t) \simeq 1$ as in the initial Fermi gas, but for $t \gg \tau_0$ we recover a Fermi liquid behavior with a reduced quasiparticle weight as

$$Z(\tau_0 \ll t \ll \tau) \sim \left(\frac{\tau_0}{t}\right)^{\gamma(t)} \tag{7.15}$$

The quasiparticle weight thus slowly decreases during the quench, and excitations remain similar to those in the initial Fermi gas with a reduced weight ($Z < 1$) for $t < \tau$. After the quench, $t > \tau$, the quasiparticle weight

continues to decrease as a power-law, and it resembles to an interacting heavy fermi system with $1/x$ spatial decay and $Z \ll 1$ quasiparticle residue, Eq. (7.12), as was also found for sudden quenches [181, 182]. This situation is shown in detail in Fig. 7.2, where $Z(t)$ is plotted for the special case of a linear quench[183]. Our results are summarized in Fig. 7.3.

7.2 Density matrix of hard core bosons from the XXZ Heisenberg model

The excess energy could have in principle been obtained by using adiabatic perturbation theory [200], since our perturbative results from Eq. (7.5) capture only the lowest order correction in J_z/J to the above physical quantities. Therefore, we now focus on the spin flip correlation function $\langle S^+S^-\rangle$, which contains the bosonic fields in the exponent, similarly to the fermionic case and demonstrates the non-perturbative nature of bosonization: the present approach yields to first correction in J_z to the *exponent* of the spin-flip correlation function. Perturbation theory would only yield the lowest order correction to the whole correlator, and not to its exponent. Thus, it requires the non-perturbativeness of bosonization to account for the numerical data and to produce power-law correlation functions.

The most singular, staggered part of the transverse magnetization [72], which is directly related to the hard core boson creation operator, is given by

$$S^+(x) = \frac{(-1)^x}{\sqrt{2\pi\alpha}} \exp(-i\theta(x)), \tag{7.16}$$

where

$$\theta(x) = \sum_{q\neq 0} \sqrt{\frac{\pi}{2|q|L}} \mathrm{sgn}(q) \exp\left(-\frac{\alpha|q|}{2}\right) \left(\exp(iqx)b_q + \exp(-iqx)b_q^+\right). \tag{7.17}$$

$S^+(x)$ is also the hard core boson creation operator in the continuum limit, and α is a short distance cutoff. The $\theta(x)$ function differs from $\phi_+(x)$ from Eq. (1.44) by containing negative q modes, which is the direct consequence of the Jordan-Wigner string operator in Eq. (1.50), responsible for the transformation of fermions into hard-core bosons.

The spin flip correlation function of the XXZ model, which corresponds to the hard-core boson single particle density matrix, is obtained as

$$G_B(x,t) = \langle S^+(x,t)S^-(0,t)\rangle, \tag{7.18}$$

which is evaluated similarly to Eq. (7.8) using Eq. (7.9).

Right after the quench at $t = \tau$ and in the $|x|, v\tau \gg R_0$ limit, the spin flip correlation function reads as

$$G_B(x,\tau) \approx \frac{C(-1)^x}{\sqrt{|x|}} \exp\left(-\frac{g_2}{2v} f\left(\frac{x}{2v\tau}\right)\right)\left(\frac{R_0}{x}\right)^{g_2/2v}, \qquad (7.19)$$

where $C = \sqrt{e}2^{-1/3}A^{-6}$ stems from the correlator of hard core bosons on a lattice in, e.g., the XY model ($g_2 = 0$), $A = 1.28243\ldots$ is Glaisher's constant [201]. These non-perturbative results are tested against numerics in Fig. 7.4, where we fix $R_0 = 0.5622$ from Fig. 7.4. Similarly to the previous comparisons, the agreement is excellent and works qualitatively upto rather large J_z.

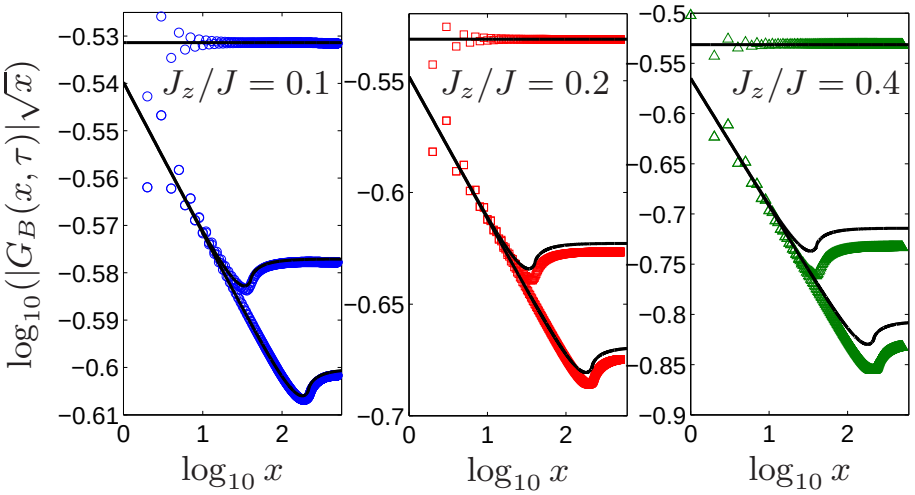

Figure 7.4: The spin flip correlation function is shown for $J_z/J = 0.1$ (left panel), 0.2 (middle panel) and 0.4 (right panel) for $J\tau = 0$, 20.2 and 108.3 from top to bottom with $R_0 = 0.5622$ from Eq. (7.19), together with the numerical data. The power-law exponent changes from $-\frac{1}{2} - \frac{J_z}{\pi J}$ for $x \ll v\tau$ to $-\frac{1}{2}$ for $x \gg v\tau$, as $|G(B(x,\tau)|\sqrt{|x|} \approx C(R_0/\min[x, 2v\tau/e])^{g_2/2v}$. Results from the XY model [201] fix the prefactor of the correlation function as well, leaving R_0 as the only adjustable parameter. The $\tau = 0$ results correspond to that in the XX Heisenberg model [201]. At short distances, the correlator is strongly influenced by the presence of the lattice.

The short distance behaviour ($< v\tau$) in Fig. 7.4 is dominated by high energy ($> 1/\tau$) modes, evolving adiabatically. The correlators thus behave identically to the adiabatic case ($\tau \to \infty$). However, the long distance ($> v\tau$) response is dictated by low energy ($< 1/\tau$) modes, feeling a sudden

quench, and the observables in this range reveal the sudden quench behaviour ($\tau \to 0$). We have also checked that the numerical data for time dependent correlators are also successfully described by our bosonization scheme.

After the quench ($t \gg \tau$), Eq. (7.18) still applies after changing τ to t. The momentum distribution (MD), i.e. the spatial Fourier transform of Eq. (7.18), to first order in g_2 behaves as

$$n(\tilde{k}, t) \sim \tilde{k}^{-1/2} \max\left(R_0 \tilde{k}, \frac{R_0}{vt}\right)^{-g_2/2v}, \tag{7.20}$$

where $\tilde{k} = ||k| - \pi|$. In the steady state, it remains identical to the adiabatic expression[71, 72] in spite of the quench, as opposed to the fermionic case in Eq. (7.13), which highlight the essential role of the string operators $\sum_{m<l} n_m$ in the Jordan-Wigner transformation in Eq. (1.50). Had we taken a ferromagnetic coupling ($J < 0$), the divergence would occur at $k = 0$ as is the case normally for hard core bosons [202]. The steady state ($t \to \infty$) response thus coincides with the equilibrium one to first order in the exponent, irrespective of the quench time. Higher order terms, however, will modify the exponent [183]. Eq. (7.20) is directly accessible experimentally using time-of-flight imaging of quenched hard core bosons, similarly to fermions.

To summarize, we have applied the Luttinger model description for a lattice model outside the usual equilibrium description, by deriving quantities using an out-of-equilibrium Luttinger liquid theory and comparing them to exact numerical calculations on the XXZ chain[184]. Remarkably, even though our bosonization calculations are perturbative in J_z, they provide an excellent quantitative description even for moderately large J_z values.

7.3 Statistics of work done during a quantum quench

So far, we have concentrated on simple physical observables such as the energy of single particle density matrix, which can be expressed in terms of few point correlation functions. We have shown that the time-dependent Luttinger model describes successfully such instances. However, it is not clear whether arbitrary high order correlators can also be well described using the present approach. Additionally, the full characterization of a quantum state is only possible through its all higher moments, encoding unique information about non-local correlations of arbitrary order and entanglement[203], similarly to how a random variable is characterized by all of its moments or equivalently, by its probability distribution function. Thus, calculating all

possible arbitrary order correlations functions is equivalent to determining the full distribution function of the quantity of interest. While its equilibrium evaluation is already rather involved[203], obtaining the full non-equilibrium distribution function of a physical observable has rarely been carried out[204].

Recently, using recent developments in non-equilibrium statistical physics, a delightful exception is found, which is the statistics of work done during a quench, which has been studied in Refs. [205, 206] for a sudden quench between *gapped* phases, separated by a quantum critical point. The probability distribution function (PDF) of work done, $P(W)$, involves all possible moments of energy[207], thus providing us with full characterization of the energy distribution.

The goal of this section is to calculate the PDF of work done on a Luttinger liquid after an interaction quench[185], and construct explicitly the diagonal ensemble which reproduces all moments of $P(W)$. We remark that this is one of the rare occasions, where the diagonal ensemble can be constructed analytically for an interacting model.

To this end, we consider the the time-dependent Luttinger model from Eq. (1.42), which is interaction quenched by a given protocol into a final LL liquid state, as described by Eq. (7.1).

Armed with the formal solution of the time-dependent Bogoliubov equations, Eq. (7.3), we analyze the statistics of work done. Albeit the work done has been studied in classical statistical mechanics exhaustively, its quantum generalization has been carried out only recently [207], and its properties are known for very few systems. The quantum work cannot be represented by a single Hermitian operator ($\Leftrightarrow$ work is not an observable[208]), but rather its characterization requires two successive energy measurements, one before and one after the time dependent protocol (thus work characterizes a process). The knowledge of all possible outcomes of such measurements yields the full probability distribution function (PDF) of work done on the system.

The characteristic function of work after the quench, which is the Fourier transform of the PDF of work, $P(W)$, can be expressed as [207]

$$G(\lambda,\tau)=\langle \exp[i\lambda H_H(t>\tau)]\exp[-i\lambda H_H(0)]\rangle\ , \tag{7.21}$$

where $H_H(t)$ is the Hamilton in the Heisenberg picture, and the expectation value is taken with the initial thermal state. For a sudden quench (SQ), $\tau=0$, and $G(\lambda,\tau)$ coincides with the Loschmidt echo [205], to be discussed in more detail at the end of this chapter. The expectation value of the characteristic function of work done is independent of t for $t>\tau$, but depends on the details of the quench protocol. $H_H(t)$ is obtained by expressing the time dependent boson operators in Eq. (7.1) using Eq. (7.3). Eq. (7.21) can

then be evaluated at $T = 0$ upon realizing that the operators

$$K_0(q) = (b_q^+ b_q + b_{-q} b_{-q}^+)/2, \quad K_+(q) = b_q^+ b_{-q}^+, \quad K_-(q) = b_q b_{-q} \tag{7.22}$$

are the generators of a SU(1,1) Lie algebra, satisfying

$$[K_+(q), K_-(q)] = -2K_0(q), \quad [K_0(q), K_\pm(q)] = \pm K_\pm(q), \tag{7.23}$$

and the operators for distinct q's commute with each other. Using Ref. [185], we finally obtain

$$\ln\ G(\lambda, \tau) = i\lambda E_{ad} - \sum_{q>0} \ln\left(1 + n_q(1 - e^{2i\,\Omega_q \lambda})\right), \tag{7.24}$$

with $E_{ad} = E_f - E_i$ the difference between the adiabatic ground state energies in the final and initial state, and $n_q = [\omega_q(t) - \Omega_q + 2\mathrm{Im}\{v_q^*(t)\partial_t v_q(t)\}]/2\Omega_q$ the time independent occupation number of mode q in the final LL state, and $\Omega_q = \sqrt{\omega_q^2(t > \tau) - g_q^2(t > \tau)}$ the corresponding excitation energy [71].

Eq. (7.24) depends only on the occupation numbers of the steady state therefore the diagonal ensemble may describe the final state [66]. The analytic construction of the final density matrix is very hard. Therefore, one typically focuses only on few body observables, and tries to build an approximate density matrix describing these. Such an approach is, however, not sufficient to account for the complete PDF of work, which depends on all possible moments of energy. In. Ref. [185], we have constructed explicitly the density matrix of the diagonal ensemble for the Luttinger model, describing arbitrary order correlation functions after the quench.

To obtain an analytical understanding of the PDF of work, we expand Eq. (7.24) for small $g_2(q)$. For large system sizes L, the characteristic function of work done reads as

$$\frac{\ln G(\lambda, \tau)}{iE_{ad}} = \lambda - \int_0^\tau \int_0^\tau dt_1 dt_2 Q'(t_1) Q'(t_2) \tau_0 \left[f(t_1 - t_2 + \lambda) - f(t_1 - t_2)\right]. \tag{7.25}$$

Here $E_{ad} < 0$ is defined in Eq. (7.7) and $f(t) = \tau_0/(t + i\tau_0)$. The cumulants, C_n of the work done can be derived by expanding Eq. (7.25) in power series as $\ln\left(\tilde{G}(\lambda, \tau)\right) = \sum_{n=1}^\infty C_n (i\lambda)^n/n!$, and are shown in Fig. 7.5.

To analyze the PDF of work, we introduce the dimensionless work, measured with respect to the adiabatic ground state energy shift,

$$w \equiv (W - E_{ad})/|E_{ad}|\ . \tag{7.26}$$

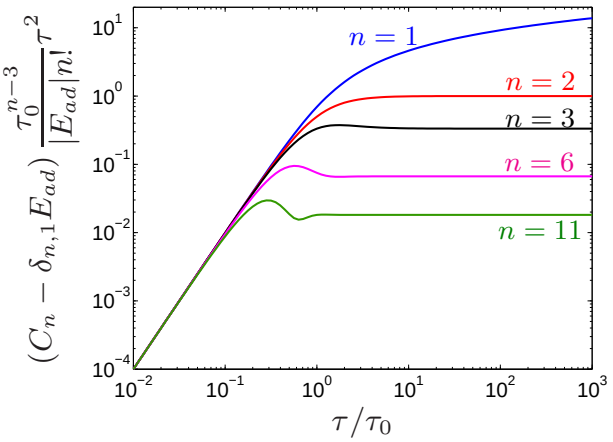

Figure 7.5: Several cumulants of the work done on a LL are log-log plotted as a function of the quench time for a linear protocol. Close to the SQ limit ($\tau \ll \tau_0$), all properly normalized cumulants are equal, while in the near adiabatic limit ($\tau \gg \tau_0$), these approach $2/n(n-1)$.

The distribution of w is then obtained by the Fourier transform of its characteristic function,

$$p(w) = \mathcal{P}_{ad}\,\delta(w) + \rho(w)\,. \tag{7.27}$$

The Dirac-delta peak corresponds to the probability of staying in the adiabatic ground state, while the broad structure $\rho(w)$ is associated with transitions to excited states with $w > 0$.

In the adiabatic limit ($\tau \to \infty$), a finite system always stays in its ground state, and the time evolved wave function coincides with the lowest energy eigenfunction of the instantaneous Schrödinger equation [209]. Consequently, only the first term remains in Eq. (7.27) with $\mathcal{P}_{ad} = 1$. For $\tau \ll \tau_0$, on the other hand, $\mathcal{P}_{ad}$ scales as $\sim \exp(-\alpha) \sim \exp(-cst.\ L)$ (see Fig. 7.6), and in the limit $L \to \infty$ — but fixed interaction — $\mathcal{P}_{ad}$ vanishes due to the orthogonality catastrophe. Here, $\alpha = |E_{ad}\tau_0| \sim N(g_2/v)^2$ denotes the total angle of Bogoliubov rotations ($N \sim L/v\tau_0$ is the number of particles), and can be viewed as the many-body orthogonality exponent. It is also closely related to the fidelity susceptibility [210]: $\alpha \gtrless 1$ describes the thermodynamic / small system limits [210].

In the extreme SQ limit [182, 180, 181] $\tau \ll \tau_0$, $G(\lambda, \tau)$ simplifies to $G(\lambda) = \exp\left[iE_{ad}\lambda^2/(\lambda + i\tau_0)\right]$, and the continuum part of the PDF of work is evaluated exactly as

$$\rho_{\rm SQ}(w) = \mathcal{P}_{ad}\ \exp(-\alpha w)\ \alpha\ w^{-1/2}\ I_1\big(2\alpha\sqrt{w}\big)\ , \tag{7.28}$$

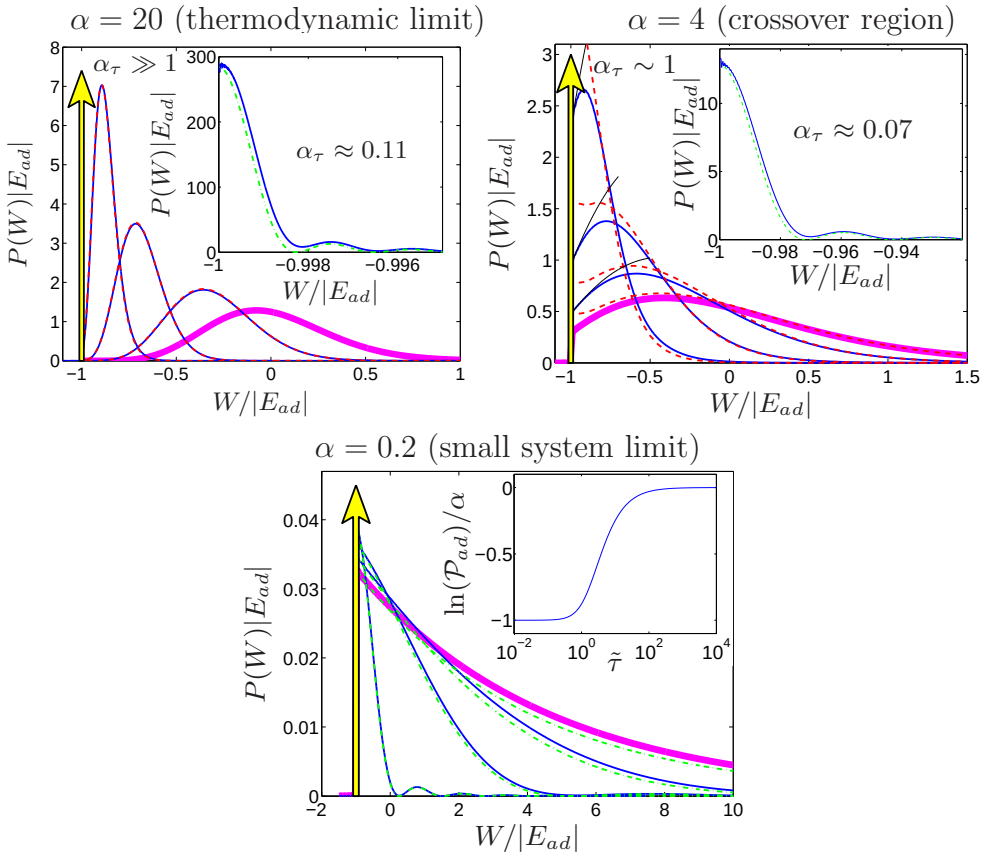

Figure 7.6: The PDF of work done on a LL is plotted after a linear quench from the numerical evaluation of Eq. (7.25) (blue solid line). Top left panel: $\alpha = 20$ with $\tilde{\tau} = 0$, 1, 2.5 and 5 from right to left and 180 (inset, $P(W > E_{ad})$ only); Top right panel: $\alpha = 4$ with $\tilde{\tau} = 0$, 1, 2 and 4 with increasing peak height and 55 (inset); bottom panel: $\alpha = 0.2$ with $\tilde{\tau} = 0$, 2, 5, and 25 from right to left. The thick magenta line denotes the exact SQ expression (Eq. (7.28)), the red dashed line represent Eq. (7.31), the thin black line in the middle panel visualizes Eq. (7.30), while the green dash-dotted line shows the result in the small system limit[185]. The vertical arrow at $W = E_{ad}$ denotes the Dirac-delta peak, whose spectral weight $\mathcal{P}_{ad}$ is shown in the inset of the right panel on semilog scale as a function of the ramp time τ.

with $\mathcal{P}_{ad} = \exp(-\alpha)$ and $I_1(x)$ the modified Bessel function of the first kind. This is the non-central χ^2 distribution with non-centrality parameter 4α in the limit of zero degrees of freedom [211]. The average work is zero [183], since for a SQ the system remains in its initial state and — on average — there is no back reaction. Entropy is, however, generated by populating high

and low energy configurations.

The shape of $\rho(w)$ depends crucially on the orthogonality parameter, α. The thermodynamic limit, $\alpha \gg 1$ reveals universal behaviour: almost all probability weight is carried by a peak centered at around $W = 0$ ($w = 1$) and of width $\Delta W \sim |E_{ad}|/\sqrt{\alpha}$,

$$\rho_{\rm SQ}^{\alpha\gg 1}(w \gg \alpha^{-2}) \approx \frac{\exp\left(-\alpha\left[1-\sqrt{w}\right]^2\right)}{w^{3/4}\sqrt{4\pi\alpha^{-1}}} \,, \tag{7.29}$$

whose high energy tail decays according to the Gamma distribution, $\sim \exp(-\alpha w)/w^{3/4}$. In the small system regime $\alpha \ll 1$, on the other hand, the delta function retains almost all spectral weight, and transfers only a fraction $\sim \alpha$ to an exponential distribution of width $\Delta W \sim |E_{ad}|/\alpha$ and threshold at E_{ad} for $w \ll \alpha^{-2}$. In the crossover regime, $\alpha \sim 1$, the maximum shifts to lower energies and the PDF of work develops a sizable value right above the threshold at E_{ad} (see Fig. 7.6). The maximum of $P(W)$ occurs at $W > E_{ad}$ for $\alpha > 2$, while the PDF becomes monotonically decreasing for $\alpha < 2$.

For finite quenches times, in addition to the orthogonality parameter α, the work statistics also depends on τ and the protocol $Q(t)$ itself. For definiteness, we focus here on a linear quench, and measure the degree of adiabaticity by $\tilde{\tau} = \tau/\tau_0$.

For a finite duration quench, $\tilde{\tau} > 1$, only a fraction $1/\tilde{\tau}$ of the excitations experiences the quench as sudden. Consequently, in the expression of $\mathcal{P}_{ad}$, the orthogonality exponent α is replaced by $\alpha_\tau \sim \alpha/\tilde{\tau}$, and $\mathcal{P}_{ad}$ becomes a monotonously increasing function of $\tilde{\tau}$ (see Fig. 7.6). The crossover with increasing α_τ from $\mathcal{P}_{ad} \lesssim 1$ to vanishingly small spectral weight, $\mathcal{P}_{ad}$, occurs at $\alpha \sim \tilde{\tau}$.

Close to the threshold, $W - E_{ad} \ll 1/\tau$, only states with energy smaller than $1/\tau$ and thus feeling a SQ contribute to work. Therefore, apart from a normalization factor, the PDF of work agrees with the SQ result and we obtain

$$\rho(w \ll \alpha^{-1}\tilde{\tau}^{-1}) \approx \mathcal{P}_{ad}\exp(\alpha)\rho_{SQ}(w) \,, \tag{7.30}$$

and depends on τ only through $\mathcal{P}_{ad}$.

For $\tilde{\tau} \gg 1$, however, Eq. (7.30) describes only a small region close to E_{ad} (see thin black lines in Fig. 7.6), and the overall shape depends both on α and $\tilde{\tau}$. For $4\alpha \gg \tilde{\tau}$, almost all spectral weight is carried by the non-adiabatic processes ($\rho(w)$) around the typical value $W_{typ} - E_{ad} \sim 2|E_{ad}|\ln(\tilde{\tau})/\tilde{\tau}^2$, clearly separated from the adiabatic process. For $\tilde{\tau} \gg 4\alpha$, the adiabatic process

gains spectral weight, $\mathcal{P}_{ad} \approx 1$, but a maximum for $W > E_{ad}$ remains present, though it gradually merges with the adiabatic processes.

In the small system limit $\alpha_\tau \ll 1$, the system evolves almost adiabatically, non-adiabatic processes have only a small probability $\sim \alpha/\tilde{\tau}$, and the typical work done in case of a rare non-adiabatic process is $W_{typ} \approx -\alpha^2\pi/\tau$.

Increasing α, the zeros of the PDF turn gradually into dips, and the PDF develops a more universal form. In the thermodynamic limit $\alpha_\tau \gg 1$, using the method of steepest descent we obtain

$$\rho(w) \approx \frac{\mathcal{P}_{ad}\tilde{\tau}^{3/2}\sqrt{\alpha}}{2\sqrt{\tan^3(s)\pi}} \exp\left(w\left(\frac{\tilde{\tau}^2}{2} - \alpha\right) + 2\frac{\alpha s}{\tilde{\tau}}\right) \tag{7.31}$$

for $\alpha s \gg \tilde{\tau}$, with $s \equiv \arctan[\sqrt{\exp(w\tilde{\tau}^2) - 1}]$. For $w \gg 1/\tilde{\tau}^2 \gg 1/\alpha^2$, $\rho(w)$ in Eq. (7.31) behaves as a generalized Gumbel distribution of index $a = \frac{1}{2} + \frac{2\alpha}{\tilde{\tau}^2}$ [212]. This latter emerges in the context of global fluctuations, describing the limit distribution of the a-th maximum of a sequence of independent and identically distributed random variables [203]. The distribution in the $1/\tilde{\tau}^2 \gg w \gg 1/\alpha^2$ region resembles closely to Eq. (7.29) apart from its normalization.

Experimentally, these results can be tested on one-dimensional hard-core bosons [213] or non-interacting fermions as initial states. The detection of the PDF of work requires two energy measurements, one before and one after the time dependent protocol. The first energy measurement can be omitted if we prepare the initial wave function in an energy eigenstate of $H(t = 0)$. The resulting energy distribution can then be probed using time-of-flight experiments [66, 63], similarly to Ref. [214]. The crossover between the various regimes can be monitored by tuning τ/τ_0 and $\alpha \sim N\,(g_2/v)^2$, where N is the number of particles in a 1D trap, typically with $N \sim 10^2$ - 10^3 atoms [70, 67, 69]. By choosing $g_2/v \sim 1/\sqrt{N}$, α becomes of order unity, facilitating the observation of crossover between the various regimes. For one-dimensional interacting bosons (i.e. Bose-Hubbard model), $v \sim J$ and $g_2 \sim J^2/U$ for $U \gg J$ (close to the hard-core boson limit) with U the on-site interaction [98] and J the hopping amplitude. By quenching away from the initial $U \gg J \Leftrightarrow g_2 \approx 0$ limit (e.g. by changing the lattice parameters or tuning the Feshbach resonance), a final interaction $U \sim J\sqrt{N}$ is reachable. For weakly interacting fermions, $v \sim J$ and $g_2 \sim U$, therefore ramping from the weakly interacting case to $U \sim J/\sqrt{N}$ is desirable.

We have studied the PDF of work done on a LL after an interaction quench[185]. The PDF exhibits markedly different characteristics depending on the system size, quench duration and interaction strength.

7.4 Loschmidt echo in LLs and in the XXZ Heisenberg chain

The Loschmidt echo (LE) provides direct insight into the dynamical properties of the quantum-many body state, without reference to any particular observable. It is defined as the overlap of two wave functions, $|\Psi_0(t)\rangle$ and $|\Psi(t)\rangle$, evolved from the same initial state, but with different Hamiltonians, H_0 and H,

$$\mathcal{L}(t) \equiv |\langle\Psi_0(t)|\Psi(t)\rangle|^2 . \tag{7.32}$$

Josef Loschmidt was an Austrian scientist, who became famous by his critique to Ludwig Boltzmann's work on the entropy, known as the reversibility paradox. According to Boltzmann, during the time evolution of a system, its entropy should increase with time. Loschmidt pointed out that by reversing the time at the end and evolving the final state backwards, the entropy must decrease. Therefore, Eq. (7.32) reflects Loschmidt's idea and measures the "distance" between two quantum states and quantifies irreversibility and chaos in quantum mechanics[215, 216, 217]. Furthermore, it can be used to diagnose quantum phase transitions[209], and is also an important quantity in various fields of physics, ranging from nuclear magnetic resonance to quantum computation and information theory. While the LE for local perturbations, which is related to the X-ray edge singularity, is well understood, its behavior in quantum many-body systems is poorly described [218, 219, 220, 221].

Here we study the interaction driven LE of a genuine interacting one-

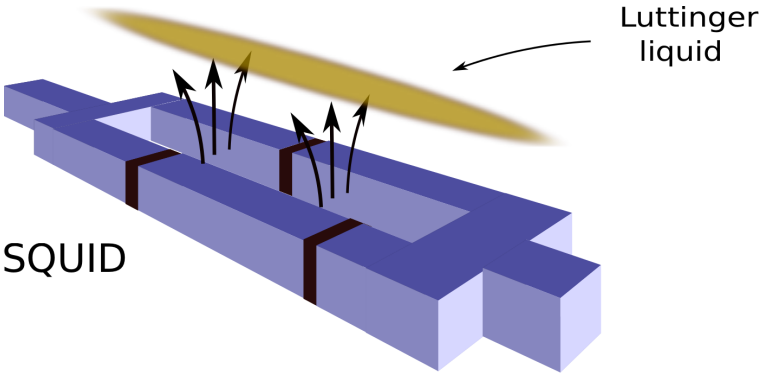

Figure 7.7: Schematics of the experimental setup. The black segments on the SQUID denote the Josephson junctions, the arrows stand for the total magnetic field. By changing the eigenstate of the flux qubit, the total flux hence the total magnetic field changes, controlling the Feshbach resonance in the cold atomic LL.

dimensional system, a Luttinger liquid (LL). We evaluate the LE within the Luttinger liquid (LL) description for a time dependent Hamiltonian. To test and validate the LL predictions, which neglects many irrelevant terms, we also investigate numerically the XXZ Heisenberg chain, containing all sorts of irrelevant terms [71], using MPS based methods. An experimental setup is also proposed to measure the LE of a Luttinger liquid, where a flux qubit coupled to a Feshbach resonance is used to control the interaction in one-dimensional cold atom gas (see Fig. 7.7).

We start from a more general setting than in Eq. (1.42), where already the initial LL state is interacting as

$$H_0 = \sum_{q\neq 0} \left(\omega_q a_q^+ a_q + \frac{g_i(q)}{2} [a_q a_{-q} + a_q^+ a_{-q}^+] \right) , \tag{7.33}$$

where $g_i(q)$ is the initial interaction. We assume that $H = H(t)$ has the same form as Eq. (7.33), but with a time dependent coupling,

$$g_q \to g_q(t) = g_i(q) + \Delta g_q(t), \tag{7.34}$$

where $\Delta g_q(t) = [g_f(q) - g_i(q)]Q(t)$, and $g_f(q)$ is the final interaction strength, and $Q(t)$ encodes again the details of the quench protocol.

The Hamiltonian $H(t)$ is quadratic, and can be diagonalized at any instance. Its initial and final quasiparticle spectra are simply given by $\omega_{i/f}(q) = (\omega_q^2 - g_{i/f}^2(q))^{1/2}$, and the strength of interaction in these states is conveniently characterized by the dimensionless LL parameters,

$$K_{i/f} = \sqrt{\frac{\omega_q - g_{i/f}(q)}{\omega_q + g_{i/f}(q)}} . \tag{7.35}$$

We first diagonalize Eq. (7.33) by a standard, time independent Bogoliubov transformation. In this basis, $H(t)$ reads

$$H = \sum_{q\neq 0} \omega(q,t) b_q^+ b_q + \frac{g(q,t)}{2} [b_q b_{-q} + b_q^+ b_{-q}^+] + \dots \tag{7.36}$$

with $\omega(q,t) = \omega_i(q) - \Delta g_q(t) \frac{g_i(q)}{\omega_i(q)}$ and $g(q,t) = \Delta g_q(t) \frac{\omega_q}{\omega_i(q)}$, and the dots stand for an unimportant time dependent energy shift. The resulting Hamiltonian is then analyzed similarly to Eq. (1.42).

After some tedious calculations[186], the LE takes a particularly simple form

$$\mathcal{L}(t) = \exp\left(- \sum_{q>0} \ln\left(|u_q(t)|^2 \right) \right) , \tag{7.37}$$

where $u_q(t)$ is the time-dependent Bogoliubov coefficient, describing Eq. (7.36) from Eq. (7.4). This result determines the complete time dependence of the generalized LE in a LL and holds for any non-equilibrium evolution. This applies to any quadratic bosonic Hamiltonian such as a Bose-Einstein condensate or the Dicke model. We regularize the q sums in (7.37) by an $\exp(-\alpha|q|)$ factor, with $1/\alpha$ an ultraviolet cutoff[71].

We can now use the function $Q(t)$ to calculate the LE. Changing $Q(t)$ adiabatically, the LE is just the overlap of the ground states of the initial and final Hamiltonian and, in agreement with Refs. [222, 152], reads as

$$\mathcal{L}_{ad} = \left(\frac{1}{2} + \frac{1}{4}\left(\frac{K_i}{K_f} + \frac{K_f}{K_i}\right)\right)^{-L/2\pi\alpha}, \tag{7.38}$$

with L being the system size. This remains valid in the steady state for near-adiabatic quenches, $\tau \gg \alpha/v$ with v being the sound velocity in the final state.

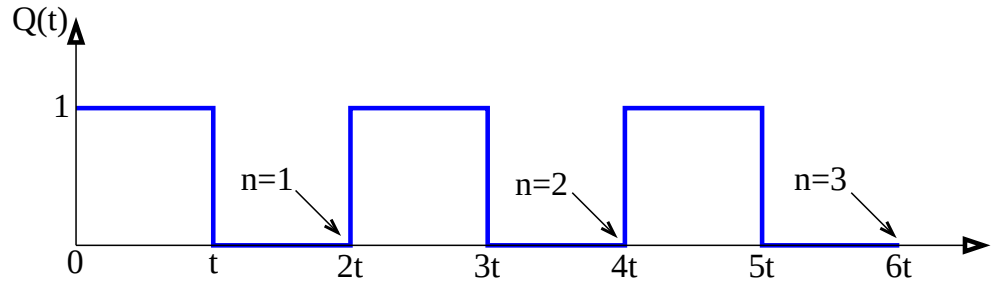

Figure 7.8: (Color online) The bang-bang protocol is visualized up to $n = 3$. The arrows indicate the time instant when the overlap is calculated for an nth order protocol.

For a SQ [180], however, Eq. (7.4) yields

$$|u_q(t)|^2 = 1 + \frac{1}{4}\sin^2(\omega_f(q)t)\left(\frac{K_f}{K_i} - \frac{K_i}{K_f}\right)^2, \tag{7.39}$$

with $\omega_f(q) = v|q|$ denoting the excitation energy after the quench. By plugging this back to Eq. (7.37), we find for the short time limit ($t \ll \alpha/v$)

$$\mathcal{L}_{SQ}(t) \sim \exp\left(-c\, L\, (t/t_c)^2/\alpha\right) \tag{7.40}$$

where c is a non-universal constant of order unity. The characteristic decay time of this expression is $t_c \equiv 4\alpha/v|K_f/K_i - K_i/K_f|$, and $1/t_c^2$ can be identified as the variance of energy per particle after the quench. For intermediate

times $t \sim t_c$, the LE displays a non-universal transient signal (see Fig. 7.9b), however, for very long times, $t \gg \alpha/v$, the LE for SQ becomes time independent and universal. This can be determined by substituting Eq. (7.39) back to Eq. (7.37), expanding the logarithm, then performing the momentum integral in the $t \gg \alpha/v_f$ limit, and finally resumming of the resulting series gives

$$\mathcal{L}_{SQ}(t \gg \alpha/v) = \left(\frac{1}{2} + \frac{1}{4}\left(\frac{K_i}{K_f} + \frac{K_f}{K_i}\right)\right)^{-L/\pi\alpha}, \tag{7.41}$$

which holds also true for fast quenches, $\tau \ll \alpha/v$. Excitations are only produced at $t = 0$, which interfere with each other for a short amount of time, causing Eq. (7.40), but after this phase coherence is lost, excitations propagate independently and only their total number determines the overlap. Eqs. (7.38) and (7.41) implies that for $t \to \infty$

$$\mathcal{L}_{SQ} = \mathcal{L}_{ad}^2. \tag{7.42}$$

The exponent of the LE is further enhanced[186] by repeating the $Q(t > 0)$: SQ to 1, holding time t, SQ to 0, holding time t sequence n times (bang-bang protocol, visualized in Fig. 7.8). The generalized LE is the nth power of the SQ overlap in Eq. (7.41) as $\mathcal{L}_n(2nt) = \mathcal{L}_{SQ}^n(t) = \mathcal{L}_{ad}^{2n}$ in the post-quench steady state, therefore the exponent is enhanced by a factor of n.

We compared the analytical results to numerical data obtained on the one-dimensional XXZ Heisenberg model[71] in Eq. (1.48) by Frank Pollmann using MPS based methods[186], covering $1/2 < K < \infty$, for adiabatic ramps and SQs from $J_z = 0$ to a finite J_z.

The factor $L/\pi\alpha$ in the exponent in Eqs. (7.38) and (7.41) contains the unknown short distance cutoff. However, its value can be fixed by calculating the fidelity susceptibility, χ_f, around the non-interacting XX point of the Heisenberg model, in which case $L/2\pi\alpha \approx N\chi_f\pi^2$, where N is the number of lattice sites and $\chi_f \approx 0.0195$[223]. Using then the Bethe Ansatz result [71] for the LL parameter K from Eq. (1.53), we find an excellent agreement with the numerical data with *no* fitting parameter (see Fig. 7.9a). This excellent agreement is somewhat surprising since, as expected, the non-universal transient signals clearly differ in the LL approach and the numerics, and also, because the LL description completely neglects (asymptotically irrelevant) back scattering processes, contained in the lattice calculations.

Slight deviations are only visible close to the end points of the critical region of the XXZ Heisenberg model in Fig. 7.9, where a description based on the Luttinger model becomes less accurate, as discussed in the Introduction. Close to the $J_z = J$ point, the neglected back scattering term, driving

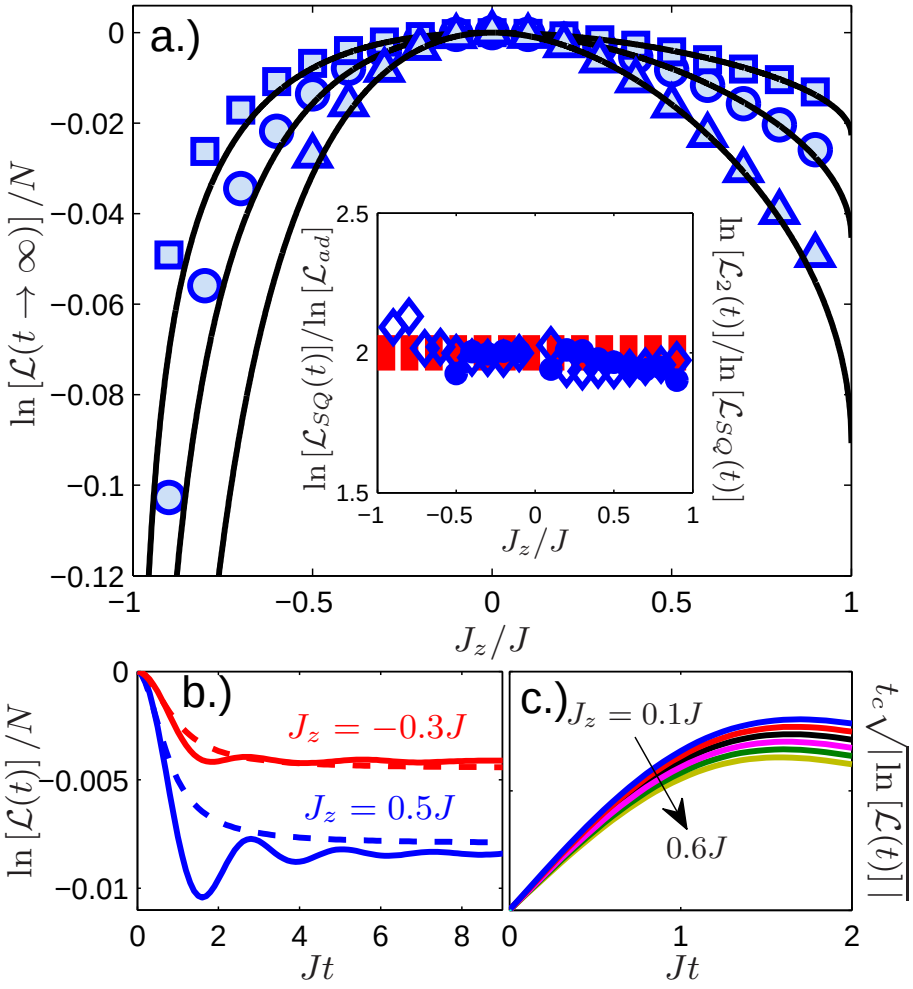

Figure 7.9: a.) The exponent of the generalized Loschmidt echo is shown for SQ $n = 1$ (circle), double quench $n = 2$ (triangle) and adiabatic time evolution (square) for the XXZ Heisenberg model in the steady state, starting from the XX point and ending up at a finite J_z, obtained numerically from MPS based methods. The solid lines are the analytical results from Eqs. (7.38) and (7.41). The inset shows the ratio of the SQ and adiabatic exponents (diamond) and the $n = 2$ and 1 exponents (circle) from numerics, which agrees with the expected value of 2. b.) Typical numerical results (solid lines) of the LE of the XXZ model are shown for a SQ from the XX point to $J_z = 0.5J$ and -0.3J, the dashed curve is the analytical expression using Eqs. (7.37) and (7.39). c.) The scaling of the numerical data expected from Eq. (7.40) for short times for a SQ is visualized from $J_z = 0$ to $0.1J$ to $0.6J$ with $0.1J$ steps from top to bottom in arbitrary units.

the Kosterlitz-Thouless phase transition causes a slight disagreement. Upon approaching the ferromagnetic critical point at $J_z = -J$, on the other hand, the validity of bosonization shrinks to very small energies, and the high energy modes, which are not accounted for properly by the Luttinger model, also influence the overlap.

We propose to measure the LE of the LL in a cold atomic setting, where a flux qubit[224, 225] is used to control the interaction between the atoms. The flux qubit consists of a Josephson junction circuit, and is governed by the Hamiltonian $H_{\rm qubit} = \epsilon\sigma_z + \Delta\sigma_x$, with Δ the tunneling between the two eigenstates of σ_z, $|\circlearrowleft\rangle$ and $|\circlearrowright\rangle$, carrying oppositely circulating persistent currents, $\pm I$, and ϵ the energy splitting. In addition to the external flux, $\Phi_{\rm ext}$, the states $|\circlearrowleft\rangle$ and $|\circlearrowright\rangle$ generate an additional flux $\mp\Phi_f$. Ideally, tunneling between them is suppressed.

The one-dimensional quantum gas is positioned above the flux qubit (see Fig. 7.7), such that the total magnetic field of the state $|\circlearrowright\rangle$ of flux $\Phi_{\rm ext} + \Phi_f$ be at a Feshbach resonance, while the field of the state $|\circlearrowleft\rangle$ of flux $\Phi_{ext} - \Phi_f$, be further away from the resonance. The qubit switching-induced magnetic field difference is estimated for an elongated rectangular flux qubit, using the Boit-Savart law, with parallel sides comparable to the length of a typical cold atomic tube (~ 10 μm). Assuming a persistent current of $I = 2$ μA and a separation of 2 μm between the two lines of the qubit, we obtain a field difference $\delta B_f \sim 16$ mG. Although relatively small, this field is comparable to the width $\Delta B = 15$ mG of some narrow Feshbach resonances used to realize a LL in ^{87}Rb systems [226].

In this setup, one could use rf spectroscopy to measure the absorption spectrum of the qubit in the presence and in the absence of the trapped gas, similarly to the X-ray edge singularity problem[72]. This absorption signal is just proportional to the Fourier transform of the LE. Alternatively, the LE can be measured using Ramsey interferometry[220, 219]: initializing the qubit in the $|\circlearrowleft\rangle$ state with weak interactions to the cold atoms, yields a wavefunction $|\circlearrowleft\rangle\otimes|\Psi_0\rangle$ at $t = 0$. By applying a $\pi/2$ rf pulse, a superposition of the two qubit states is produced $(|\circlearrowleft\rangle + |\circlearrowright\rangle)/\sqrt{2}\otimes|\Psi_0\rangle$, yielding distinct, qubit state dependent time evolution for $|\Psi_0\rangle$, where $|\circlearrowleft\rangle\otimes|\Psi_0\rangle$ represents the time evolved, weakly interacting gas, while $|\circlearrowright\rangle\otimes|\Psi_0\rangle$ stands for the strongly interacting LL. After time t, a second $\pi/2$ pulse and the measurement of the qubit current $\langle\hat{I}\rangle \sim \langle\sigma_z\rangle$ is performed, giving a signal proportional to $\mathcal{L}(t)$.

We have investigated the Loschmidt echo of Luttinger liquids after quantum quenches, and found universal behavior at various stages of the non-equilibrium time evolution[186]. These results were verified numerically by Frank Pollmann using MPS based methods on the XXZ Heisenberg model. A feasible experimental scheme using Ramsey interferometry on a hybrid

system of cold atoms and a flux qubit is proposed to test these ideas.

Chapter 8

Theses of this DSc dissertation

1. We have studied the evolution of the current in the two-dimensional Dirac equation, relevant for graphene and topological insulators, after switching on a longitudinal electric field E. The current parallel to the field reveals three distinct regions, termed as classical, Kubo and Schwinger regions. In the first one, the current increases linearly with time and electric field. In the second one, the current becomes time-independent, but scales linearly with the field. In the last region, the current grows as $\sim tE^{3/2}$, which is dominated by electron-hole pairs created by the strong electric field. From this, we predicted that the current-voltage characteristics of the steady state of graphene crosses over from the linear response regime to a non-linear regime, where the current increases with the 3/2 power of the applied voltage. Subsequent experiments have confirmed our prediction. We have also determined the non-linear Hall-current-voltage relation of graphene and topological insulators: for strong electric field, the Hall current is expected to increase a $E^{1/2}$.

2. The energy spectrum in bilayer graphene can be tuned by the application of a perpendicular electric field, which controls the opening of a band-gap around half-filling. We have shown that by modulating this gap in real time, excited states are produced in bilayer graphene, which parallels to the defect production during non-adiabatic passages though quantum critical points, described by the Kibble-Zurek theory. After the quench, population inversion occurs for wavevectors close to the Dirac point. This could, at least in principle provide a coherent source of infra-red radiation with tunable spectral properties (frequency and broadening).

3. The canonical model of quantum optics, the Jaynes-Cummings Hamil-

tonian describes a two level atom in a cavity interacting with electromagnetic field. Graphene, a condensed matter system, possesses low energy excitations obeying to the Dirac equation, and mimics the physics of quantum electrodynamics. These two seemingly unrelated fields turn out to be closely related to each other. We demonstrate that Rabi oscillations, corresponding to the excitations of the atom in the former case are observable in the optical response of the latter in quantizing magnetic field, providing us with a transparent picture about the structure of optical transitions in graphene. While the longitudinal conductivity reveals chaotic Rabi oscillations, the Hall component measures coherent ones. This opens up the exciting possibility of investigating a microscopic model of a few quantum objects in a macroscopic experiment of a bulk material with tunable parameters.

4. Inspired by the observation that time-periodic perturbations can be used to engineer topological properties of matter by altering the Floquet band structure, we have studied the fate of a spin-Hall edge state of a two-dimensional topological insulator in the presence of circularly polarized electromagnetic field. As opposed to similar problems, the spin-Hall edge state is sensitive mostly to the Zeeman term and not to the orbital effect. The photocurrent, which is directly proportional to the magnetization along the edge via the magnetoelectric effect, develops a finite, helicity dependent expectation value and turns from dissipationless to dissipative with increasing radiation frequency, signalling a change in the topological properties.

5. We have studied the effect of an interaction quench on one-dimensional gapless interacting systems, i.e. Luttinger liquids. The fermionic single particle density matrix reveals several regions of spatial and temporal coordinates relative to the quench time, termed as Fermi liquid, sudden quench Luttinger liquid, adiabatic Luttinger liquid regimes, and a Luttinger liquid regime with time dependent exponent. The various regimes are argued to be observable in the momentum distribution of the fermions, directly accessible through time of flight experiments. We have also investigated the hard-core bosons of the XXZ Heisenberg model and their correlation functions. These differ clearly from their fermionic counterpart and in the long time limit, the quench time does not reveal itself in their momentum distribution function. Our analytical results are benchmarked by comparing them to numerical simulations using matrix-product state based methods.

6. Motivated by recent developments in non-equilibrium statistical me-

chanics, we have studied the statistics of work done on a Luttinger liquid after an interaction quench. In the thermodynamic limit, the probability distribution function of the work done exhibits a non-Gaussian maximum around the excess heat, carrying almost all spectral weight. In contrast, in the small system limit most spectral weight is carried by a delta peak at the energy of the adiabatic process, and an oscillating probability distribution function with dips at energies commensurate to the quench duration and with an exponential envelope develops.

7. While much is known about Anderson's orthogonality catastrophe and the X-ray edge problem due to local perturbation, the many-body generalization of the orthogonality catastrophe is still lacking. Here we bridge this gap and study the generalized Loschmidt echo of Luttinger liquids after a global change of interaction. It decays exponentially with system size and exhibits universal behaviour: the steady state exponent after quenching back and forth n-times between 2 Luttinger liquids is $2n$-times bigger than that of the adiabatic overlap, and depends only on the initial and final Luttinger liquid parameters. These are corroborated numerically by matrix-product state based methods of the XXZ Heisenberg model. An experimental setup consisting of a hybrid system containing cold atoms and a flux qubit coupled to a Feshbach resonance is proposed to measure the Loschmidt echo using rf spectroscopy or Ramsey interferometry.

Papers related to this dissertation [1]:

1. **B. Dóra**, K. Ziegler, T. Thalmeier, M. Nakamura:
Rabi Oscillations in Landau Quantized Graphene
Phys. Rev. Lett. **102**, 036803 (2009)

2. **B. Dóra**, R. Moessner:
Non-linear electric transport in graphene: quantum quench dynamics and the Schwinger mechanism
Phys. Rev. B **81**, 165431 (2010)

3. **B. Dóra**, E. V. Castro, R. Moessner:
Quantum quench dynamics and population inversion in bilayer graphene
Phys. Rev. B **82**, 125441 (2010)

[1] see `http://mono.eik.bme.hu/~dora/publcit.pdf` for an up-to-date list of citations, including arXiv papers as well

4. **B. Dóra**, R. Moessner:
Dynamics of the spin-Hall effect in topological insulators and graphene
Phys. Rev. B **83**, 073403 (2011)

5. **B. Dóra**, M. Haque, G. Zaránd:
Crossover from adiabatic to sudden interaction quench in a Luttinger liquid
Phys. Rev. Lett. **106**, 156406 (2011)

6. **B. Dóra**, J. Cayssol, F. Simon, R. Moessner:
Optically engineering the topological properties of a spin Hall insulator
Phys. Rev. Lett. **108**, 056602 (2012)

7. **B. Dóra**, Á. Bácsi, G. Zaránd:
Generalized Gibbs ensemble and work statistics of a quenched Luttinger liquid
Phys. Rev. B **86**, 161109(R) (2012)

8. J. Cayssol, **B. Dóra**, F. Simon, R. Moessner:
Floquet topological insulators
Phys. Stat. Sol. RRL **7**, 101 (2013)

9. F. Pollmann, M. Haque, **B. Dóra**:
Linear quantum quench in the Heisenberg XXZ chain: time dependent Luttinger model description of a lattice system
Phys. Rev. B **87**, 041109(R) (2013)

10. **B. Dóra**, F. Pollmann, J. Fortágh, G. Zaránd:
Loschmidt echo and the many-body orthogonality catastrophe in a qubit-coupled Luttinger liquid
Phys. Rev. Lett. **111**, 046402 (2013)

Chapter 9

Acknowledgement

I'm grateful for my family for encouragement to perform the presented research. I have benefitted from useful and illuminating discussion with several colleagues and friends, in particular from the experimental side Ferenc Simon, Alex Grüneis, József Fortágh, and from the theorists Peter Thalmeier, Klaus Ziegler, Masaaki Nakamura, Roderich Moessner, Eduardo V. Castro, Masudul Haque, Gergely Zaránd, Ádám Bácsi, Attila Virosztek, Frank Pollmann, Jêrome Cayssol. I have learned a lot from them during our common work. Special thanks go to Attila Virosztek for his insightful comments on this dissertation.

Financial support by the Hungarian Scientific Research Fund No. K101244 and by the Bolyai Program of the HAS is gratefully acknowledged.

Bibliography

[1] K. S. Novoselov, A. K. Geim, S. V. Morozov, D. Jiang, Y. Zhang, S. V. Dubonos, I. V. Grigorieva, and A. A. Firsov, Science **306**, 666 (2004).

[2] K. S. Novoselov, A. K. Geim, S. V. Morozov, D. Jiang, M. I. Katsnelson, I. V. Grigorieva, S. V. Dubonos, and A. A. Firsov, Nature **438**, 197 (2005).

[3] A. H. Castro Neto, F. Guinea, N. M. R. Peres, K. S. Novoselov, and A. K. Geim, Rev. Mod. Phys. **81**, 109 (2009).

[4] V. V. Cheianov and V. I. Fal'ko, Phys. Rev. B **74**, 041403 (2006).

[5] C. W. J. Beenakker, Rev. Mod. Phys. **80**, 1337 (2008).

[6] M. I. Katsnelson, Eur. Phys. J. B **51**, 157 (2006).

[7] J. Cserti and G. Dávid, Phys. Rev. B **74**, 172305 (2006).

[8] S. Chakravarty, R. B. Laughlin, D. K. Morr, and C. Nayak, Phys. Rev. B **63**, 094503 (2001).

[9] A. W. W. Ludwig, M. P. A. Fisher, R. Shankar, and G. Grinstein, Phys. Rev. B **50**, 7526 (1994).

[10] M. I. Katsnelson, K. S. Novoselov, and A. K. Geim, Nat. Phys. **2**, 620 (2006).

[11] L. Tapasztó, G. Dobrik, P. Lambin, and L. P. Biró, Nat. Nanotech. **3**, 397 (2008).

[12] H. B. Nielsen and M. Ninomiya, Phys. Lett. B **105**, 219 (1981).

[13] K. S. Novoselov, Z. Jiang, Y. Zhang, S. V. Morozov, H. L. Stormer, U. Zeitler, J. C. Maan, G. S. Boebinger, P. Kim, and A. K. Geim, Science **315**, 1379 (2007).

[14] R. R. Nair, P. Blake, A. N. Grigorenko, K. S. Novoselov, T. J. Booth, T. Stauber, N. M. R. Peres, and A. K. Geim, Science **320**, 1308 (2008).

[15] X. Du, I. Skachko, F. Duerr, A. Luican, and E. Y. Andrei, Nature **462**, 192 (2009).

[16] K. I. Bolotin, F. Ghahari, M. D. Shulman, H. L. Stormer, and P. Kim, Nature **462**, 196 (2009).

[17] E. McCann, Phys. Rev. B **74**, 161403(R) (2006).

[18] E. V. Castro, K. S. Novoselov, S. V. Morozov, N. M. R. Peres, J. M. B. Lopes dos Santos, J. Nilsson, F. Guinea, A. K. Geim, and A. H. Castro Neto, J. Phys.: Condens. Matter **22**, 175503 (2010).

[19] J. B. Oostinga, H. B. Heersche, X. Liu, A. F. Morpurgo, and L. M. K. Vandersypen, Nature Mat. **7**, 151 (2007).

[20] K. F. Mak, C. H. Lui, J. Shan, and T. F. Heinz, Phys. Rev. Lett. **102**, 256405 (2009).

[21] F. Xia, D. B. Farmer, Y.-M. Lin, and P. Avouris, Nano Lett. **10**, 715 (2010).

[22] Y. Zhang, T.-T. Tang, C. Girit, Z. Hao, M. C. Martin, A. Zettl, M. F. Crommie, Y. R. Shen, and F. Wang, Nature **459**, 820 (2009).

[23] E. McCann and V. I. Fal'ko, Phys. Rev. Lett. **96**, 086805 (2006).

[24] H. Min, B. Sahu, S. K. Banerjee, and A. H. MacDonald, Phys. Rev. B **75**, 155115 (2007).

[25] S. Kim and E. Tutuc, *Quantum Hall effect in dual-gated graphene bilayers with tunable layer density imbalance*, arXiv:0909.2288.

[26] K. Novoselov, E. McCann, S. Morozov, V. Falko, M. Katsnelson, U. Zeitler, D. Jiang, F. Schedin, and A. Geim, Nature Physics **2**, 177 (2006).

[27] O. Vafek, Phys. Rev. B **82**, 205106 (2010).

[28] Y. Lemonik, I. L. Aleiner, Cs. Tőke, and V. I. Fal'ko, Phys. Rev. B **82**, 201408 (2010).

[29] O. Vafek and K. Yang, Phys. Rev. B **81**, 041401 (2010).

[30] F. Zhang, H. Min, M. Polini, and A. H. MacDonald, Phys. Rev. B **81**, 041402 (2010).

[31] K. v. Klitzing, G. Dorda, and M. Pepper, Phys. Rev. Lett. **45**, 494 (1980).

[32] D. J. Thouless, M. Kohmoto, M. P. Nightingale, and M. den Nijs, Phys. Rev. Lett. **49**, 405 (1982).

[33] M. Z. Hasan and C. L. Kane, Rev. Mod. Phys. **82**, 3045 (2010).

[34] X.-L. Qi and S.-C. Zhang, Rev. Mod. Phys. **83**, 1057 (2011).

[35] C. L. Kane and E. J. Mele, Phys. Rev. Lett. **95**, 226801 (2005).

[36] F. D. M. Haldane, Phys. Rev. Lett. **61**(18), 2015 (1988).

[37] M. Gmitra, S. Konschuh, C. Ertler, C. Ambrosch-Draxl, and J. Fabian, Phys. Rev. B **80**, 235431 (2009).

[38] N. Goldman, I. Satija, P. Nikolic, A. Bermudez, M. A. Martin-Delgado, M. Lewenstein, and I. B. Spielman, Phys. Rev. Lett. **105**, 255302 (2010).

[39] B. A. Bernevig, T. L. Hughes, and S.-C. Zhang, Science **314**, 1757 (2006).

[40] M. König, S. Wiedmann, C. Brune, A. Roth, H. Buhmann, L. W. Molenkamp, X.-L. Qi, and S.-C. Zhang, Science **318**, 766 (2007).

[41] V. V. Cheianov and V. I. Fal'ko, Phys. Rev. Lett. **97**, 226801 (2006).

[42] L. Landau, Phys. Zeitschrift der Sowjetunion **2**, 46 (1932).

[43] C. Zener, Proc. Royal Soc. London A **137**, 696 (1932).

[44] E. O. Kane and E. I. Blount, in *Tunneling Phenomena in Solids*, edited by E. Burstein and S. Lundqvist (Plenum Press, New York, 1969).

[45] N. Tanji, Ann. Phys. **324**, 1691 (2009).

[46] T. D. Cohen and D. A. McGady, Phys. Rev. D **78**, 036008 (2008).

[47] E. Merzbacher, *Quantum mechanics* (Wiley International, Tokyo, 1970).

[48] L. Landau and E. Lifshitz, *Quantum Mechanics, Vol. 3* (Pergamon, Oxford, 1981).

[49] A. M. Dykhne, Sov. Phys. JETP **14**, 941 (1962).

[50] B. Damski, Phys. Rev. Lett. **95**, 035701 (2005).

[51] J. Dziarmaga, Adv. Phys. **59**, 1063 (2010).

[52] J. Dziarmaga, Phys. Rev. Lett. **95**, 245701 (2005).

[53] F. Iglói and H. Rieger, Phys. Rev. Lett. **106**, 035701 (2011).

[54] T. W. B. Kibble, J. Phys. A **9**, 1387 (1976).

[55] W. H. Zurek, Nature **317**, 505 (1985).

[56] C. Bäuerle, Y. M. Bunkov, S. N. Fisher, H. Godfrin, and G. R. Pickett, Nature **382**, 332 (1996).

[57] V. M. Ruutu, V. B. Eltsov, A. Gill, T. W. Kibble, M. Krusius, Y. G. Makhlin, B. Placais, G. E. Volovik, and W. Xu, Nature **382**, 334 (1996).

[58] I. Chuang, R. Durrer, N. Turok, and B. Yurke, Science **251**, 1336 (1991).

[59] M. J. Bowick, L. Chandar, E. A. Schiff, and A. M. Srivastava, Science **263**, 943 (1994).

[60] L. E. Sadler, J. M. Higbie, S. R. Leslie, M. Vengalattore, and D. M. Stamper-Kurn, Nature **443**, 312 (2006).

[61] W. H. Zurek, U. Dorner, and P. Zoller, Phys. Rev. Lett. **95**, 105701 (2005).

[62] C. De Grandi, V. Gritsev, and A. Polkovnikov, Phys. Rev. B **81**, 012303 (2010).

[63] I. Bloch, J. Dalibard, and W. Zwerger, Rev. Mod. Phys. **80**, 885 (2008).

[64] P. Calabrese and J. Cardy, Phys. Rev. Lett. **96**, 136801 (2006).

[65] M. Rigol, V. Dunjko, and M. Olshanii, Nature **452**, 854 (2008).

[66] A. Polkovnikov, K. Sengupta, A. Silva, and M. Vengalattore, Rev. Mod. Phys. **83**, 863 (2011).

[67] S. Hofferberth, I. Lesanovsky, B. Fischer, T. Schumm, and J. Schmiedmayer, Nature **449**, 324 (2007).

[68] E. Haller, R. Hart, M. J. Mark, J. G. Danzl, L. Reichsollner, M. Gustavsson, M. Dalmonte, G. Pupillo, and H.-C. Nagerl, Nature **466**, 597 (2010).

[69] T. Kinoshita, T. Wenger, and D. S. Weiss, Nature **440**, 900 (2006).

[70] B. Paredes, A. Widera, V. Murg, O. Mandel, S. F. I. Cirac, G. V. Shlyapnikov, T. W. Hänsch, and I. Bloch, Nature **429**, 277 (2004).

[71] T. Giamarchi, *Quantum Physics in One Dimension* (Oxford University Press, Oxford, 2004).

[72] A. O. Gogolin, A. A. Nersesyan, and A. M. Tsvelik, *Bosonization and Strongly Correlated Systems* (Cambridge University Press, Cambridge, 1998).

[73] G. D. Mahan, *Many particle physics* (Plenum Publishers, New York, 1990).

[74] J. von Delft and H. Schoeller, Ann. Phys. (Leipzig) **7**, 225 (1998).

[75] R. Shankar, Acta Phys. Pol. B **26**, 1835 (1995).

[76] M. A. Cazalilla, J. Phys. B: At. Mol. Opt. Phys. **37**, S1 (2004).

[77] J. Sólyom, Adv. Phys. **28**, 201 (1979).

[78] G. Grüner, *Density waves in solids* (Addison-Wesley, Reading, 1994).

[79] R. Egger and A. O. Gogolin, Eur. Phys. J. B **3**, 281 (1998).

[80] C. Kane, L. Balents, and M. P. A. Fisher, Phys. Rev. Lett. **79**, 5086 (1997).

[81] L. Balents and M. P. A. Fisher, Phys. Rev. B **55**, 11973 (1997).

[82] H. Yoshioka and A. A. Odintsov, Phys. Rev. Lett. **82**, 374 (1999).

[83] Y. A. Krotov, D.-H. Lee, and S. G. Louie, Phys. Rev. Lett. **78**, 4245 (1997).

[84] H. Ishii, H. Kataura, H. Shiozawa, H. Yoshioka, H. Otsubo, Y. Takayama, T. Miyahara, S. Suzuki, Y. Achiba, M. Nakatake, T. Narimura, M. Higashiguchi, *et al.*, Nature **426**, 540 (2003).

[85] H. Rauf, T. Pichler, M. Knupfer, J. Fink, and H. Kataura, Phys. Rev. Lett. **93**, 096805 (2004).

[86] M. Bockrath, D. H. Cobden, J. Lu, A. G. Rinzler, R. E. Smalley, L. Balents, and P. L. McEuen, Nature **397**, 598 (1999).

[87] P. M. Singer, P. Wzietek, H. Alloul, F. Simon, and H. Kuzmany, Phys. Rev. Lett. **95**, 236403 (2005).

[88] B. Dóra, M. Gulácsi, F. Simon, and H. Kuzmany, Phys. Rev. Lett. **99**, 166402 (2007).

[89] B. Dóra, M. Gulácsi, J. Koltai, V. Zólyomi, J. Kürti, and F. Simon, Phys. Rev. Lett. **101**, 106408 (2008).

[90] H. Moritz, T. Stöferle, K. Günter, M. Köhl, and T. Esslinger, Phys. Rev. Lett. **94**, 210401 (2005).

[91] K. Günter, T. Stöferle, H. Moritz, M. Köhl, and T. Esslinger, Phys. Rev. Lett. **95**, 230401 (2005).

[92] M. Köhl, H. Moritz, T. Stöferle, K. Günter, and T. Esslinger, Phys. Rev. Lett. **94**(8), 080403 (2005).

[93] Y. an Liao, A. S. C. Rittner, T. Paprotta, W. Li, G. B. Partridge, R. G. Hulet, S. K. Baur, and E. J. Mueller, Nature **467**, 567 (2010).

[94] T. Fukuhara, Y. Takasu, M. Kumakura, and Y. Takahashi, Phys. Rev. Lett. **98**, 030401 (2007).

[95] M. Lu, S. H. Youn, and B. L. Lev, Phys. Rev. Lett. **104**, 063001 (2010).

[96] B. J. DeSalvo, M. Yan, P. G. Mickelson, Y. N. Martinez de Escobar, and T. C. Killian, Phys. Rev. Lett. **105**, 030402 (2010).

[97] F. Herrmann and P. Schmälzle, Am. J. Phys. **49**, 761 (1981).

[98] M. A. Cazalilla, R. Citro, T. Giamarchi, E. Orignac, and M. Rigol, Rev. Mod. Phys. **83**, 1405 (2011).

[99] J. Schwinger, Phys. Rev. **82**, 664 (1951).

[100] M. Ben Dahan, E. Peik, J. Reichel, Y. Castin, and C. Salomon, Phys. Rev. Lett. **76**, 4508 (1996).

[101] B. Dóra and R. Moessner, Phys. Rev. B **81**, 165431 (2010).

[102] B. Dóra and R. Moessner, Phys. Rev. B **83**, 073403 (2011).

[103] K. Ziegler, Phys. Rev. B **75**, 233407 (2007).

[104] J. Cserti, Phys. Rev. B **75**, 033405 (2007).

[105] A. G. Green and S. L. Sondhi, Phys. Rev. Lett. **95**, 267001 (2005).

[106] M. Lewkowicz and B. Rosenstein, Phys. Rev. Lett. **102**, 106802 (2009).

[107] S. P. Gavrilov and D. M. Gitman, Phys. Rev. D **53**, 7162 (1996).

[108] D. Allor, T. D. Cohen, and D. A. McGady, Phys. Rev. D **78**, 096009 (2008).

[109] V. Ryzhii, M. Ryzhii, V. Mitin, and M. S. Shur, Appl. Phys. Express **2**, 034503 (2009).

[110] N. V. Vitanov and B. M. Garraway, Phys. Rev. A **53**, 4288 (1996).

[111] P. Boross, B. Dóra, and R. Moessner, Phys. Stat. Sol. B **248**, 2627 (2011).

[112] J. Moser, A. Barreiro, and A. Bachtold, Appl. Phys. Lett. **91**, 163513 (2007).

[113] N. Vandecasteele, A. Barreiro, M. Lazzeri, A. Bachtold, and F. Mauri, Phys. Rev. B **82**, 045416 (2010).

[114] S. Katayama, A. Kobayashi, and Y. Suzumura, J. Phys. Soc. Jpn. **75**, 054705 (2006).

[115] G. W. Semenoff, Phys. Rev. Lett. **53**, 2449 (1984).

[116] V. Singh and M. M. Deshmukh, Phys. Rev. B **80**, 081404 (2009).

[117] I. Garate and M. Franz, Phys. Rev. Lett. **104**, 146802 (2010).

[118] X.-L. Qi, T. L. Hughes, and S.-C. Zhang, Phys. Rev. B **78**, 195424 (2008).

[119] J. Sinova, D. Culcer, Q. Niu, N. A. Sinitsyn, T. Jungwirth, and A. H. MacDonald, Phys. Rev. Lett. **92**, 126603 (2004).

[120] M. Koshino, Phys. Rev. B **78**, 155411 (2008).

[121] J. E. Avron and Z. Kons, J. Phys. A: Math. Gen. **32**, 6097 (1999).

[122] D. Huertas-Hernando, F. Guinea, and A. Brataas, Phys. Rev. B **74**, 155426 (2006).

[123] V. Lukose, R. Shankar, and G. Baskaran, Phys. Rev. Lett. **98**, 116802 (2007).

[124] N. M. R. Peres and E. V. Castro, J. Phys. Cond. Matter **19**, 406231 (2007).

[125] S. Mondal, D. Sen, K. Sengupta, and R. Shankar, Phys. Rev. B **82**, 045120 (2010).

[126] A. V. Andreev, Phys. Rev. Lett. **99**, 247204 (2007).

[127] V. Ryzhii, M. Ryzhii, and T. Otsuji, J. Appl. Phys. **101**, 083114 (2007).

[128] B. Dóra, E. V. Castro, and R. Moessner, Phys. Rev. B **82**, 125441 (2010).

[129] R. Barankov and A. Polkovnikov, Phys. Rev. Lett. **101**, 076801 (2008).

[130] A. K. Sen, K. K. Bardhan, and B. K. Chakrabarti, eds., *Quantum and Semi-classical Percolation and Breakdown in Disordered Solids* (Springer, Berlin, 2009).

[131] J. Cardy, *Scaling and renormalization in statistical physics* (Cambridge University Press, Cambridge, 1996).

[132] M. Uhlmann, R. Schützhold, and U. R. Fischer, Phys. Rev. D **81**, 025017 (2010).

[133] D. S. L. Abergel and V. Fal'ko, Phys. Rev. B **75**, 155430 (2007).

[134] E. J. Nicol and J. P. Carbotte, Phys. Rev. B **77**, 155409 (2008).

[135] M. Monteverde, C. Ojeda-Aristizabal, R. Weil, M. Ferrier, S. Gueron, H. Bouchiat, J. N. Fuchs, and D.Maslov, Phys. Rev. Lett. **104**, 126801 (2010).

[136] K. Sun, H. Yao, E. Fradkin, and S. A. Kivelson, Phys. Rev. Lett. **103**, 046811 (2009).

[137] F. Guinea, A. H. Castro Neto, and N. M. R. Peres, Phys. Rev. B **73**, 245426 (2006).

[138] H. Min and A. MacDonald, Phys. Rev. B **77**, 155416 (2008).

[139] G. Li and E. Y. Andrei, Nat. Phys. **3**, 623 (2007).

[140] Z. Jiang, E. A. Henriksen, L. C. Tung, Y.-J. Wang, M. E. Schwartz, M. Y. Han, P. Kim, and H. L. Stormer, Phys. Rev. Lett. **98**, 197403 (2007).

[141] B. Dóra, K. Ziegler, P. Thalmeier, and M. Nakamura, Phys. Rev. Lett. **102**, 036803 (2009).

[142] B. W. Shore and P. L. Knight, J. Mod. Opt. **40**, 1195 (1993).

[143] D. V. Khveshchenko, Phys. Rev. Lett. **87**, 206401 (2001).

[144] S. Y. Zhou, G. Gweon, A. V. Fedorov, P. N. First, W. A. de Heer, D. Lee, F. Guinea, A. H. Castro Neto, and A. Lanzara, Nature Materials **6**, 770 (2007).

[145] D. Braak, Phys. Rev. Lett. **107**, 100401 (2011).

[146] J. Schliemann, Phys. Rev. B **77**, 125303 (2008).

[147] J. Schliemann, New J. Phys. **10**, 043024 (2008).

[148] G. S. Agarwal, J. Opt. Soc. Am. B **2**, 480 (1985).

[149] Z. Q. Li, E. A. Henriksen, Z. Jiang, Z. Hao, M. C. Martin, P. Kim, H. L. Stormer, and D. N. Basov, Nat. Phys. **4**, 532 (2008).

[150] A. Bermudez, M. A. Martin-Delgado, and E. Solano, Phys. Rev. Lett. **99**, 123602 (2007).

[151] T. Ando, Y. Zheng, and H. Suzuura, J. Phys. Soc. Jpn. **71**, 1318 (2002).

[152] M.-F. Yang, Phys. Rev. B **76**, 180403 (2007).

[153] V. P. Gusynin, S. G. Sharapov, and J. P. Carbotte, Phys. Rev. Lett. **98**, 157402 (2007).

[154] V. P. Gusynin, S. G. Sharapov, and J. P. Carbotte, J. Phys.: Cond. Matter **19**, 026222 (2007).

[155] P. L. Knight and P. M. Radmore, Phys. Lett. A **90**, 342 (1982).

[156] J. Sabio, J. Nilsson, and A. H. Castro Neto, Phys. Rev. B **78**, 075410 (2008).

[157] F. Guinea, Sol. St. Commun. **152**(15), 1437 (2012).

[158] S. Raghu, X.-L. Qi, C. Honerkamp, and S.-C. Zhang, Phys. Rev. Lett. **100**, 156401 (2008).

[159] E. V. Castro, A. G. Grushin, B. Valenzuela, M. A. H. Vozmediano, A. Cortijo, and F. de Juan, Phys. Rev. Lett. **107**, 106402 (2011).

[160] I. F. Herbut, Phys. Rev. B **78**, 205433 (2008).

[161] B. Roy and I. F. Herbut, Phys. Rev. B **88**, 045425 (2013).

[162] B. Dóra, J. Cayssol, F. Simon, and R. Moessner, Phys. Rev. Lett. **108**, 056602 (2012).

[163] J. Cayssol, B. Dóra, F. Simon, and R. Moessner, Phys. Stat. Sol. RRL **7**, 101 (2013).

[164] H. Sambe, Phys. Rev. A **7**, 2203 (1973).

[165] T. Dittrich, P. Hanggi, G.-L. Ingold, B. Kramer, G. Schon, and W. Zwerger, eds., *Quantum Transport and Dissipation* (Wiley-WCH, Weinheim, 1998).

[166] N. H. Lindner, G. Refael, and V. Galitski, Nat. Phys. **7**, 490 (2011).

[167] T. Kitagawa, T. Oka, A. Brataas, L. Fu, and E. Demler, Phys. Rev. B **84**, 235108 (2011).

[168] T. Oka and H. Aoki, Phys. Rev. B **79**, 081406 (2009).

[169] P. Hosur, Phys. Rev. B **83**, 035309 (2011).

[170] J.-i. Inoue and A. Tanaka, Phys. Rev. Lett. **105**, 017401 (2010).

[171] D. S. L. Abergel and T. Chakraborty, Nanotechnology **22**, 015203 (2011).

[172] M. J. Schmidt, E. G. Novik, M. Kindermann, and B. Trauzettel, Phys. Rev. B **79**, 241306 (2009).

[173] X.-L. Qi, T. L. Hughes, and S.-C. Zhang, Nat. Phys. **4**, 273 (2008).

[174] J. Goldstone and F. Wilczek, Phys. Rev. Lett. **47**, 986 (1981).

[175] D. J. Thouless, Phys. Rev. B **27**, 6083 (1983).

[176] J. Karch, P. Olbrich, M. Schmalzbauer, C. Zoth, C. Brinsteiner, M. Fehrenbacher, U. Wurstbauer, M. M. Glazov, S. A. Tarasenko, E. L. Ivchenko, D. Weiss, J. Eroms, *et al.*, Phys. Rev. Lett. **105**, 227402 (2010).

[177] B. Wittmann, S. N. Danilov, V. Bel'kov, S. A. Tarasenko, E. G. Novik, H. Buhmann, C. Brüne, L. W. Molenkamp, Z. D. Kvon, N. N. Mikhailov, S. A. Dvoretsky, N. Q. Vinh, *et al.*, Semicond. Sci. Technol. **25**, 095005 (2010).

[178] D. B. Gutman, Y. Gefen, and A. D. Mirlin, Phys. Rev. B **81**, 085436 (2010).

[179] E. Perfetto, G. Stefanucci, and M. Cini, Phys. Rev. Lett. **105**, 156802 (2010).

[180] M. A. Cazalilla, Phys. Rev. Lett. **97**, 156403 (2006).

[181] G. S. Uhrig, Phys. Rev. A **80**, 061602(R) (2009).

[182] A. Iucci and M. A. Cazalilla, Phys. Rev. A **80**, 063619 (2009).

[183] B. Dóra, M. Haque, and G. Zaránd, Phys. Rev. Lett. **106**, 156406 (2011).

[184] F. Pollmann, M. Haque, and B. Dóra, Phys. Rev. B **87**, 041109 (2013).

[185] B. Dóra, A. Bácsi, and G. Zaránd, Phys. Rev. B **86**, 161109 (2012).

[186] B. Dóra, F. Pollmann, J. Fortágh, and G. Zaránd, Phys. Rev. Lett. **111**, 046402 (2013).

[187] C. Karrasch, J. Rentrop, D. Schuricht, and V. Meden, Phys. Rev. Lett. **109**, 126406 (2012).

[188] M. Fannes, B. Nachtergaele, and R. W. Werner, Commun. Math. Phys. **144**, 443 (1992).

[189] S. R. White, Phys. Rev. Lett. **69**(19), 2863 (1992).

[190] J. A. Kjäll, M. P. Zaletel, R. S. K. Mong, J. H. Bardarson, and F. Pollmann, Phys. Rev. B **87**, 235106 (2013).

[191] I. McCulloch, J. Stat. Mech Theor. Exp. p. P10014 (2007).

[192] G. Vidal, Phys. Rev. Lett. **98**, 070201 (2007).

[193] U. Schollwöck, Annals of Physics **326**, 96 (2011).

[194] F. Pollmann, S. Mukerjee, A. A. M. Turner, and J. E. Moore, Phys. Rev. Lett. **102**, 255701 (2009).

[195] L. Tagliacozzo, T. R. de Oliviera, S. Iblisdir, and J. I. Latorre, Phys. Rev. B **78**, 024410 (2008).

[196] V. S. Shchesnovich, Phys. Lett. A **349**, 398 (2006).

[197] J.-S. Bernier, G. Roux, and C. Kollath, Phys. Rev. Lett. **106**, 200601 (2011).

[198] A. Polkovnikov and V. Gritsev, Nat. Phys. **4**, 477 (2008).

[199] F. Pellegrini, S. Montangero, G. E. Santoro, and R. Fazio, Phys. Rev. B **77**, 140404 (2008).

[200] C. De Grandi and A. Polkovnikov, in *Quantum Quenching, Annealing and Computation*, edited by A. K. Chandra, A. Das, and B. K. Chakrabarti (Springer Berlin / Heidelberg, 2010), vol. 802 of *Lecture Notes in Physics*.

[201] B. M. McCoy, Phys. Rev. **173**, 531 (1968).

[202] M. Rigol and A. Muramatsu, Phys. Rev. A **70**, 031603 (2004).

[203] V. Gritsev, E. Altman, E. Demler, and A. Polkovnikov, Nat. Phys. **2**, 705 (2006).

[204] M. Gring, M. Kuhnert, T. Langen, T. Kitagawa, B. Rauer, M. Schreitl, I. Mazets, D. A. Smith, E. Demler, and J. Schmiedmayer, Science **337**, 1318 (2012).

[205] A. Silva, Phys. Rev. Lett. **101**, 120603 (2008).

[206] L. Campos Venuti and P. Zanardi, Phys. Rev. A **81**, 022113 (2010).

[207] M. Campisi, P. Hänggi, and P. Talkner, Rev. Mod. Phys. **83**, 771 (2011).

[208] P. Talkner, E. Lutz, and P. Hänggi, Phys. Rev. E **75**, 050102 (2007).

[209] F. Pollmann, S. Mukerjee, A. G. Green, and J. E. Moore, Phys. Rev. E **81**, 020101 (2010).

[210] M. M. Rams and B. Damski, Phys. Rev. Lett. **106**, 055701 (2011).

[211] A. F. Siegel, Biometrika **66**, 381 (1979).

[212] M. Clusel and E. Bertin, Int. J. Mod. Phys. B **22**, 3311 (2008).

[213] T. Kinoshita, T. Wenger, and D. S. Weiss, Science **305**, 1125 (2004).

[214] D. Chen, M. White, C. Borries, and B. DeMarco, Phys. Rev. Lett. **106**, 235304 (2011).

[215] A. Peres, Phys. Rev. A **30**, 1610 (1984).

[216] T. Gorina, T. Prosen, T. H. Seligman, and M. Znidari, Phys. Rep. **435**, 33 (2006).

[217] A. Goussev, R. A. Jalabert, H. M. Pastawski, and D. A. Wisniacki, Scholarpedia **7**, 11687 (2012).

[218] L. Campos Venuti, N. T. Jacobson, S. Santra, and P. Zanardi, Phys. Rev. Lett. **107**, 010403 (2011).

[219] J. Goold, T. Fogarty, N. Lo Gullo, M. Paternostro, and T. Busch, Phys. Rev. A **84**, 063632 (2011).

[220] M. Knap, A. Shashi, Y. Nishida, A. Imambekov, D. A. Abanin, and E. Demler, Phys. Rev. X **2**, 041020 (2012).

[221] D. Rossini, T. Calarco, V. Giovannetti, S. Montangero, and R. Fazio, Phys. Rev. A **75**, 032333 (2007).

[222] J. O. Fjaerestad, J. Stat. Mech. p. P07011 (2008).

[223] J. Sirker, Phys. Rev. Lett. **105**, 117203 (2010).

[224] J. R. Friedman, V. Patel, W. Chen, S. K. Tolpygo, and J. E. Lukens, Nature **406**, 43 (2000).

[225] C. H. van der Wal, A. C. J. ter Haar, F. K. Wilhelm, R. N. Schouten, C. J. P. M. Harmans, T. P. Orlando, S. Lloyd, and J. E. Mooij, Science **290**, 773 (2000).

[226] A. Widera, S. Trotzky, P. Cheinet, S. Fölling, F. Gerbier, I. Bloch, V. Gritsev, M. D. Lukin, and E. Demler, Phys. Rev. Lett. **100**, 140401 (2008).